Experimental study onf the fragmentation of adenine and porphyrin molecules induced by low energy multicharged ion impact

Bin Li

N° d'ordre : 135-2010 Année :2010

THESE

présentée

devant l'UNIVERSITE CLAUDE BERNARD-LYON1

ECOLE DOCTORALE DE PHYSIQUE ET D'ASTROPHYSIQUE

pour l'obtention du

DIPLOME DE DOCTORAT EN CO-TUTELLE
(arrêté du 01 septembre 2006)
avec L'Institute de Physique Moderne, L'académie des Sciences, Chine

Présentée et soutenue publiquement le 27 Août 2010

par

Bin LI

TITRE

Experimental study on the fragmentation of Adenine and Porphyrin molecules induced by low energy multicharged ion impact

Directeurs de thèse:
Li CHEN et Xinwen MA

JURY :

Amine CASSIMI (Rapporteur)
Ximeng CHEN (Rapporteur)
Li CHEN
Serge MARTIN
Xinwen MA
Jianguo WANG

Contents

Acknowledgements

This work has been accomplished from September 2006 to August 2010, with close collaboration between the two laboratories LASIM in University Lyon1 in France and the atomic physics group in the Institute of Modern Physics in China.

Having reached the end of this work, I would like to express my thanks to the people who supported and inspired me throughout this period of my life. My deepest gratitude goes first and foremost to my supervisors, Mrs. Li CHEN and Mr. Xinwen MA, for helping and guiding me through the numerous details of the experiments, data analysis, and even the English writings. Without their constant and illuminating instruction, this thesis could not be finished. I would also like to thank them for providing me the opportunity to study alternately between France and China, which has given me wonderful experience and pleasant memories.

My great thanks are extended to Mr. Serge MARTIN, the leader of Multi-charged ion team in LASIM. He was not only kindly accepted me in his team, throughout my stay in LASIM he always guided and encouraged me to face many problems concerning the experimental setup operation and the experimental data interpretation. Another two permanent members in the team, Mr. Richard BRÉDY, and Mr. Jérôme BERNARD were invaluable part of this research. I appreciate for their guidance and helpful discussions on my thesis. I also want to thank the engineer, Mr. Guillaume MONTAGNE for his technique supports in the experiments.

I would like to extend my special thanks to Ms. Chantal LAGRIFFOUL, Mrs. Li CHEN, and Mr. Richard BRÉDY for their continual attention of my living in Lyon. I also express my thanks to my colleagues for their help in the experiment in Lanzhou. They are Mrs. Huiping LIU, Mr. Xiaolong ZHU, Mr. Dongbin QIAN, Mr. Shaofeng ZHANG.

I also express my gratefulness to Mr. Amine CASSIMI, and Mr. Ximeng CHEN for reading and commenting on my thesis manuscript.

It is a pleasure to acknowledge at this point the team running the ARIBE facility in CEAN and the ECR ion source team in the Institute of Modern Physics in Lanzhou for providing high quality ion beams.

I gratefully acknowledge the French government for the financial support in my stay in France, and ITS-LEIF for the financial support in performing collaboration experiments with GANIL laboratory and attending the winter school.

I also wish to express my appreciation to Prof. Christian BORDAS, Prof. Jacques DOURY, Prof. L. COLLET, Prof. Wenlong ZHAN, Prof. Guoqing XIAO, and Prof. Hushan XU for their support of the joint supervised program.

Finally, I would like to express my deep and most sincere thanks along with my true love to my wife and my parents for their support all these years.

ABSTRACT

Since the dissociation of small molecules might play key roles in the understanding of radiation induced damages of living tissues at the primary steps and at the molecular levels, fragmentation dynamics of small biomolecules have drawn much attention. The knowledge of the internal energy is of fundamental importance for understanding its fragmentation dynamics following external excitation. For a long time however, it was difficult to measure this parameter in coincidence with the fragmentation patterns until the development of CIDEC (Collision Induced Dissociation under Energy Control) method in 2007. In this work, the CIDEC method was extended to study the fragmentation of gas-phase biomolecules adenine ($H_5C_5N_5$) and Porphyrin chloride FeTPPCl ($C_{44}H_{28}N_4FeCl$). The population distribution for each dissociation channel as a function of the excitation energy of the parent molecular ions at a well-determined initial charge state has been experimentally determined, which could shed some light on the fragmentation dynamics of these molecules.

In collisions between Cl^+ and Ade at 3keV, the fragmentation pattern of Ade^{2+} is dominated by the loss of H_2CN^+ and the successive emission of HCN. The energy distribution of the parent dication confirms the successive emission dynamics. A specific decay channel is observed, i.e., the emission of a charged H_2CN^+ followed by the emission of HC_2N_2. The measured mean excitation energies of this channel and other competitive channels are compared.

In Kr^{8+}-FeTPPCl collisions at 80keV, parent ions $FeTPPCl^{1+,2+,3+}$ are observed, along with the corresponding decay patterns. It is found that, in the first step the dominant low-energy-cost decay channel is the emission of Cl^0 independent of the initial charge state of $FeTPPCl^{r+}$. For the resulted dication $FeTPP^{2+}$, the dominant fragmentation channel is the neutral evaporation; for the trication however, the dominant fragmentation channel is the asymmetrical fission by emission of a charged fragment. In the case of H^+ and F^+ impact at 3keV, due to the different reaction windows opened in the two collision systems, different fragmentation patterns are observed. The internal energy distributions of the parent ions are experimentally determined. In addition, nH_2 loss processes are observed.

The negative ion production yield emerged in F^{2+}-Ade collision at 30keV is also measured in this work using a new experimental approach. The negative ion production yield is measured to be about 1%.

Key words: Ion irradiation, small biomolecule, fragmentation mechanism, excitation energy measurement, negative ion production yield

Chapter I Introduction

In this work, we study the fragmentation of small molecules of biological interests induced by ion impact at low energy range (v<1 a.u.). Fragmentation dynamics of small biomolecules have drawn much attention from growing scientific communities during the last decades. This is mainly due to the fact that the dissociation of small molecules, for example the building blocks of DNA (Deoxyribonucleic acid), might play key roles in the understanding of the radiation induced damage of living tissues at the primary steps and at the molecular levels. In the laboratories, different species of particles such as electrons, photons and ions have been employed to excite the objective biomolecules and to induce their dissociation. Numerous works about this topic can be found in the literatures covering a large energy range [1-6].

Interaction between low energy particles and small biomolecules is gaining particular interests during the last years. It is now well established that heavy ion-beam (~MeV) provides a promising tool for some types of cancer therapy due to the specific characteristic energy loss of heavy ions in matter, i.e., the increase of the energy deposition with penetration depth resulting in the well known Bragg peak. With the selective energy deposition into a relatively small volume (the Bragg peak), the ion-beam irradiation can reduce damage to healthy tissue as far as possible. In hadrontherapy, when the primary ions travel through living cells and organisms, a sequence of events of ionizing radiation happens. Along the primary ion track and in the volume of the Bragg peak, plenty of secondary particles such as low energy electrons, radicals, excited molecules and singly/multiply charged ions are produced. The damage of DNA molecules induced not only by direct impact of the primary high-energy particles but also by secondary species at low energy becomes a relevant problem.

In the DNA damage of living cells, it is thought that the single-strand break (SSB) most probably can be repaired without further consequences; for double-strand break (DSB), however, it may cause the death of a cell and/or mutations (illustrated in Figure 1 for SSB and DSB). So the sequence of events happened in radiation eventually can lead to the tissue modifications at the molecular and cellular levels. Recent observations involving low energy electron impact on DNA films showed that covalent damage to double-stranded DNA and its components can occur at energies well below the ionization energy thresholds [1]. This pioneering work has stimulated the investigation of DNA/RNA damage induced by low

energy ions, and the investigations of ionization and fragmentation of small biomolecules, including DNA/RNA and its building blocks.

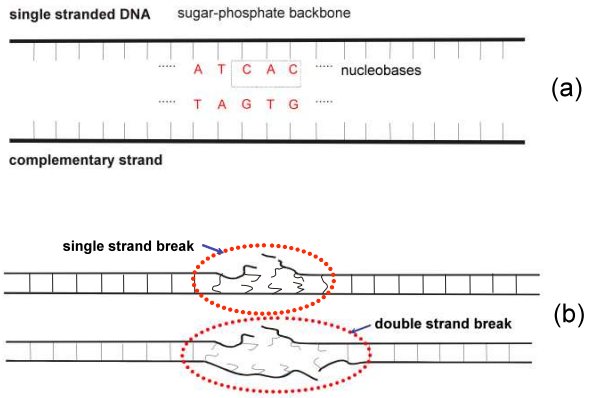

Figure 1. (a). Illustration for intact DNA. (b). Illustration for SSB and DSB.

I.1. *Fragmentation of small biomolecules induced by electrons, photons, and ions*

I.1.1. Low energy electron driven damage in biomolecules

In ionizing radiations, large quantities of low energy secondary electrons are produced, about 10^5 electrons per MeV. From a radiobiological point of view, there is considerable interest in studying the fragmentation of biomolecules induced by low energy electrons. In the past decade, plenty of works were contributed on low energy electron driven damage of biomolecules, including the elementary components of the DNA molecule (i.e., the bases, sugar and phosphate group analogs and oligonucleotides) and of proteins (e.g. amino acids) (see for example [5] and reference therein, for a good topical review on both experimental progresses and theoretical advances). In these experiments the targets were prepared either in the gas phase or in condensed phase.

I.1.1.1. Biomolecules in condensed phase

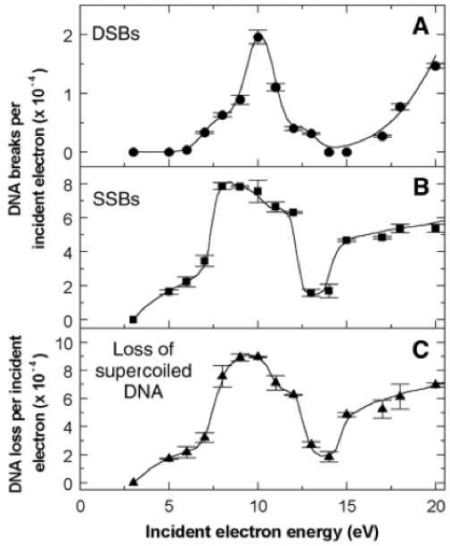

Figure 2. Measured quantum yields, per incident electron, for the induction of DSBs(A), SSBs(B), and the loss of the supercoiled DNA form(C), in DNA solids by low-energy electron irradiation as a function of incident electron energy. From reference [1].

Among the rich works in low energy electron on condensed-phase biomolecule interaction experiments (see for example [1, 7-11]), a benchmark work was performed by L. Sanche and co-workers [1]. In the traditional notion, it is thought that genotoxic damage by secondary electrons can only occur at energies above the onset of ionization, or upon solvation when they become a slowly reacting chemical species. The finding of Badia Boudaïffa *et al.* [1] however, presents a fundamental challenge for this concept. In their work, plasmid DNA was irradiated by very low energy electron beam (3 to 20eV) under ultrahigh vacuum conditions. After irradiation, the samples were analyzed with the agarose gel electrophoresis method. The resultant DNA was classified as supercoiled (undamaged), nicked circle (SSB), full-length linear (DSB), and short linear forms. From their measurement, it was found that incident electrons, even at energies well below ionization thresholds of DNA, did induce substantial yields of single- and double-strand breaks in DNA (Figure 2). Based on this observation, they concluded that, below 14eV, the measured DNA strand breaks were initiated by resonant electron attachment to the various basic DNA components (base, deoxyribose, phosphate, or hydration H_2O), leading to the formation of a transient molecular anion. Within the lifetime of the transient molecular anion, usually at the scale of femtosecond, bond dissociations might occur. In fact, the dissociative electronically excited fragments, stable anions, or neutral radicals emerged from the decay of transient molecular anion may also trigger further reactions within large biomolecules or with nearby molecules and then result in more complex chemical damage. Their findings suggest that the plentiful low energy secondary electrons, and most likely their ionic and radical reaction products, play a crucial role

in the nascent stages of DNA radiolysis and may already induce substantial damage in a very short time range long before their thermalization.

I.1.1.2. Biomolecules in gas-phase

Electron attachment to small biomolecules has been investigated in the gas-phase first by T. D. Märk and co-workers (see for example [12-19]). In their experiments of electron attachment to uracil (molecule formula $C_4H_4N_2O_2$) [12], they have shown that even ultralow energy electrons (lower than the threshold energy for electronic excitation, i.e., <3 eV) could induce hydrogen radical abstraction via dissociative electron attachment (Figure 3). The electron attachment cross-sections due to low energy electron impact have been also measured as a function of the incident electron energy for other small molecules, thymine [14, 19], cytosine [19], uracil [15, 20], deoxyribose [17], thymidine [21], and uridine [21] etc.

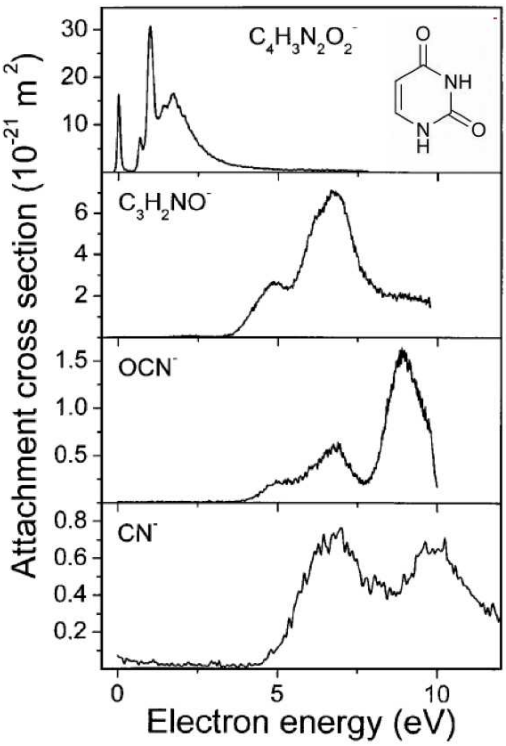

Figure 3. Absolute partial cross sections for electron attachment to gas phase uracil as a function of incident energy, with the insertion of the molecular structure of uracil. From reference [12].

In electron-molecule interactions, electron impact induced ionization and fragmentation of molecules is another important channel. A relevant measurable parameter for these processes is

the so-called Appearance Energy (AE). The AE is defined as the minimum energy of the impacting electrons leading to the appearance of a given molecular ion (parent or fragment cation) [16]. In low energy electron impact ionization investigation of, for example uracil [16], deoxyribose [17], thymidine [21], uridine [21], and tetraphenyl iron (III) porphyrin chloride (FeTPPCl) [22], etc, large variety of cation fragments were produced and the corresponding AE values were determined by measuring the ion efficiency curves of both parent ions and fragmented ones.

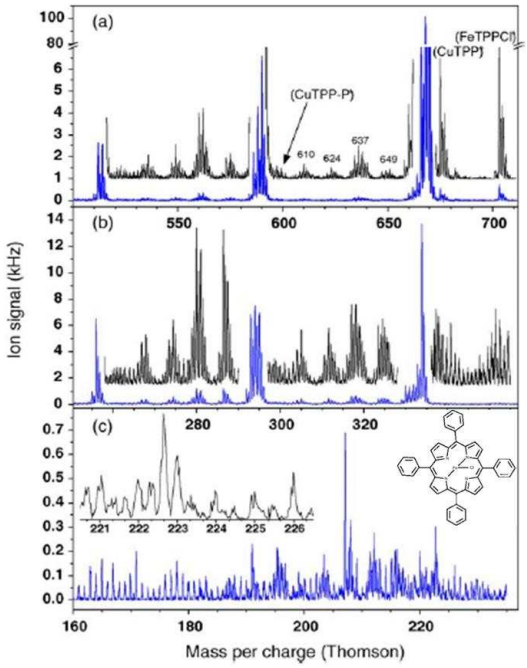

Figure 4. Mass spectrum of FeTPPCl recorded at an electron energy of 70 eV. The upper diagram (a) shows the singly charged ions of the high m/q regime, in the middle (b), the doubly charged regime is presented and the lowest panel (c) shows the triply charged regime. In (a) and (b) the mass spectra, except for the high intensity peaks, are plotted a second time multiplied by a factor of 10 and added with a constant shift to see in more details the low-intensity peaks. The numbers in (a) indicate the mean mass of the corresponding bunch of peaks. The molecular structure of FeTPPCl is inserted in (c). From reference [22].

The example of electron induced ionization and fragmentation of FeTPPCl molecule [22] is shown here because these results will be discussed in comparison with our measurement in heavy ion impact experiment in the chapter IV. Mass spectra of FeTPPCl recorded at an electron energy of 70 eV is presented in Figure 4. In these mass spectra, three distinct groups of ions, i.e. the high mass over charge group of singly charged ions, the medium mass over charge group of doubly charged ions, and the low mass over charge group of triply charged ions, were clearly

identified. The AEs of the most abundant singly and doubly charged ions were determined using the ion efficiency curves (Figure 5 and Figure 6). The AEs of the singly charged parent ion $FeTPPCl^+$ and fragment ion $FeTPP^+$ were measured to be about 9.7eV. For the doubly charged ion $FeTPP^{2+}$, the AE was obtained to be 18eV. From the curves at higher energy, the AEs of the main dissociation channels of the molecule by the loss of one or two phenyl groups (see details in the chapter IV) were also determined.

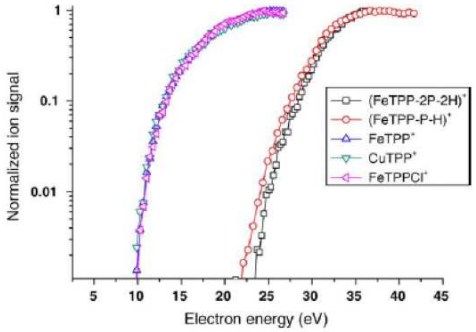

Figure 5. Normalized ion efficiency curves of the most abundant singly charged fragment ions. The intersection of the curves with the x-axis is taken as the corresponding threshold energy. From reference [22].

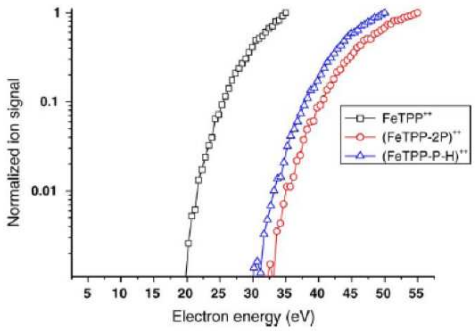

Figure 6. Normalized ion efficiency curves of the most abundant doubly charged fragment ions. The intersection of the curves with the x-axis is taken as the corresponding threshold energy. From reference [22].

I.1.2. Low energy heavy ion induced damage in DNA components

Besides low energy secondary electrons, low energy heavy ions have also attracted great attention in recent studies. Observations by T. Schlathölter and co-workers [2, 23] suggested that along the radiation track of a primary heavy ion beam, significant amounts of secondary atomic cations with hyperthermal energies up to hundreds of electron volts might be produced from DNA bases. This finding motivated the investigations by Michael A. Huels and co-workers on the hyperthermal heavy ion and DNA component interactions [3, 24-27].

In their first hyperthermal heavy ion (Ar^+ at energies from 10eV to 100eV) on DNA components scattering experiments, Z. W. Deng et al. investigated the fragmentation of fundamental building blocks of DNA in condensed phase [3]. The typical ion stimulated desorption mass spectra produced by 100 eV Ar^+ impact on films of thymine, 2-deoxy-D-ribose and thymidine are presented in Figure 7. The thymidine is also called thymine deoxyriboside. It is a nucleoside composed of deoxyribose (a sugar) joined to thymine (a nucleobase). Small fragments are dominant in the three spectra. The similarity between the spectra of dR and dT at

the low mass part (<80 m/e) was considered as the signature that in the case of the basic nucleoside thymidine, most of the low mass cation fragments originate from the sugar moiety. This observation showed that in ion irradiated DNA the sugar backbone was likely to be more fragile than the nucleobases. In the case of thymidine, the relative desorption yields of the major cation fragments are presented in Figure 8. From the determination of desorption energy thresholds, they found that Ar^+ ions with energy down to 15eV can already cause damage to DNA building blocks.

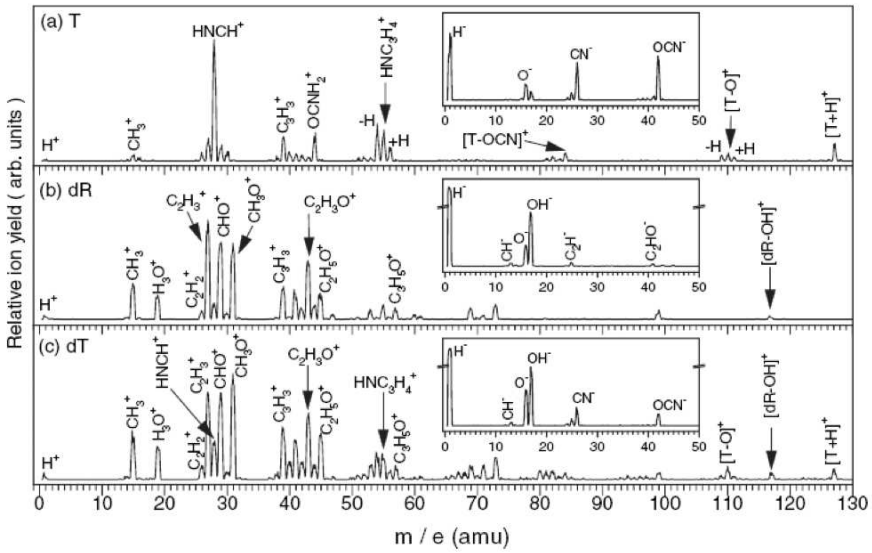

Figure 7. Cation and anion (insets) desorption mass spectra produced by 100 eV Ar^+ impact on films of (a) thymine (T), (b) 2-deoxy-D-ribose (dR), and (c) thymidine (dT), from reference [3].

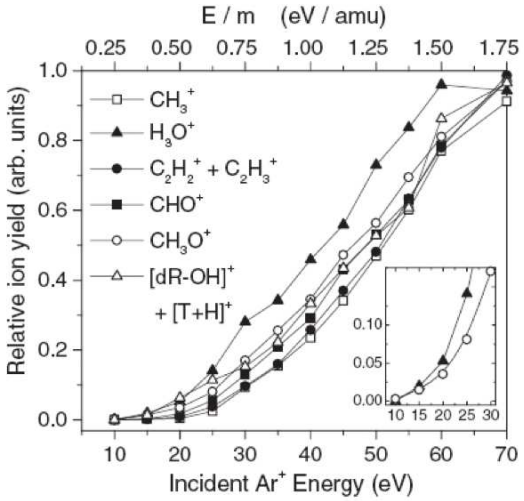

Figure 8. Desorption energy thresholds for cation fragments produced by Ar^+ impact on thymidine films. The inset shows a close-up for H_3O^+ and CH_3O^+. From reference [3].

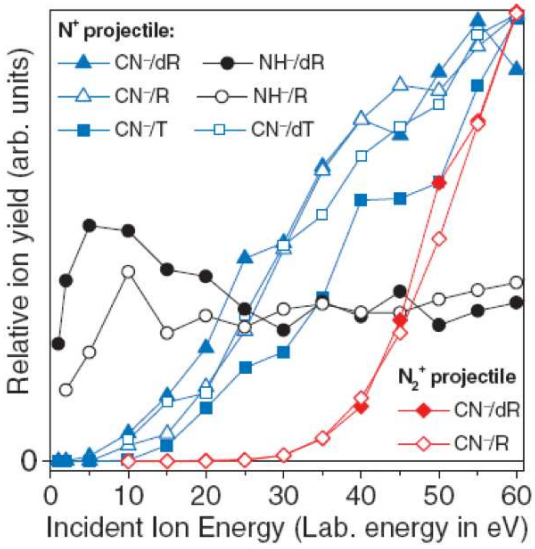

Figure 9. Desorption energy thresholds of NH^- and CN^- anions during N^+ and N_2^+ ion irradiation of 2-Deoxy-D-ribose (dR), D-ribose (R), thymine (T), and thymidine (dT) films on Pt substrate. From reference [25].

In subsequent hyperthermal heavy ion induced DNA component damage studies, Deng *et al.* [25] observed reactive scattering even at incident energies well below 10eV. In the N^+ on 2-Deoxy-D-ribose (dR), and D-ribose (R) film bombardment, reactions including carbon abstraction by N^+ to form CN^+ and hydrogen abstraction to form NH^+ occurred at collision energies down to 10 eV and 1eV, respectively. Hydrogen abstraction from DNA components has also been observed due to the secondary fragments. For example, oxygen fragments O^- at low energy (1 eV) produced by Ar^+ primary beam impact could extract a hydrogen atom from D-ribose (R) to form OH^-.

These recent studies on DNA component fragmentation induced by hyperthermal heavy ion irradiation challenge the traditional view about the mechanism of radiation damage of biological media. These observations underline the important role that might be played by low energy ions at the end of the primary ion track beyond the Bragg peak and the hyperthermal secondary heavy particles produced along the primary ion tracks. These low energy ions can lead to important and complex physical and physicochemical damage to DNA in cells.

I.1.3. Photon induced dissociation of DNA/RNA components

The excitation or ionization by photon irradiation provides another possibility in studying the dissociation of molecules. As an example, employing synchrotron radiation as excitation source in the 6-22 eV energy range, Jochims *et al.* [4] have studied the fragmentation of important

biological molecules (DNA/RNA components: adenine, thymine, and uracil). In their experiments, photoion mass spectra were recorded as a function of the energy of the photons; ionization energies and photoion appearance energies (AEs) were reported and the fragmentation patterns were discussed in detail.

In the case of adenine, the adiabatic value of the first ionization potential was measured to be 8.2eV. The appearance energies of main fragmentation channels were also available in their measurement. For instance, the AEs of fragments $C_nH_nN_n^+$ (n=4, 3, 2) emerged from the successive neutral loss of HCN groups were determined to be 11.56, 12.8 and 13.7eV, respectively. According to the measured AEs, the available thermochemical data, early reported electron impact results [28] and isotopic labeling studies [29-30], main fragmentation pathways of the monocharged parent ion were proposed (as shown in Figure 10). In the first step where one HCN neutral was lost to form the fragment $C_4H_4N_4^+$, the main reaction was expected to occur by the rupture of two bonds, the C2-N3 and N1-C6 bonds (step (1) in Figure 10). Using the measured AEs and heat of formation for involved species, it was also possible to determine the isomer of the fragment. For example, the $C_3H_3N_3^+$ ion was assigned to the 1,3,5-triazine cation (species IIIb in Figure 10) among the three isomeric cyclic 1,2,3-triazine, 1,2,4-triazine and 1,3,5-triazine.

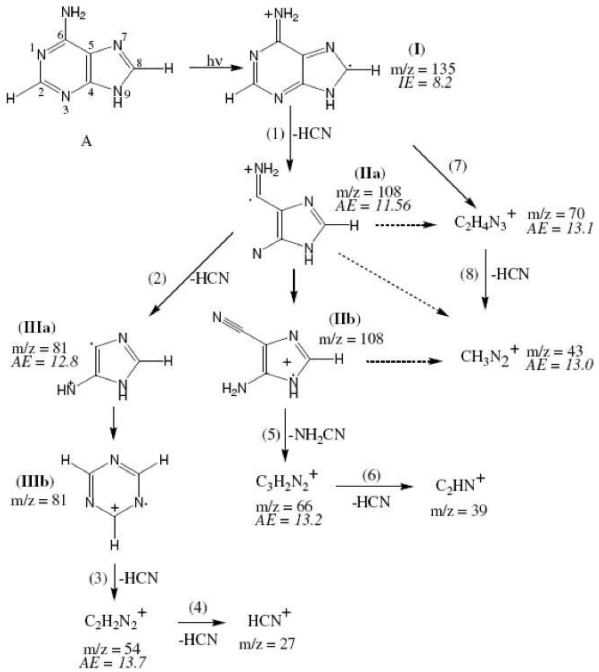

Figure 10. Principal fragmentation decay routes of the adenne radical cation. Measured appearance energy values are given for each fragment (in eV). Roman and Arabic numerals correspond to species and reactions, respectively. From reference [4].

I.1.4. Multi-charged ion on small biomolecule interaction

Multi-charged heavy ion on gas phase small biomolecule interaction is another domain of investigations. Due to the electrostatic field carried by the projectile, in short distance collisions, the target molecule could suffer from a strong electric field of strength, for example, 10^{13} V/m in the case of q=6+ and r=10Å during a very short time range of fs. The first experiment in this growing field was performed by T. Schlathölter and co-workers in 2002. In the works of this group, the fragments are usually analyzed by means of high resolution coincidence time-of-flight spectrometry [2, 23, 31-38].

In the 2 to 120 keV C^{q+} (q=1-6) on RNA base uracil collision studies [31], the effect of the projectile electronic structure and the projectile kinetic energy on the ionization and fragmentation of the molecules was studied. The measurement of the relative fragmentation cross sections as a function of the projectile velocity for each initial charge state has shown a surprising linear decrease with v for C^{2+} rather than an increase for the other cases. This special trend is in contradictory with what was expected using the electronic excitation model of the target molecule due to 'electronic stopping'. In fact, at low v, almost complete fragmentation was observed for C^{2+} projectile whereas for all other projectile charge states the induced fragment cross section was measured to be much lower. This result was interpreted by the unique electronic structure of C^{2+} projectile which allows only the electron capture from the uracil HOMO (highest occupied molecular orbital) at very short ion–molecule separations, leading to extraordinarily strong fragmentation. This first experiment has shown that in ion-molecule interaction, a part from the charge and the velocity of the projectile, the matching between the electronic structures of the projectile and the target molecule might play a crucial role in the interaction dynamics.

More systematic projectile charge effect was studied in the v=0.2 a.u. highly charged ion (Xe^{q+}, q=5-25) impact on gas phase nucleobases (uracil and thymine) experiments [2]. The kinetic energy of atomic fragments was estimated by means of the coincidence detection of correlated fragment pairs from a single molecule. Strong dependences of the fragment kinetic energies on the initial charge state of projectile, subsequently on the charge of intermediate parent ions as well as on the initial chemical environment of the respective fragments within the parent molecule were observed. It was also found that fragment ions with kinetic energies of several tens of eV could be formed; and protons with kinetic energy up to 80eV were observed (as shown in Figure 11).

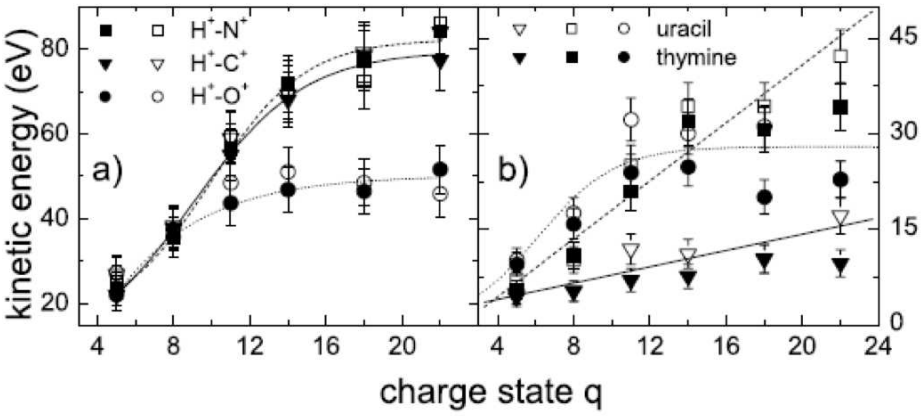

Figure 11. Maximum kinetic energies for the fragment pairs measured in slow highly charged ions (Xe^{q+}, q=5-25) on nucleobases (uracil and thymine) collisions. (a) Proton; (b) heavy ion. From reference [2].

After the experiment of D. Z. Wu *et al* [3], pointing out that deoxyribose might be the relatively weak linking part of the DNA chain upon irradiation, F. Alvarado *et al*. [35] performed experiments using keV H^+, He^+ and He^{2+} impact on isolated gas phase deoxyribose. Comparing the mass spectrum with that of adenine obtained under the same experimental conditions, the striking difference was the relative intensities of the survival parent molecules in the two spectra. For adenine, a very strong parent molecule peak was observed, while for deoxyribose, the parent peak was negligible. This result provided a clear indication concerning the more fragile characteristic of deoxyribose in DNA. In the case of deoxyribose, it was also found that the relative yield of fragment mass distribution n(M) followed a power law, $n(M) \sim M^{\tau}$ (n: number of fragments, M: fragment mass, τ: characteristic exponent) This feature was considered as the fingerprint of statistical fragmentation process.

Recently, F. Alvarado *et al* have measured experimentally the internal energies of deoxyribose dications after proton collisions at 3 and 7 keV [38]. This work has been performed in Lyon during the preparation of this present thesis in cooperation with the group of S. Martin using the CIDEC method (see section I.2). From this experiment, it was found that:

1) the mass spectrum was only weakly dependent on the kinetic energy of the proton projectile for the energy range under study;

2) the most probable excitation energy of the dication deoxyribose prior to the fragmentation was only weakly dependent on the fragment mass, but strongly dependent on the projectile energy (see Figure 12). The authors argued that if non-statistical processes dominated the fragmentation dynamics, the presence of well-defined reaction pathways would have implied a strong dependence of the fragmentation pattern on the excitation energy, consequently on the projectile kinetic energy. The observations in this work were therefore interpreted as indications of

statistical fragmentation processes where the deposited excitation energy redistributed over the vibrational degrees of freedom before the eventual dissociation.

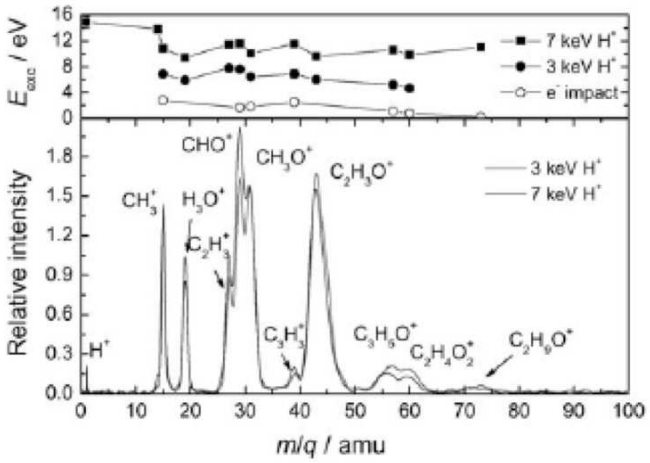

Figure 12. Lower panel: Fragment ion mass spectra from collisions of 3 and 7 keV protons with 2-deoxy-d-ribose. Upper panel: Most probable excitation energy E_{exc} associated to major fragments for different proton impact energies (3 keV and 7 keV) and excitation energy obtained by electron impact ionization. From reference [38].

Besides charged projectiles, neutral projectiles on nucleobase interactions were also studied. Neutral 14keV atomic beams (H, He, and C) on DNA base adenine collision experiments were carried out by F. Alvarado *et al* [37]. When comparing with their corresponding mono-charged projectile impact cases, qualitatively very similar fragmentation pattern was observed for hydrogen and proton projectiles; however for C^0 and C^+, strong differences in relative intensities of the fragment distributions were revealed. Namely, lower relative fragmentation cross section was measured using C^+ than C^0. This was explained as due to the gentle resonant electron capture, only possible for monocharged carbon projectiles.

Since 2005, multi-coincidence technique was introduced in ion-nucleobase interactions by S. Martin and co-workers. In 36keV F^{2+} ion on adenine collision experiment, triple coincidence between the charge selected projectile F^+, the emitted electron number and the fragment ions was performed [39]. The TOF spectrum presented a dominant peak of stable singly charged Adenine and important fragmentation in mainly light fragments. The TOF spectra corresponding to the simultaneous detection of n=0, 1, 2 and 3 electrons were assigned to parent adenine molecules of a well-defined charge state to be 1, 2, 3 and 4 respectively. The strong shift of the population distribution to light mass fragments for increasing number of n suggested that the energy deposition on the target molecule could be important and correlated closely to the number of ejected electrons.

Using highly charged ions, in low energy Ar^{8+} and adenine interactions, S. Martin *et al* [40] have studied in detail the decay mechanism of singly charged adenine which was known until then as dominated by the successive emission of HCN fragments. Employing a mass spectrometer equipped with a specially designed electric field before the time of flight tube, the coincidence measurement of the neutral fragment (HCN) and the residual charged fragments $(C_4H_4N_4)^+$ have been performed. This coincidence detection provided evidence for the delayed emission of HCN in the special electric field corresponding to a time range around 2 microseconds. For adenine with higher excitation energy, the fast loss of a HCN fragment was followed by a subsequent delayed neutral fragment loss from the intermediate parent ion $(C_4H_4N_4)^+$. Coincidence measurement of neutral and charged fragments not only confirmed the delayed loss of the second HCN but also revealed an unknown fragmentation channel i.e., the delayed neutral emission of a H_2CNCN fragment from $(C_4H_4N_4)^+$.

I.2. *Direct measurement of the excitation energy*

It is known that the knowledge of the internal energy of clusters or large molecules is of fundamental importance for understanding its fragmentation dynamics following external excitation. However, to our knowledge, apart from the threshold appearance energies associated to specific dissociation channels, no direct coincidence measurement between internal excitation energy distribution of parent clusters or molecules and fragmentation channels has been performed until 2007. From the retrospect in the previous section we notice that the excitation energy distribution of parent molecular ions before their fragmentation has never been determined or discussed except the case in ref. [38]. This is due to the fact that, for a long time it was difficult to measure this parameter. The main difficulty arises from the absence of a resonance structure in the high continuum energy levels and from the complexity in the energy relaxation mechanism due to the large number of degrees of freedom of such systems [41].

In the case of electron impact or synchrotron radiation, the energy of the incident particle provides a good estimation of the internal energy as long as the energy conversion efficiency from the incident particle to the target is near 100%. It is only the case at the appearance energy that corresponds to the critical energy necessary for the opening of a specific ionization and fragmentation channel [42-43]. When the energy of the incident particle is higher, an increasing and unknown part of the incident energy is carried out by the ejected electrons resulting from the ionization of the target or by the scattered particle. Due to that, the group of S. Martin at Lyon developed an approach, named Collision Induced Dissociation under Energy Control (CIDEC), to

investigate the internal energy distribution of fragmented complex systems beyond the appearance energy of each individual fragmentation channel, and it has been successfully used in C_{60} case [41].

To shed some light on the fragmentation dynamics of interested small biomolecules under the bombardment of charged heavy ions, in this thesis, the CIDEC method has been extended to such systems to determine the excitation energy of the parent ions before its dissociation. In this section, the development and the principle of this method will be presented.

I.2.1. The history of CIDEC method

The concept of the CIDEC method is based on the idea of Double-Charge-Transfer (DCT) spectroscopy. The DCT method was introduced by J. Durup and coworkers in the early 1970s [44-45]. It was developed to measure the electronic-state energies of doubly charged ions, including diatomic, triatomic, and polyatomic molecules (for review see, for example [46]). Principally, DCT is based on the formation of a negative ion by a double electron capture in an inelastic collision between an incident proton H^+ and a neutral molecular target M:

$$H^+ + M \rightarrow H^- + M^{2+}*$$

Equ 1

In this reaction, the kinetic energy of the recoil ion $M^{2+}*$ can be neglected as long as if only scattered anions with diffusion angles near zero degree are considered. The excitation energy deposited in the molecule during the collision is determined by analyzing the kinetic energy loss of the outgoing hydrogen anion H^-. The key point of the method lies on the non-existence of stable excited state of negative ion H^-. If any possible excited states of the anion were populated during the collision, due to fast auto-ionization, their lifetime would be very short (less than 100 ns) and much shorter than the analysis time of H^- (in the order of μs). Therefore, the detected anions result necessarily from collisions in which the ground state of H^- has been populated. This ensures that the energy balance for the reaction, with only 2 bound electrons, is rather simple. The energy defect in Equ 1 (see the figure 13, the channel $H^- + M^{2+}$) can be represented by

$$\delta = IP_1\,(M) + IP_2\,(M) - IP_1(H) - EA(H).$$

Equ 2

In Equ 2, IP_1 (M) and IP_2 (M) stand respectively for the first and second ionization potential of the molecule under investigation, and IP_1(H) and EA(H) represent the first ionization potential

and the electron affinity of the projectile. According to the energy conservation law, the energy to drive the reaction (1) must come from the kinetic energy loss ΔE (or translational energy loss in some references) of the projectile. Under these conditions and if we consider firstly that the recoil ion M^{2+} is populated in the ground electronic state in Equ 1, then the kinetic energy loss ΔE equals to the energy defect δ,

$$\Delta E = \delta = IP_1 (M) + IP_2 (M) – IP_1(H) – EA(H).$$

Equ 3

In the early works where the second ionization potential IP_2 (M) of the target molecule was unknown, when the kinetic energy loss ΔE of the projectile was measured, according to Equ 3, the value of IP_2 (M) could be determined experimentally:

$$IP_2 (M) = \Delta E – (IP_1 (M) – IP_1(H) – EA(H)).$$

Equ 4

In the case where the recoil ion M^{2+} is populated in an excited electronic and/or vibrationnal state, the energy difference between the populated excited state and the ground state of M^{2+} can denoted by E_d (see Figure 13, the channel $H^- + M^{2+*}$). Due to the energy conservation rule, in this case, the kinetic energy loss ΔE of the projectile should equal to the energy defect δ of the collision corrected by E_d :

$$\Delta E = E_d(M^{2+}) + \delta.$$

Equ 5

Using the definition of the energy defect δ (Equ 2), the energy value IP_2'(M), that is necessary to populate higher-lying states of the doubly charged molecular ion M^{2+}* is given in the following expression,

$$IP_2'(M) = IP_2(M)+ E_d = \Delta E – (IP_1 (M) – IP_1(H) – EA(H))$$

Equ 6

The population of such higher-lying states of M^{2+}* will give rise to additional peaks in the measured energy loss spectrum. Thus, by experimentally determining the energy losses for corresponding peaks in a DCT spectrum, the required information on double ionization energies to ground and excited states of doubly charged parent molecular ion can be obtained.

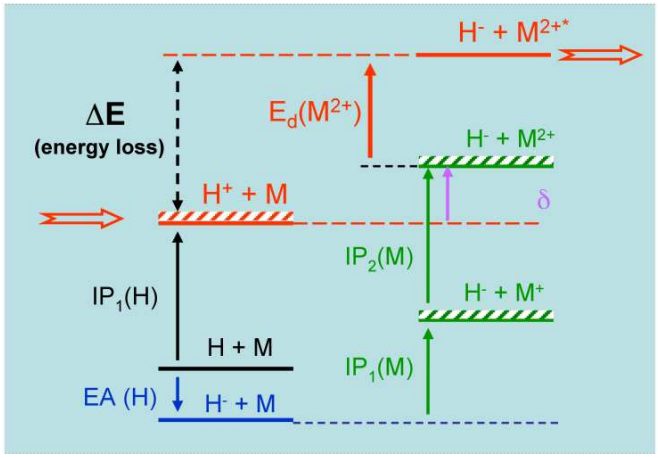

Figure 13. Illustration for energy transfer in proton on molecule collision.

The DCT spectroscopy has been successfully used to measure the double ionization potential of dimer molecules with vibrational resolution (<150 meV), to test the Franck-Condon principle [47-48] (see Figure 14), and to study the electronic-state energies for numerous triatomic and polyatomic doubly charged ions (see, for example [49-52]).

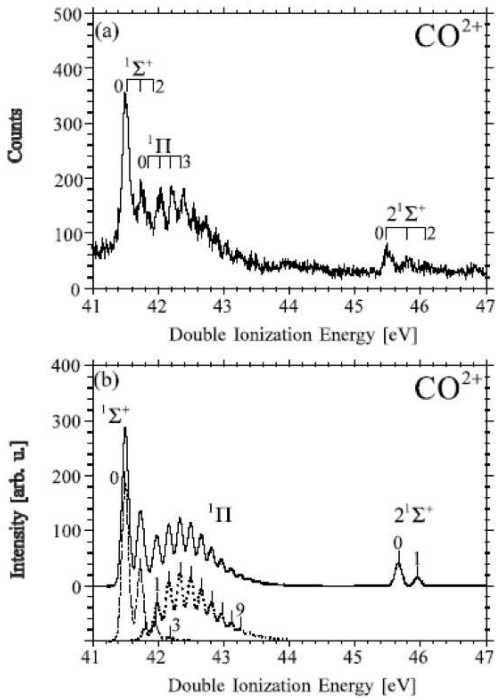

Figure 14. (a) DCT spectrum of CO^{2+}. Bars indicate energy positions determined with threshold photoelectrons coincidence spectroscopy. (b) Calculated Frank-Condon factors assuming the instrumental resolution of 120 meV. Bars indicate theoretical peak positions. From reference [48].

I.2.2. The principle of CIDEC method

As described previously, in DCT experiment, only the kinetic energy loss of the projectile is measured. The CIDEC method is a combination of the DCT spectroscopy and the coincidence analysis of fragment mass spectroscopy and KER (kinetic energy release) spectroscopy [41, 53-54]. In our experiments, both light ions such as H^+ and other heavy ions for instance Cl, F and I, etc. have been used as projectile beams.

In collisions between singly charged ions P^+ at keV energy range and molecules, we select reactions leading to the formation of anions P^-:

$$P^+ + M \rightarrow P^- + M^{2+}*$$

Equ 7

After the primary electron capture process, the doubly charged recoil ions $M^{2+}*$ may undergo auto-ionization and/or dissociation. The energy available for such further evolution corresponds to the energy difference between the populated excited state of $M^{2+}*$ and the ground state of M^{2+} defined previously as E_d (see Figure 13). This energy is called thereafter the energy deposited in the molecule during the collision. It can be determined using Equ 5 as follows,

$$E_d(M^{2+}) = \Delta E - (IP_1(M) + IP_2(M) - IP_1(P) - EA(P)),$$

Equ 8

where $IP_1(M)$ and $IP_2(M)$ denote respectively the first and the second ionization potential of the target molecule (M) and $IP_1(P)$ and EA(P) the first ionization potential of the projectile (P) and its electron affinity.

The evolution of the target molecules $M^{2+}*$ is then studied as a function of the deposited energy $E_d(M^{2+})$ in the molecules by measuring the kinetic energy loss of the scattered projectile anions P^-.

The measurement is performed in triple coincidence event-by-event mode. It includes the charge and kinetic energy analysis of the projectiles, the time-of-flight spectroscopy of the recoil ions (both parent ions and fragments) and the detection of the number (n) of ejected electrons. The fragmentation patterns of the recoil molecular ions are determined from the time-of-flight spectrum in coincidence with the measurement of E_d.

In some collision systems, the doubly charged molecules may lose one or more electrons before the fragmentation allowing for the study of the fragmentation patterns of triply or other multiply charged molecules. In such cases, it is essential to have the knowledge of the charge state

of the parent recoil ions (M^{r+}) prior to the fragmentation. In our experiments, this parameter can be determined by the electron number conservation rule, r=2+n.

Therefore, merging the two techniques DCT spectrometry and the triple-coincidence measurement, the CIDEC method can be employed to investigate the population distribution for each dissociation channel as a function of the excitation energy of the parent molecular ions at a well-determined initial charge state.

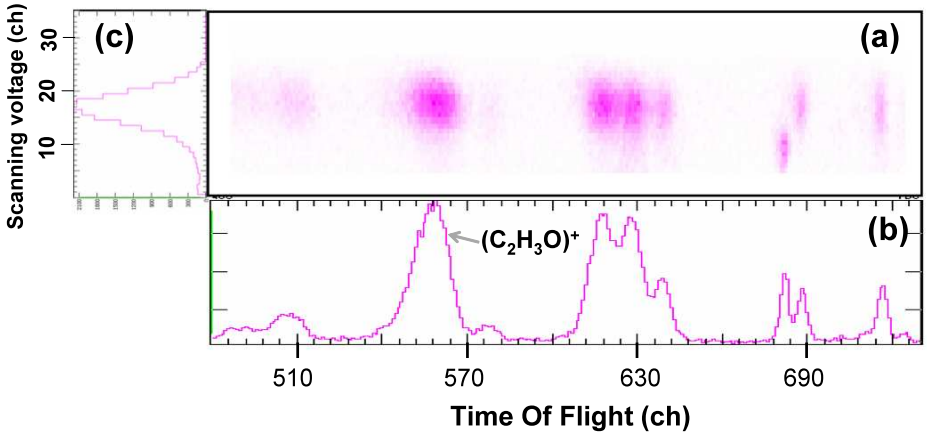

Figure 15. Typical spectra obtained in CIDEC measurement for 3keV F^+ on deoxyribose collision, the scattered projectile was charge selected as negative ion F^-: (a). Correlation spectrum between outgoing projectile and recoil ions; (b). TOF spectrum of recoil ions: the projection from (a) onto the horizontal axis; (c). Population distribution of the parent ions as a function of the excitation energy: the projection from (a) onto the vertical axis.

As an example, typical spectra obtained in CIDEC measurement between 3keV F^+ and isolated gas phase deoxyribose ($C_5H_{10}O_4$) collisions are presented here (Figure 15). Figure 15 (a) is a correlation spectrum obtained in coincidence measurement between the charge selected outgoing projectiles F^- and the recoil fragments. The horizontal axis corresponds to the time-of-flight (TOF) of the recoil ions, and the vertical axis the scanning voltage of the analyzer for the kinetic energy analysis of the anions F^- (which can be transferred into excitation energy of the parent ions, see details in section II.3). According to the monitoring of the ejected electron number, it was found that nearly no electron was detected for this collision system. It means that the fragmentation spectrum measured in this experiment results predominantly from the doubly charged molecular ions $(C_5H_{10}O_4)^{2+}$. Figure 15 (b) is obtained by the projection from the spectrum (a) onto the horizontal axis. From this TOF spectrum, all fragmentation channels can be determined and the dominant one is assigned to the fragment $(C_2H_3O)^+$. Figure 15 (c) is the projection onto the

vertical axis of the spot in Figure 15 (a) associated to the selected fragment $(C_2H_3O)^+$. It provides the so-called population distribution for this dissociation channel as a function of the excitation energy of the parent doubly charged molecular ions $(C_5H_{10}O_4)^{2+}$.

I.3. *The interested molecules in this thesis*

Two objective biomolecules are involved in this work, i.e., Adenine and meso-tetraphenyl iron (III) porphyrin chloride. Both are of fundamental importance in biological system, and they will be introduced in the following.

I.3.1. Adenine: one of the DNA building blocks

DNA is a nucleic acid that carries the genetic information in the cell. In structure, DNA consists of two long chains of nucleotides twisted into a double helix and joined by hydrogen bonds between the complementary bases adenine and thymine or cytosine and guanine. The alternating phosphate and sugar (2-deoxyribose) make up of the backbone of the DNA strand. The segment of unfolded DNA molecule is shown in Figure 16.

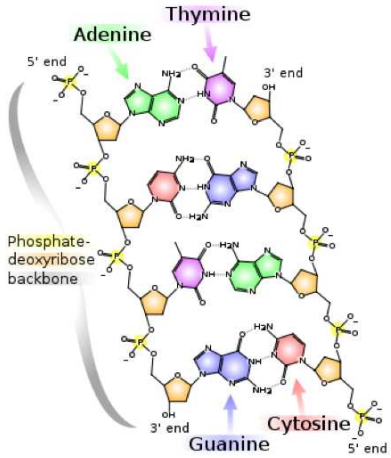

Figure 16. Part of DNA structure.

Adenine (Ade: $C_5H_5N_5$, m=135) is one of the constituents of DNA involved in base pairing with thymine. The structure of the isolated adenine is shown in Figure 17. As mentioned previously, the recent extensive investigations on the dissociation of Adenine have been motivated by its essential role in the understanding of the damage dynamics of DNA upon

irradiation. Another interest of adenine investigation lies in the astrobiology and exobiology. As a matter of fact, traces of nucleobases and life-base molecules have been found in meteorites [55-57], cometary grains [58-60], and interstellar regions [61-62]; It is still unclear how these molecules could be formed and survived in interstellar conditions. This leads to intensive searches of interstellar molecules potentially interesting for astrobiology as well as speculations on the possible mechanisms involved in the formation of these molecules [63-64].

Many studies on the dissociation of charged adenine in the gas phase are available. As early as in 1967, J. M. Rice and G. O. Dudek [28] performed experiments on electron-Ade collisions at 70eV. In this pioneer work, the mass spectrum revealed a successive loss of neutral HCN (m=27) from Ade^+ ionized due to the electron impact leading to the formation of the daughter ions m=108, 81, and 54. The electron impact induced fragmentation of the isotopically labeled Adenine molecules provided precise information on the location of bond rupture for fragment release for dominant dissociation channels , e.g., the first HCN loss occurs by the rupture of the C2-N3 and N1-C6 bonds [29-30]. More fragmentation pathways, for instance, the evaporation of NH_3 etc, have been reported in collision-induced dissociation (CID) of protonated adenine [65]. More recently, H. W. Jochims and co-workers [4] have studied the photo induced fragmentation pathways of adenine by using synchrotron radiation in energy range 6-22eV (see also section I.1.3). The adiabatic ionization energy and the ion appearance energies for main decay channels have been determined in higher accuracy than previous works.

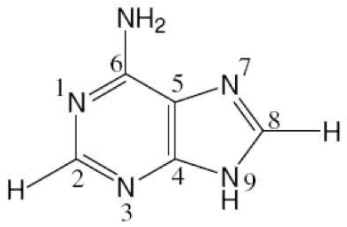

Figure 17. The structure of the isolated adenine molecule.

In the studies of ion on isolated gas phase adenine collisions [37, 39, 66], similar as in electron and photon impact experiments, successive emission of neutral HCN groups were observed as the main decay channels of the singly and doubly charged parent ions. However, the coincidence technique employed in ion impact experiments allowed the observation of other possible fragmentation patterns, even those with very low statistics. We can mention here the observation of delayed fragmentation channels using a special coincidence detection method between charged and neutral fragments [40]. It is also noticeable that in the work of Lyon [39], where the present thesis was prepared, the importance of energy deposition on the Ade molecule was evoked

already several years ago (see also section I.1.4). In some sense, the present study is a continuous work of these multi-coincidence experiments.

In this work, based on the CIDEC method, the population distribution of the doubly charged parent ion Ade^{2+} was measured as a function of the excitation energy. It is expected that the internal energy measurement could provide additional information on the fragmentation dynamics of the adenine molecule.

The CIDEC method is based on the negative ion production of the outgoing projectile via electron capture from the target. To extend this method in collisions with adenine, one of the essential questions is to know if the negative ion production yield is high enough to perform coincidence measurements. To answer this question, a special arranged experiment was performed to measure directly the negative ion production yield.

I.3.2. Porphyrins: the pigment of life

A porphyrin is "any of a group of compounds containing the porphin structure of four pyrrole rings connected by methine bridges in a cyclic configuration, to which a variety of side chains are attached; usually metalled, e.g., with iron to form heme." [67]. Porphyrin and its derivatives are one of the most important pigments in nature. A large variety of tetrapyrrolic pigments exist with the similar ligand core, but differ in the metal center and the side groups attached to the marcrocycle porphyrin rings. The metal center can be an iron (heme), a magnesium (chlorophyll) or cobalt (vitamin B12) [68]. Many vitally important functions in living systems are carried out by such metalloporphyrins, for example, haem is responsible for oxygen transport, cytochrome for electron transport and, most fundamentally, chlorophylls for photosynthesis [69-70]. Thus the porphyrins can fairly be called the pigments of life. Except for the fundamental importance in the numerous biological processes, metalloporphyrins are also of prime importance in chemical catalysis and as geological markers. They are even used in photodynamic tumor treatment [71-72]. Due to the high molecular symmetry and remarkable chromophore structures, metalloporphyrins are also theoretically attractive for physicists and chemists [68].

In the present work, an iron ligand metalloporphyrin molecule, i.e., meso-tetraphenyl iron (III) porphyrin chloride, is employed as target molecule. It has a formula of $C_{44}H_{28}N_4FeCl$ and the mass m=704. In the following, it is denoted as FeTPPCl. The structure of the FeTPPCl molecule is shown in Figure 18.

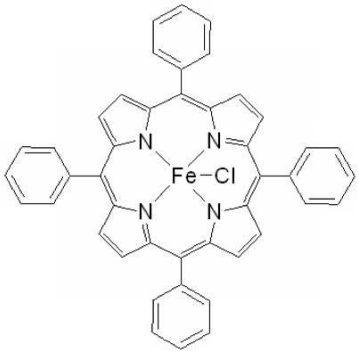

Figure 18. The structure of the FeTPPCl molecule.

Previously, the FeTPPCl molecule was impacted by low energy electron (see also section I.1.1.2), and mass spectra and AEs of some fragments were reported [4]. Multi-charged ion on FeTPPCl collision was also investigated [73], where the total mass spectrum (without the selection of outgoing projectiles or ejected electron numbers) was reported and compared with the electron impact case. Recently, the electrospray ionization (ESI) tandem mass spectrometry was employed to study the multi-collision-induced dissociation (CID) process of monocharged $(FeTPP)^+$ ions [74]. Decay pathways were probed as a function of the collision offset voltage and the onset voltages for observed pathways were determined. Unfortunately, in the ESI/CID experiment, the energy conversion efficiency is unknown, thus the energy deposited into the target during the collision could not be determined.

In this work, multi-coincidence technique was employed to study the fragmentation pattern of FeTPPCl molecule induced by multi-charged heavy ions. Similar to Adenine, the population distribution of the doubly charged parent ion $(FeTPPCl)^{2+}$ was also measured as a function of the excitation energy, to study how the additional energy (the energy deposited on the target molecule during the collision) drove further fragmentation of the parent ions.

I.4. *Outline of this thesis*

The thesis is organized as follows:

Here in chapter I, we introduced a multi-disciplinary attractive topic relevant to the fragmentation of small biomolecules under excitation or ionization. The experimental advances about this topic were briefly reviewed. The principle of a novel method to measure directly the internal energy during a collision, i.e., the CIDEC method, employed in this dissertation, was described. The interested target molecules and topics addressed in this thesis were also introduced.

In chapter II, the whole structure of the experimental setup will be described in details, including the electron cyclotron resonance ion source (ECRIS), and the experimental terminals in Lyon and Lanzhou involved in this thesis. The principle of data analysis and energy calibration with the CIDEC method will be also presented.

Chapter III will be devoted to the presentation and discussion of experimental results concerning the target molecule adenine. Direct measurement of the negative ion production yield in collisions between F^{2+} at 30keV and Ade will be presented first. Then the fragmentation of Ade^{2+} under energy control will be investigated using the CIDEC method with Cl^{+} projectiles at 3 keV.

In chapter IV, the fragmentation of FeTPPCl molecule will be studied. First, under slow multi-charged heavy ion bombardment, Kr^{8+} beam at 80keV, the fragmentation pattern of FeTPPCl will be investigated by means of multi-coincidence technique. Then the fragmentation pathways under energy control will be studied using the CIDEC method with H^{+} and F^{+} projectile impact at 3 keV.

Finally in chapter V, a summary and conclusions about the experimental investigations presented in this work will be given.

Chapter II Experimental Setup

In this chapter, details of experimental setup will be presented. Since this is a joint supervised thesis between the LASIM at Lyon-1 University in Lyon and the Atomic Physics group-1 (AP1) at the Institute of Modern Physics in Lanzhou, the equipments of both sides were involved. In addition, a part of works of this thesis was carried out in GANIL by using the slow highly charged ion beams delivered by the ARIBE facility and the target chamber of the Lyon group transported from Lyon to Caen. In all experiments, we used ion beams produced by electron cyclotron resonance ion sources (ECRIS). Thus, to begin, the principle of ECRIS will be briefly introduced; the projectiles employed in the experiments will also be given. The second section of this chapter is devoted to detailed descriptions of the setup in Lyon, including a general view of multi-coincidence measurement and presentation of individual components. In the section 3, the setup of Lyon working at the mode of CIDEC method will be presented. The data analysis procedures will be given at the end of this section. In section 4, the setup in Lanzhou, aiming at measuring the production yield of neutral and negative outgoing projectiles, will be presented. This chapter will be ended with a summary in section 5.

II.1. *Ion source*

Originated from studies on magnetic mirror machines for fusion research, the first operational ECRIS was built by Geller in Grenoble (1974) [75]. Since then, there has been a rapid improvement of the performance concerning the achievable charge states as well as the intensity of beams. Due to the very good properties: high charge state production, high beam current and stability, wide range of species, reliability, and ease of operation , it has been intensively used in collision experiments between highly charged ions and atoms, molecules, clusters, surfaces and solid targets. Recent progress on ECRIS can be found in ref [76], and here only the principle of this instrument will be described.

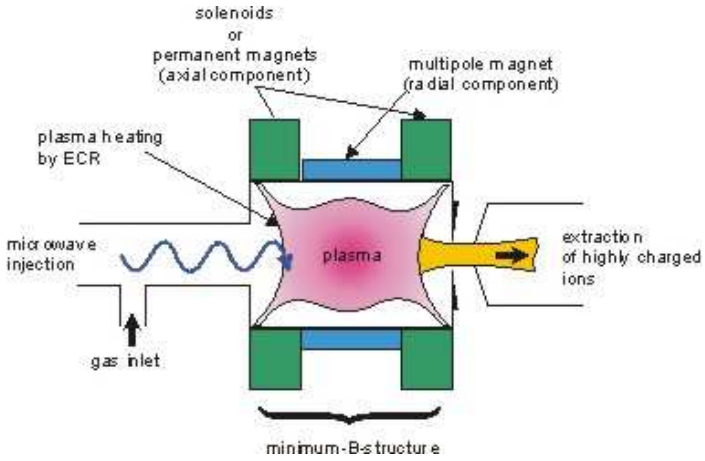

Figure 19. The principle of an ECRIS [77].

The principle of ECRIS is schematically shown in Figure 19 and simply described as follows:

When electrons move in a magnetic field they gyrate around the magnetic field lines due to the Lorentz force. The gyration frequency is called the cyclotron frequency ω_{cyc}. If a microwave radiation of the same frequency propagates into such a region, the electrons are resonantly accelerated and absorb energy from the microwave radiation. The electron cyclotron resonance condition is therefore given as follows:

$$\omega_{hf} = \omega_{cyc} = (e/m) \times B$$

Equ 9

Here, e and m denote respectively the charge and mass of the electron and ω_{hf} the angular frequency of the microwave.

The confinement of the plasma electrons in an ECRIS is achieved by means of a magnetic bottle. It is a superposition of an axial magnetic field component produced by solenoids or permanent magnets and a radial component provided by a multipole magnet. This results in a so-called minimum-B-structure: the magnetic field has a minimum in the middle of the structure and from there it increases in all directions to ensure the electron confinement with the magnetic field mirror effect. A closed surface is created where the electron cyclotron resonance condition is fulfilled. Electrons passing through that surface can be accelerated resonantly. Furthermore, a high mirror ratio of the magnetic field leads to long confinement times for the plasma electrons. They can pass the resonance region very often, gain high energies and ionize plasma atoms and ions into high charge states via successive single ionization-collisions.

On the other hand, the ions in the plasma are not accelerated and remain in thermal motion, because the cyclotron resonance frequency of such particles is much lower than that of electrons due to their heavy mass and therefore stay far from the resonance conditions (formula $Bq/M << \omega_{cyc}$). They are not confined by the magnetic field but by the space charge potential of the electrons. The plasma magnetic confinement, however, is not perfect and electrons can escape from the plasma, for example in axial direction. Since the plasma tends to stay neutral, some ions will follow the electrons. By using a suitable extraction system and by applying a high voltage, ions can be extracted from the ion source to form high charge state ion beams.

The key parameters that influence the source stability and beam intensity are the gas pressure and the microwave power. The energy resolution of the beams depends strongly on the source stability. So, in experiments where beams with high energy resolution are needed, special empirical values of the gas pressure and microwave power were set after numerous tests.

In this work, slow ion beams Cl^+, H^+, and F^+ at 3keV were delivered by a NanoGan III in Lyon mainly for experiments with excitation energy measurement; slow highly charged ion beams Kr^{8+} at 80 keV were delivered by ARIBE at GANIL in Caen for multi-coincidence measurement; and slow ion beams F^{2+} at 20 keV delivered by LECR3 in Lanzhou were employed for direct measurement of neutral and negative ion production yield.

II.2. *Multi-coincidence measurement*

In collisions between slow highly charged ions and molecular targets, electron transfer from the target to the projectile ion is the predominant interaction process. Having lost r electrons, the target molecule becomes charged and may undergo further dissociation. To determine without ambiguity the charge state of the parent recoil ions M^{r+} prior to the fragmentation, a setup with triple coincidence measurement between the charge-analyzed projectile, the time-of-flight of the recoil ions and the number of ejected electrons had been developed in the group of Lyon [78-81]. For a collision with the initial projectile charge state of (q), from the analysis of the final charge state (q') of the scattered projectile, the number of electrons (s) captured and stabilized on the scattered projectile ion can be obtained with ($s = q - q'$). By measuring in coincidence the number (n) of electrons ejected in the continuum, we can

determine the number of electrons active in the electron transfer process by the electron number conservation rule (r = n + s) and therefore the initial charge of parent recoil ions before fragmentation M^{r+}.

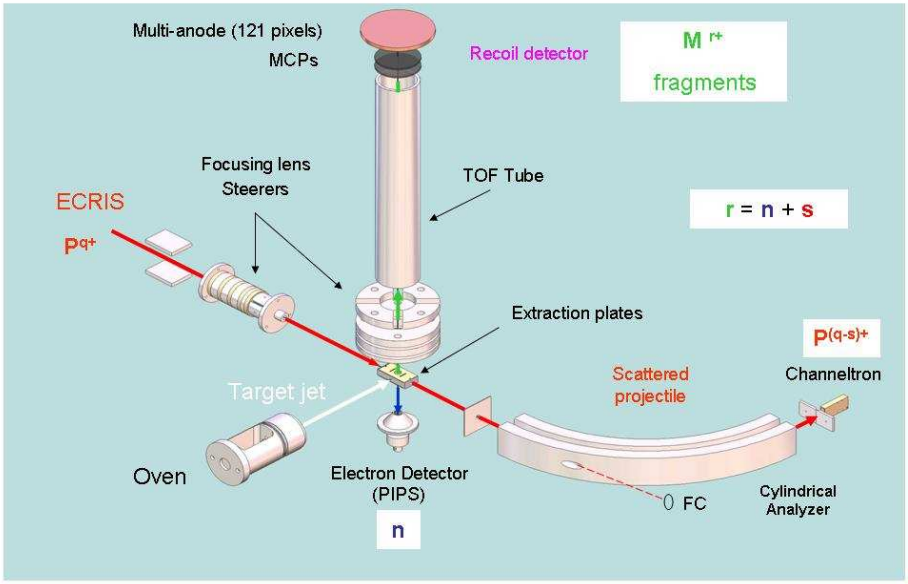

Figure 20. A general view of the experimental setup in Lyon (see the detailed description in the text).

A schematic of the experimental setup in Lyon is shown in Figure 20. The projectile ions P^{q+} were delivered by the ECRIS. After being focused and driven by a lens and steerers, and well collimated by an entrance slit of 200μm, the beam was sent into the collision chamber and crossed perpendicularly an effusive target jet evaporated from an oven. After collision, emitted electrons and recoil ions (parent ions or charged fragments) were extracted from the interaction region in opposite directions by a transverse electric field. The electrons were accelerated at 18keV and detected by a Passivated Implanted Planar Silicon (PIPS) detector. The recoil ions were analyzed by a TOF spectrometry, and detected by a position sensitive detector equipped with two multi-channel plates (MCPs) and a multi-anode. The final charge of the outgoing projectiles was analyzed by a cylindrical electrostatic analyzer. The experiments were performed using an event-by-event mode with coincidence data acquisition of the amplitude of the PIPS signal (proportional to the electron number) and the TOF of all detected recoil ion fragments triggered by the detection of a charge-selected projectile.

In the following, detailed information related to the three parts, i.e. the detection of recoil ions, the analysis of outgoing projectile and the counting of the ejected electron number, will be presented.

II.2.1. The detection of the recoil ions

Configuration The recoil parent ions or charged fragments emerged in the collisions were analyzed by the TOF spectrometer and detected by recoil detector equipped with two pieces of MCPs and a multianode of 121 pixels.

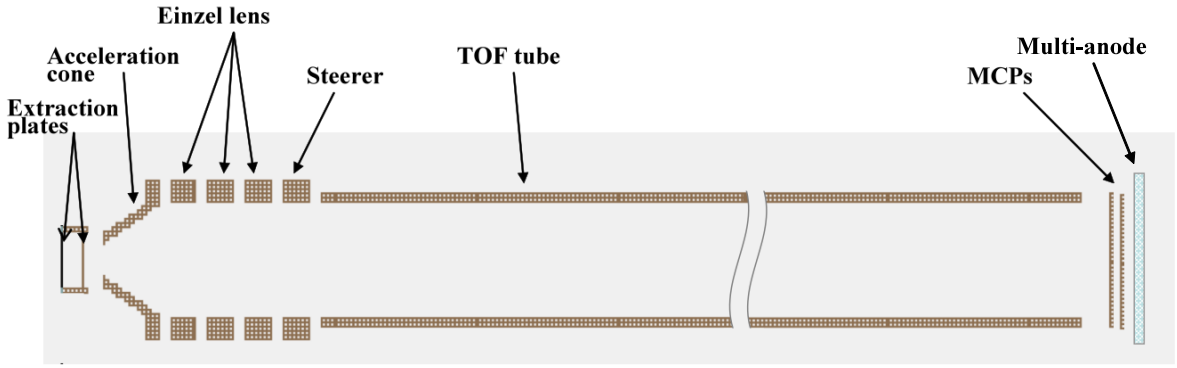

Figure 21. The TOF configuration. Except for the extraction plates, all electrodes have cylindrical symmetry.

The TOF spectrometer arrangement is shown in Figure 21. The two extraction plates separated by a distance of 8mm were biased to U_{Ext1} and U_{Ext2}, respectively. After the extraction region, the ions were accelerated over 7mm until the cone-shaped electrode (acceleration cone), which was biased to U_{Tube}. The TOF tube with length of 845mm was set to the same potential as that of the acceleration cone. To improve the collection efficiency, between the acceleration cone and the TOF tube, an einzel lens and a set of steerers were employed to focus and drive the recoil ions. The einzel lens was composed of three ring-shaped electrodes; the first and third ones were both polarized to the same potential $U_{ring,\ s}$, and the central one to $U_{ring,\ c}$. The steerers were set to $U_{Steerer}$. Except for the extraction plates, all electrodes have cylindrical symmetry. At the end of the TOF tube, two MCPs were employed to detect the recoil ions. To improve the detection efficiency, the recoil ions were post-accelerated with a voltage of 3.4kV toward the MCPs. A multi-anode composed of 121 pixels and their individual amplifiers and discriminators was mounted after the MCPs to differentiate fragments hitting the MCPs at the same time while differing in positions. In the multicoincidence measurement in Caen, to improve the mass resolution of the recoil ion, strong extraction field was arranged (500V/cm); while in the CIDEC measurement in Lyon, to

ensure the best compromise between a good kinetic energy resolution of the scattered projectile and a sufficient mass resolution on the recoil ion, a relatively low extraction field (25V/cm) was optimized. The voltages of the TOF components are listed in Table 1.

Table 1. The voltages of the TOF components in multicoincidence measurement and CIDEC measurement.

	U_{Ext1} (V)	U_{Ext2} (V)	U_{Tube} (V)	U_{Lens} (V)		$U_{Steerer}$ (V)
				$U_{ring,s}$	$U_{ring,c}$	
Multicoincidence measurement	-400	-800	-2000	-2000	-3000	-2500
CIDEC measurement	-90	-110	-3000	-3000	+800	-3000

Assignment of the TOF spectrum According to the arrangement of the TOF spectrometer, the flight time of the recoil ions from collision region to MCPs is proportional to the square root of its mass over charge ratio, i.e.,

$$t \sim (m/q)^{1/2}$$

Equ 10

From this relation, for each peak on the TOF spectrum, its mass over charge value *(m/q)* can be determined precisely. As an example, Figure 22 presents a typical TOF spectrum of recoil ions, which was measured in I^{2+} on background gas (residual air) collisions at 6keV. In Figure 22, horizontal axis stands for the time-of-flight of the recoil ion which is shown in channel, and the vertical axis for the counting numbers.

To assign unknown charged elements detected in this experiment, in the first step, we have to calibrate the spectrum using at least three well-identified species. For instance, in the present case, the water, hydrogen, and nitrogen molecular ions are expected to occur with relatively high intensities. By performing a Gaussian fitting for corresponding peaks on the recorded TOF spectrum, the central positions of these peaks can be determined. The square root of m/q ratio for these "known" species can be obtained easily (The values of square root of m/q for H_2O^+, H_2^+, and N_2^+ ions in this example are listed in Table 2). The measured flight time (in channel) of these molecules are plotted as a function of their $(m/q)^{1/2}$ (Figure 23). A linear fitting is applied on the data of Figure 23. Considering the theoretical linear relation between the flight time and $(m/q)^{1/2}$, a good fitted straight line is expected (see Figure 23). In mathematics, whether the linear fitting is good or not is described by a correlation coefficient R. The square of R is a variable between 0 and 1. The higher the R^2 value, the better the linear correlation between the data. To the limit, when $R^2 = 1$, it means a perfect linear fitting. When the TOF spectrum is well calibrated, one can precede the identification of unknown species. First, the central positions of the unknown peaks on the TOF spectrum are measured. Using

the obtained linear formula of the fitted straight line inversely, the m/q ratio for the ions corresponding to each peak is determined. Then the TOF spectrum is assigned. In this way, the small peak next to N_2^+ is assigned to O_2^+, and the small peak at the foot of H_2O^+ is assigned to OH^+.

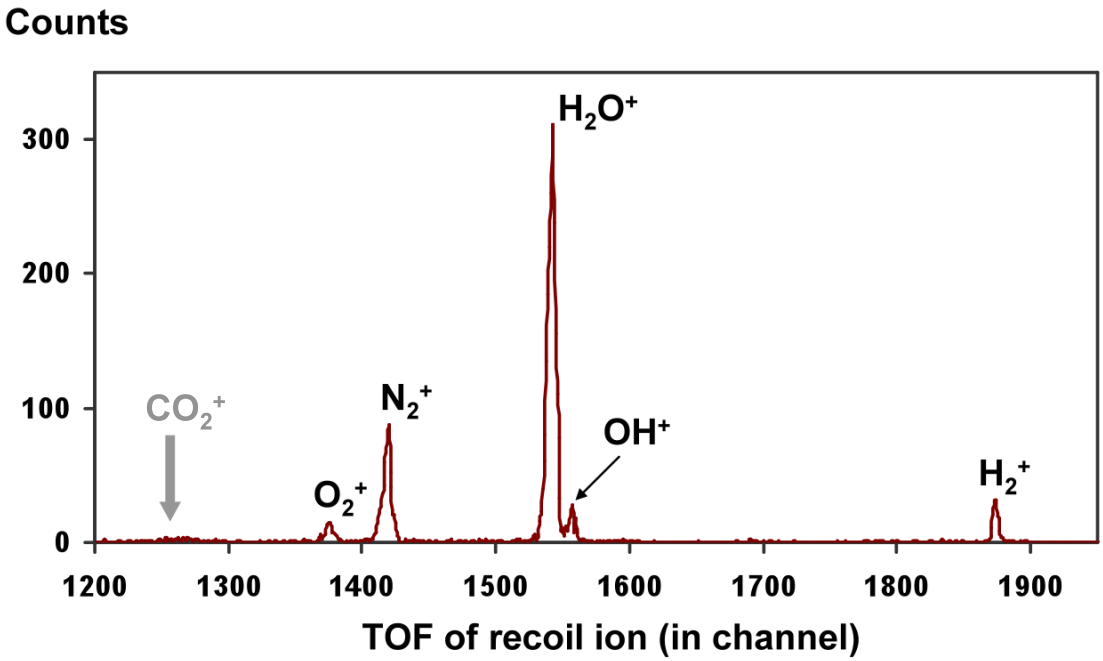

Figure 22. Spectrum for illustrating the "assignment of the TOF spectrum". It was measured in I^{2+} on air collisions at 6keV. As the result of assignment, the species of the recoil ions are labeled on the spectrum. The gray arrow denotes the nominal position of ion CO_2^+.

Exploiting the formula of the fitted straight line, one can also determine the nominal center of recoil ions with a given mass and charge state. For instance, in this case, another possible ion CO_2^+ is expected to appear at about channel 1261, as shown by the gray arrow in Figure 22. This method will be useful in chapter IV for spectrum deconvolution (see IV.3.3).

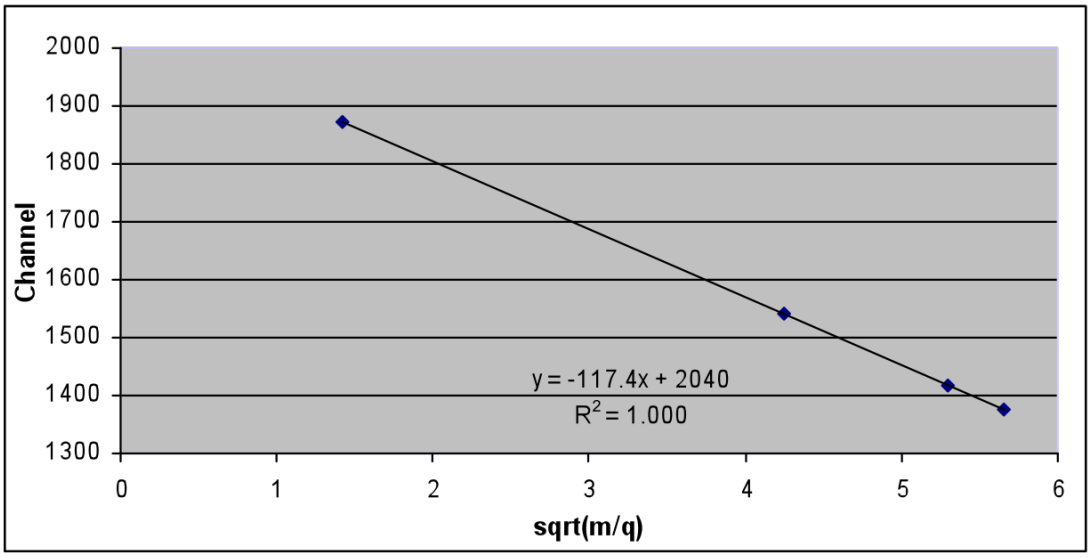

Figure 23. The flight time of recoil ion (in channel), plotted as a function of its $(m/q)^{1/2}$. The fitted straight line, along with its formula and the value of the square of the correlation coefficient (R^2), is presented.

Table 2. Data used in the example of TOF spectrum assignment. The position is the central position of the peak obtained by performing a Gaussian fitting on the recorded TOF spectrum. Fitting is the calculated nominal position of the recoil ions.

Species	Mass	Charge state	sqrt(m/q)	Position (ch)	Fitting (ch)
H_2^+	2	+1	1.414	1874	1874
H_2O^+	18	+1	4.243	1542	1542
N_2^+	28	+1	5.292	1418	1418
O_2^+	32	+1	5.657	1376	1376
CO_2^+	44	+1	6.633		1261

II.2.2. Analyzer system

For the final charge state and kinetic energy loss determination of the outgoing projectiles, a cylindrical electrostatic analyzer system was employed, which is mainly composed of two parts: a 90^0 cylindrical electrostatic analyzer and a channeltron, as shown in Figure 24.

The cylindrical electrostatic analyzer has a radius of R_{center} = 205 mm for the center, R_{in} = 200 mm for the inner sector, and R_{out} = 210 mm for the outer sector. The incident beam was focused around the center of the collision cell, which was considered as the object point of the analyzer. An Exit slit with a width of 200μm was placed at the image point of the analyzer just in front of the ion detector in order to improve the energy resolution. The slit 1 placed

before the analyzer was to limit the scattering angle of the ions. The two sectors of analyzer were connected to a power supply with two output voltages ranging from 0 to ± 6.5kV, which can be scanned by a control and acquisition program. For positive ion analysis, depending on the final charge state and kinetic energy, the inner and outer sectors were biased to a negative voltage V_- and a positive voltage V_+ respectively. For negative ion analysis, the polarities of the two sectors were reversed.

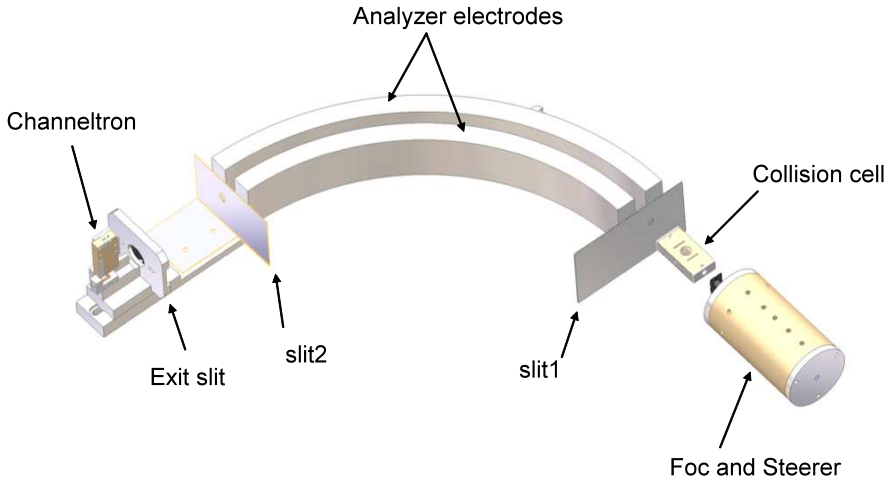

Figure 24. The scheme of the electrostatic analyzer

According to the Gaussian theory and considering scattered ions flying along the central trajectory of the analyzer, the kinetic energy E_k of the detected ions is related to the absolute value of their charge state *(q')* and the potential difference voltage between the two sectors of the analyzer *($V=V_+ - V_-$)* as follows:

$$E_k = \frac{q'V}{2} \Big/ \ln\left(\frac{R_{out}}{R_{in}}\right)$$

Equ 11

After the deflection by the analyzer, the selected ions hit, at 45° incidence angle, a grounded copper cylinder of 5 mm in diameter placed at 10 mm behind the exit slit. Secondary electrons sputtered from the copper surface were detected by a channeltron biased at +3kV, and the signals were transmitted to subsequent electronic units and the acquisition system. When the channeltron high voltage supply was switched off, the copper cylinder could be connected to a pico ampermeter and used as a Faraday cap for the primary beam current detection. This arrangement was convenient to optimize the beam transport conditions in order to improve the energy resolution of the analyzer.

II.2.3. The electron detection system

In the opposite side of the recoil ion detector, a semi-conductor detector PIPS polarized at 18kV was employed for electron detection. The configuration of the electron detector is shown in Figure 25. The distance from the front surface of the PIPS to the collision center was about 50mm. In order to collect all emitted electrons, an intermediate electrode (Nose) biased at +360V was used and placed in between the PIPS and the interaction region. To reduce the detection of the electrons coming from the surfaces, a steel hat, with a hole of 5mm in diameter, was mounted above the PIPS. When several particles hit simultaneously the PIPS detector, the PIPS delivers a signal of amplitude proportional to the total energy deposited by the particles. In the experiments, all electrons ejected in a collision are accelerated to the same kinetic energy; the amplitude of the output signal is then proportional to the number of detected electrons. In the measurement, the signal of the detector PIPS was amplified and sent to an analog-digital converter (ADC 811) for pulse-height analysis in order to determine the number of emitted electrons in the collision.

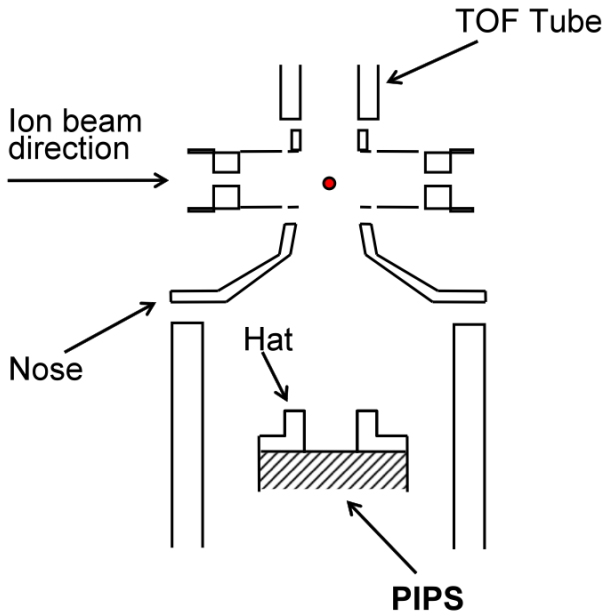

Figure 25. Arrangement of the electron detection system.

II.3. *Excitation energy measurement with the CIDEC method*

As exposed in the chapter I, the CIDEC method combines the DCT method with a coincidence technique [41, 53-54]. The experimental setup is based on the multi-coincidence collision chamber described in II.2 with a special improvement for scanning the analyzer voltage under the best energy resolution conditions. It works as follows:

After a single collision, all emerged electrons and recoil ions were detected as in II.2. The cylindrical electrostatic analyzer was employed here for analyzing both the final charge state and the kinetic energy of the outgoing projectiles. The analyzer voltage was scanned step by step over the whole peak of the projectile anion in order to analyze the kinetic energy loss. For each scanning step, we performed an event-by-event data acquisition with an identical time interval. For each event, three types of data were recorded in a data file, the scanning voltage of the projectile analyzer, the amplitude of the PIPS signal and the TOF of all detected recoil ion fragments.

II.3.1. Energy resolution of the electrostatic analyzer and energy dispersion of the primary beam

In experiments using the CIDEC method, the precision of kinetic energy analysis depends sensitively on the energy resolution of the analyzer and the energy dispersion of the primary beam. The primary beam energy dispersion depends strongly on the stability of the ECRIS and the stability of the beam delivery and transport elements, such as the beam extraction voltage and the magnet, etc. On the other hand, the instrumental resolution of the analyzer depends on the beam focusing conditions, on the width of the exit slit and on the scanning step of the analyzer. It can be optimized by adjusting the parameters of lens and slits.

As an example, the voltage of the lens before the entrance of the collision cell (Figure 24) is a critical and adjustable parameter. It determines the focusing point of the beam and therefore the size of the beam at the Exit slit of the analyzer. To optimize this parameter, a primary projectile beam Ar^+ at 3keV was analyzed with the cylindrical analyzer. The full width at half maximum (FWHM) of the peak given in analyzer scanning channels was measured as a function of the voltage applied to this lens. The result is shown in Figure 26. Fitting the data by using a parabola function, we obtained an optimized lens voltage of 1.33kV corresponding to a minimum FWHM of the analyzed primary beam, i.e. the best

focalization condition. Under this condition, the beam is first focused at the collision point by the lens. This point and the exit slit hole are conjugate points for the analyzer. Therefore, the size of the beam is minimized at the position of the Exit slit. Using a narrow slit, we can reduce as much as possible the optical broadening of the analyzed peak.

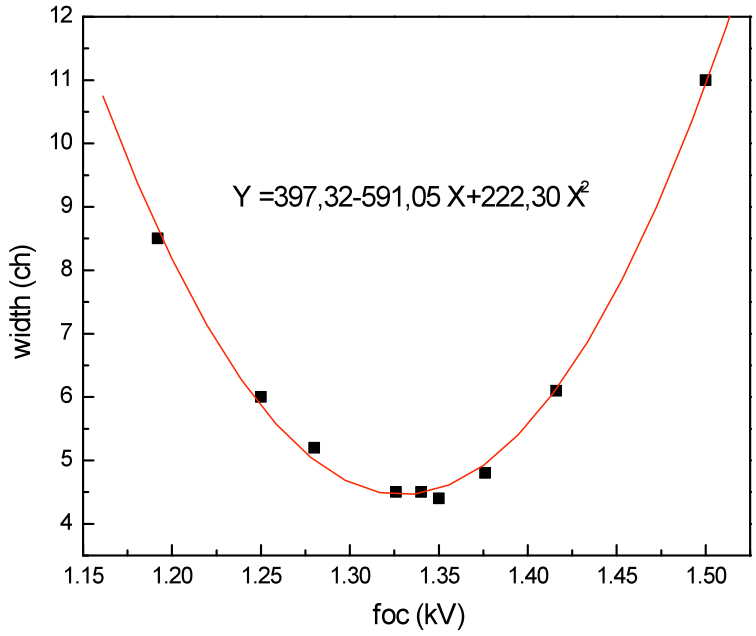

Figure 26. The width of the direct primary beam peak as a function of the lens condition at the entrance of the target chamber, square dot for the experimental data, and red line for fitted curve.

When we use the control and acquisition program to scan step by step the potential voltages of the analyzer sectors V_+ and V_-, the analyzer voltage is related to the kinetic energy of scattered projectiles by the Equ 11. By differentiating Equ 11, we can obtain the kinetic energy scanning step:

$$\delta E_k = \frac{q'(\delta V)}{2} \Big/ \ln\left(\frac{R_{out}}{R_{in}}\right)$$

Equ 12

In order to increase the precision of each step as much as possible, a voltage divider with a factor α of 12.5 or 20.8 was introduced between the power supply and the analyzer sectors. To analyze the kinetic energy loss of anions at 3keV, the negative voltage provided by the power supply of absolute value U_- was kept constant. The power supply of the positive voltage U_+ was controlled by the program with a variation δU_+ of 1.59V/step=6.5 kV/4096 (12 bits). The

vertical scale of the spectrum corresponds therefore to 1.59V/channel for U_+. The voltage U_- was divided by a volt box with a factor of α_1=12.5, i.e., $V_- = -U_-/\alpha_1$. The voltage U_+ was divided by a volt box with a factor of α_2 =20.8. The positive voltage applied to the analyzer is therefore given by, $V_+=U_+/\alpha_2$. So we can get the kinetic energy variation for each scanning step (i.e. per channel) using the Equ 12 and applying the condition $V=V_+ - V_-= U_+/\alpha_2 + U_-/\alpha_1$:

$$\delta E_k = \frac{E_0}{(U_-/\alpha_1)+(U_+/\alpha_2)} \times \frac{\delta U_+}{\alpha_2}$$

Equ 13

In the experiment, for a beam of 3keV the initial values for U_- and U_+ are 1830V and 3175V respectively. Thus we know from the Equ 13 that each scanning step δU_+=1.59 V on the analyzer voltage corresponds to a kinetic energy variation of 0.76eV. Therefore, the kinetic energy scanning step in this case is δE_k=0.76eV/channel.

II.3.2. PR-IR spectrum

In Figure 27, a typical two-dimensional spectrum (PR-IR spectrum) was built by plotting the recoil-ion TOF along the horizontal axis and the scanning voltage of the analyzer along the vertical axis obtained in collisions between F^+ and FeTPPCl at 3keV.

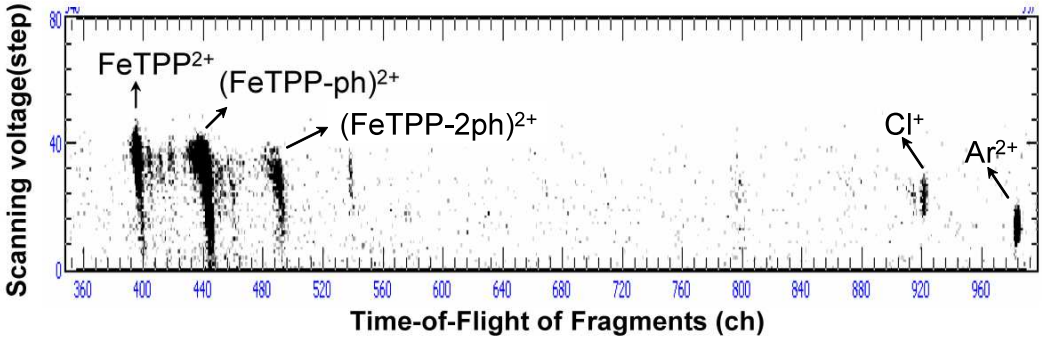

Figure 27. A typical PR-IR spectrum obtained in collisions between F^+ and FeTPPCl at 3keV.

According to Equ 11, the scanning voltage of the analyzer is proportional to the kinetic energy of the analyzed scattered projectile, here the anion F^-. If we were able to calibrate the scanning voltage of the analyzer to the kinetic energy of scattered projectile, and furthermore,

to the kinetic energy loss (ΔE) and then the excitation energy (E*) of the target according the principle of the CIDEC method, we would have converted the vertical scale of the two dimensional spectrum to the excitation energy of the target. By selecting a spot on the 2D spectrum and projecting it to the vertical axis, the internal energy distribution of the transient charged precursor M^{r+}* leading to the corresponding fragmentation process could have been experimentally determined. However, an absolute calibration of the energy axis is not immediately evident. It is due to the uncertainty and the dispersion of the potential voltage of individual collision events in the interaction region. In fact, the potential of the center of the interaction region is set to -100V. This value is not precisely known. This may introduce slight modification on the kinetic energy of the scattered beam. So, in our experiments, we employ a relative calibration method through simple etalon gas targets. This will be discussed in the forthcoming subsection. It is also noteworthy that due to the extraction field and the size of the beam (200μm), additional energy dispersion for ions under charge exchange is introduced.

II.3.3. Calibration and Deconvolution

II.3.3.1. Relative energy loss calibration

As the absolute kinetic energy calibration of the electrostatic analyzer is difficult, a relative energy loss calibration method has been used in our experiment. Spectra obtained in collisions between F^+ ions and (Ar, Xe) atoms or small molecules (H_2, N_2, H_2O …) have been studied precisely. We present here an example of calibration using the Argon atoms. We recorded a spectrum of a mixture of Argon gas and the target molecule, for instance, in the case of F^+ on FeTPPCl collisions at 3keV (Figure 27). In the double capture reaction $F^+ + Ar \rightarrow F^- + Ar^{2+}$, the ground state of the incident projectile ($1s^2\ 2s^2\ 3p^4$) F^+ is a triplet (^3P) and that of the scattered anion F^- is a singlet. To follow the conservation rule of the total spin of electrons, the target Ar^{2+} ions should populate dominantly the triplet ground state ^3P (43.4 eV) [82]. Considering the energy conservation in the reaction, as shown in Figure 28, the kinetic energy loss of F^- corresponding to the peak Ar^{2+}, $\Delta E(_{Ar}{}^{2+})$, was determined precisely to be $\Delta E(_{Ar}{}^{2+})$ $=43.4\text{-}IP_1(F)\text{-}EA(F) = 22.6$ eV. The peak obtained with the vertical projection of the spot

corresponding to the TOF of Ar^{2+} was measured to be centered at $Y(Ar^{2+})$=13.9 ch. It was employed for kinetic energy loss calibration.

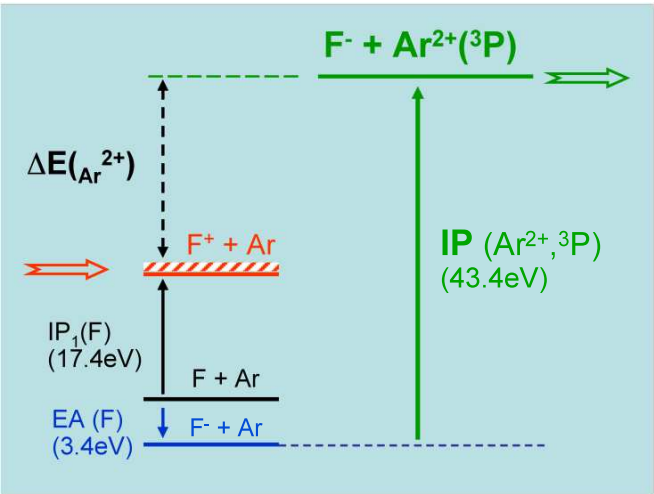

Figure 28. Energy diagram used for relative energy loss calibration.

Thus, to evaluate the kinetic energy loss of the anions F^- detected at an analyzer voltage U_+ located at the channel Y on the spectrum (Figure 27), we can use the following relation:

$$\Delta E(Y) = \Delta E(_{Ar}{}^{2+}) + \delta E_k \times (Y(_{Ar}{}^{2+})-Y)$$

Equ 14

In the present case, $\Delta E(_{Ar}{}^{2+})$=22.6eV, δE_k =0.76eV/channel, $Y(_{Ar}{}^{2+})$=13.9ch, then the Equ 14 becomes:

$$\Delta E(Y) = 22.6 + 0.76 \times (13.9 - Y) \ (eV)$$

Equ 15

Equ 15 is therefore the relation for the kinetic energy loss calibration using F^+ at 3 keV under the same experimental conditions.

Using proton projectile beam, for the calibration collision system, $H^+ + Ar \rightarrow H^- + Ar^{2+}$, the ground states of both the incident projectile H^+ and the scattered anion H^- are singlet. The conservation of the total spin of electrons in the interaction implies the population of the target Ar^{2+} ions dominantly to the singlet state ^1D (45.1 eV) [82]. The kinetic energy loss of H^- is therefore expected to be $\Delta E(_{Ar}{}^{2+})$ =45.1-IP_1(H)-EA(H) = 30.7 eV, with IP_1(H)=13.6eV and EA(H)=0.75eV.

II.3.3.2. Deconvolution

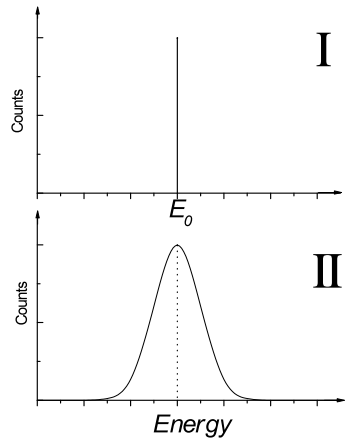

Figure 29. Illustration of instrumental enlargement for certain energy E_0 distribution: energy distribution (I), and measured energy distribution (II).

In experiments, a spectrum line centered at a certain energy E_0 will be broadened after measurement due to the instrumental enlargement. Figure 29 illustrates a special case where the width of the original line is negligible. In order to obtain the true spectral line (I in Figure 29) from the measured distribution *M(E)* (II in Figure 29), we need to remove the instrumental broadening, therefore to deconvolute the measured energy loss distribution spectra. If we use the function *g(E)* to represent the instrumental enlargement, *f(E)* the original physical distribution, the measured distribution corresponds to $M(E)=(f \cdot g)(E)$. This function is the convolution of the function f by g obtained mathematically using the relation as follows:

$$(f \cdot g)(E) = \int_{-\infty}^{+\infty} f(E_0) g(E - E_0) dE_0$$

Equ 16

In the present case, the incident ion beam energy dispersion contributes also to the enlargement of the measured distribution. In practical, the energy loss spectrum corresponding to the TOF of Ar^{2+} has been normalized and used as the reference enlargement function, i.e. *g(E)*, which includes both the instrumental enlargement and the incident ion beam energy dispersion effect. We deconvolute the measured distribution *M(E)* by *g(E)* to find the physical spectrum line distribution *f(E)*.

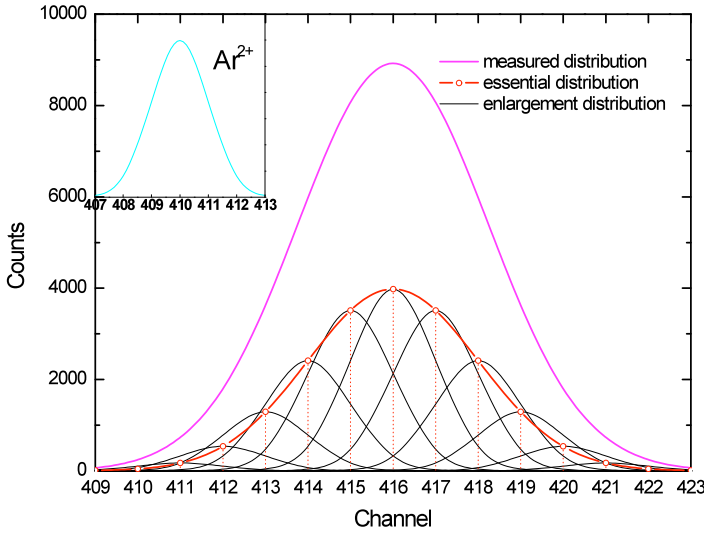

Figure 30. Illustration of deconvolution.

The deconvolution procedure is as follows:

1. We first propose a Gaussian distribution $f_0(E)$ with arbitrarily defined center, width, and amplitude.
2. Next, the energy axis is discretized to E_1, E_2…. as shown in the Figure 30.
3. Centered at each discrete energy value, E_i, a Gaussian distribution $g(E-E_i)$ of amplitude $f_0(E_i)$ was generated, $f_0(E_i)g(E-E_i)$.
4. All these Gaussian distributions were summarized leading to a function $C_0(E)$ that corresponds to the discrete convolution of f_0 by g :

$$C_0(E) = \sum_i f_0(E_i) g(E - E_i)$$

Equ 17

5. This generated function $C_0(E)$ was then compared with the experimental data $M(E)$. The discrepancy between $C_0(E)$ and $M(E)$ is characterized by the value S obtained by the summation of the square of $(C_0(E) - M(E))$ over the whole energy range.
6. The value S was minimized by using the solver function of excel where the center, the width, and the amplitude of the initial function $f_0(E)$ were defined as adjustable parameters.
7. The Gaussian distribution obtained with the adjusted parameters corresponding to the minimized S value was denoted by $f(E)$. The discrete convolution of the function f(E) by g has a minimum discrepancy comparing with the experimental data. This

function *f(E)* was therefore the best approach of the physical distribution without the contribution of the instrumental enlargement and the energy dispersion of the beam.

II.3.4. Application

The first application of the CIDEC method was on the direct measurement of the internal energy distribution of the excited doubly charged fullerene ions C_{60}^{2+}* produced in collisions with a H^+ ion beam at 2 keV [41]. A map of internal energy of the fullerene parent ions was built and the successive evaporation of one, two and three C_2 units was investigated. Experimental distribution of the excitation energy of the transient C_{60}^{2+} parent ions was obtained for each individual fragmentation channel. The measured distributions were reproduced with a cascade model. The probability for the emission of a C_2 fragment from a precursory fullerene was calculated using a statistical evaporation model without any assumption on the internal energy of the parent C_{60}^{2+} ions. Within this model, only the dissociation energies for the emission of a C_2 unit from C_{60}^{2+}, C_{58}^{2+}, and C_{56}^{2+} were adjusted parameters and were found in relatively good agreement with the theoretical values.

To apply this novel method for measuring the excitation energy of a complex system, a necessary condition is that the negative ion production rate be high enough for performing coincidence measurement. In the case of C_{60}, negative ion production rate of 10% has been measured in $F^+ + C_{60}$ collisions [83].

II.4. *Direct measurement of the neutral and negative production yield in a collision*

Is it possible to extend the CIDEC method to other molecules such as small molecules of biological importance? In fact, for molecular targets smaller than the fullerene C_{60}, if the negative ion production rate were too low, as in the case of atomic target (0.1%), it would be difficult to apply the CIDEC method; the recoil ion detection rate would be too large compared to the anion detection rate, leading to a large number of random coincidence events.

To analyze the final charge state of scattered projectiles, cylindrical electrostatic analyzers are often employed [81]. Such a device can provide high-resolution measurement in kinetic energy analysis of the ions; however it prevents one from measuring the neutralized particles

under identical experimental conditions. In a previous work in Lyon, a multicoincidence technique [83] has been employed to determine the negative ion production yield using the C_{60} target. However, this method is only suitable for targets that could remain intact (non-fragmented) after the collision. It is difficult to be applied to more fragile targets such as molecules of DNA bases, which may undergo multifragmentation in general after a primary negative ion production channel. The development of an alternative method is therefore necessary.

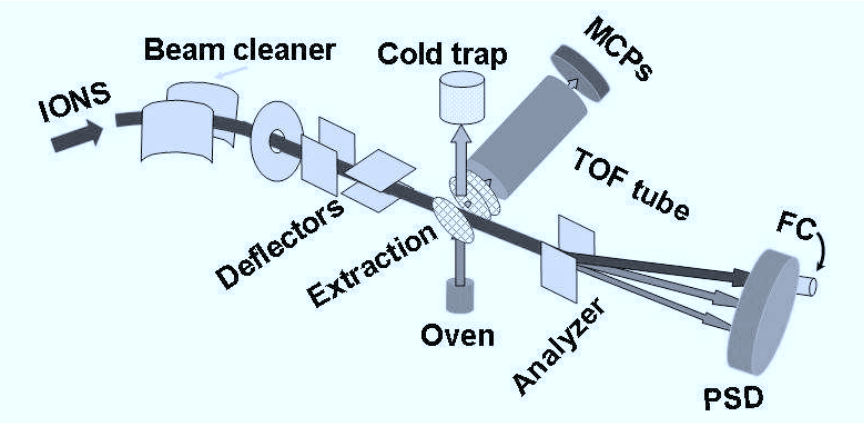

Figure 31. Schematic view of the experimental setup

In this section, we present the experimental setup developed in Lanzhou for measuring directly the production yield of all scattered projectiles, including positive, neutral, and negative scattered projectiles emerged in F^{2+} on Adenine collision. The key elements for this equipment are the parallel-plate deflector (Analyzer) for scattered projectile charge state analysis and the Position Sensitive Detector (PSD) for scattered projectile detection. The detail of the setup is described in the following.

A schematic view of the experimental setup is shown in Figure 31. The projectile ions F^{2+} at 30 keV were delivered by the ECR ion source of the Institute of Modern Physics in Lanzhou. The ions, selected in mass over charge, entered in the experimental line after a 45° magnet. The beam was then collimated by two sets of four-jaw slits separated by a distance of 800 mm (not shown in the sketch). Before entering the collision chamber, the primary beam was selected by a 30° coaxial cylindrical electrostatic deflector. This deflector, named beam cleaner, was used to eliminate secondary beams produced by collisions of ions with residual gas during the beam transport. It has a radius of 200mm along the ion beam trajectory and an exit slit of width 0.2 mm. In the collision chamber, the beam intersected a gas-phase adenine jet evaporated from an oven heated at 135°C. A plate cooled at the temperature of liquid nitrogen was mounted just above the collision region to collect the molecular jet. To ensure

the crossing of the fine projectile beam and the molecular jet, two sets of electrostatic plates in horizontal and vertical planes were inserted before the interaction region to drive the beam.

Downstream of the collision region, the projectile ions were deflected by a parallel-plate deflector. Scattered particles F^+, F^0 and F^- that have undergone charge exchange were detected by a two-dimensional delay-line position sensitive detector (PSD) composed of a couple of multi channel plates (MCP) of 75 mm in diameter and a homemade delay line anode [84]. These ions were discriminated by their position on the detector according to their charge state. The intense primary beam F^{2+} was collected into a Faraday Cup (FC) beside the detector.

For each collision event, the hitting time of the scattered projectile on the detector was recorded providing the time reference for the TOF spectrometer. The recoil ions were extracted by a homogeneous electrostatic field of 169V/cm perpendicular to the ion beam and target jet directions. The length of the acceleration and the free drift regions of the TOF were designed to fulfill the first-order focusing condition of Wiley-Mclaren. After passing through a TOF tube of 121 mm, the recoil ions were detected by a MCP detector. To increase the detection efficiency, the front MCP was biased to -2000V to post-accelerate the recoil ions. Considering also the extraction and acceleration regions with a total potential difference of 1.0 kV, the energy of a singly charged ion gets up to 3.0 keV when it hits the detector. The recoil ion signal was sent to a multi-stop TDC unit (LeCroy 4208), which was operated at single channel multi-hit (8) mode, for analyzing the arrival time of each ion with respect to the reference signal provided by the scattered projectile PSD detector. The experiments were performed in an event-by-event mode.

With the equipped Analyzer and PSD, the final charge state of the outgoing projectiles was determined, and all projectiles undergone charge exchange were measured under the same experimental conditions. And then the ratio of the neutral and negative ion production yield was directly determined.

II.5. *Summary*

To summarize, the ECRIS has the advantages of high beam current, stability, wide range of species, ease of operation, etc; in this work, it was employed to deliver the slow ion beams Cl^+, H^+, and F^+ at 3keV, slow ion beams F^{2+} at 30keV, and slow highly charged ion beams Kr^{8+} at 80 keV.

The setup in Lyon can be operated in two modes, i.e., the multi-coincidence measurement mode and internal energy measurement (or CIDEC measurement) mode. In the multi-coincidence measurement mode, the charge state analysis of the projectile, the time-of-flight spectroscopy of the recoil ions, and the detection of the number of ejected electrons were measured in triple coincidence and recorded event-by-event. Therefore the charge states of the precursor molecules of the recoil ions could be determined without ambiguity. The CIDEC method combines the multi-coincidence measurement and the kinetic energy analysis of the scattered projectile anions. For individual fragmentation pathway, the internal energy distributions of the parent molecular ions before their dissociation could be obtained.

Exploiting the parallel electrostatic analyzer and two-dimensional position sensitive detector, with the setup in Lanzhou we could directly measure the production yield of the neutral and negative outgoing projectiles in ion on small biomolecule collisions.

Chapter III Fragmentation of adenine under energy control

This chapter is devoted to the experimental investigations of interaction between slow ion beams and adenine targets. In the first part, we report the negative ion and neutral formation rates in F^{2+} and Ade collisions at 30keV. This experiment was performed in the Institute of Modern Physics at Lanzhou. After collisions with Ade targets, all scattered projectiles were analyzed using a position sensitive detector capable of the detection of positive, negative and neutral particles. In the second part, we study the fragmentation dynamics of the adenine molecule in Cl^+-Ade collisions at 3 keV performed with the CIDEC method in Lyon. The fragmentation of doubly charged parent ions Ade^{2+} was measured as a function of the excitation energy.

III.1. *Negative ion (F^-) production yield in F^{2+} on Ade collisions at 30keV*

III.1.1. The negative ion production yield

III.1.1.1. Motivation: comparison between atoms, small molecules, C_{60}, and surface

In collisions between slow ions (v<1 a.u.) and atoms, molecules, clusters or surfaces, the scattered negative ions can be considered as a probe for studying the target properties [85]. One of the applications of negative ion analysis has been demonstrated by the DCT (double charge transfer) spectroscopy in the measurement of the double ionization potential of small diatomic molecules [47-48, 86]. In H^+-molecule collisions, Furuhashi et al. have measured the energy loss of scattered negative H^- ions using a high-resolution kinetic energy spectrometer with a resolution up to 0.15 eV [48]. This resolution was sufficient to resolve vibrational levels of the excited molecular states. The first application of the CIDEC method in H^+-C_{60} collisions has shown that the production of negative ions provided an opportunity for measuring the energy deposited in a complex isolated target before its further dissociation [41].

The negative ion production yield depends sensitively on the properties of the target and projectile (dimension, structure, ionization potentials, etc). Using atomic or diatomic targets, this production yield has never exceeded 0.1% [86]. The largest negative ion production yield

up to 60%-90% has been observed in grazing collisions of ions on a LiF surface target, where a large number (from 20 to 70) of binary collision sequences with F^- lattice sites were implied [87-88]. For isolated targets, as in the case of fullerene C_{60}, intermediate negative-ion-production-rate has been reported with projectile ions at low initial charge states. For example, with F^{q+} (q=1, 2, 3) at v=0.18 a.u., the F^- production yields have been measured to be 7%, 3% and 1% respectively [83]. These values are much larger than in the cases of atomic targets. Such unexpected high negative ion production yields for a target with a limited size were interpreted as due to multi-electron capture to the ground state of the projectile in grazing collisions where the projectile passes in the electronic cloud of the C_{60} cage.

Compared to C_{60} and atoms or diatomic molecules, adenine is a target of intermediate size. In this case, we can expect an intermediate value for the negative ion production yield. In the study of the dissociation mechanism of such molecular targets, to measure precisely the energy deposited in the targets, the CIDEC method could be a good approach provided that the negative ion production yield is high enough to perform coincidence measurements.

III.1.1.2. Experimental methods: negative ion production yield measurement using inclusive recoil ion spectrum and direct measurement of all scattered particles

The main difficulty in the measurement of the negative ion production yield in ion-molecular target collisions is due to the fact that to obtain the total charge-exchange cross section, one has to measure the positive, negative and neutral scattered particles under the same experimental condition. In the experimental setup in Lyon, using cylindrical electrostatic analyzer to analyze the final charge state of scattered projectiles, the neutralized particles could not be analyzed under identical experimental conditions as charged particles. To get round this difficulty and to determine the negative ion production yield with C_{60} target, a multi-coincidence technique (Chapter II) has been used in a previous work [83]. This method is mainly based on the multi-coincidence detections in the collisions. In the experiment, on one hand, a total inclusive recoil ion spectrum S_{total}, i.e., without differentiation according to the final charge of the projectiles, was recorded, as shown in Figure 32a, for the case of F^+ projectile. On the other hand, the individual TOF spectrum S_{-1} (Figure 32b) was also measured in coincidence with the detection of negative ion F^- formed in the following reaction:

$$F^+ + C_{60} \rightarrow F^- + C_{60}^{2+}$$

Equ 18

If the two spectra were recorded under exactly the same conditions, the negative ion production yield would be obtained simply by the ratio between the count numbers of the two spectra. Unfortunately, in the experiment, the two spectra were recorded one after another with different beam transport parameters. To get a significant ratio, one has to normalize the two spectra. The normalization of the spectra was performed taking use of the C_{60}^{2+} peak in the inclusive spectrum. In fact, two distinct processes are involved in this peak: the true double capture leading to the negative ion F^- formation as in the Equ 18 and a second channel leading to the formation of neutral F^0 particle and one electron emission:

$$F^+ + C_{60} \rightarrow F^0 + C_{60}^{2+} + 1e^-$$

Equ 19

These two processes can be differentiated by considering the number of the ejected electrons measured in coincidence with the C_{60}^{2+} ions, corresponding to 0 and 1 electron detections respectively. In the correlated electron number-inclusive recoil ion spectrum (**Figure 33**), the spot related to the detection of 0 electron and C_{60}^{2+} ions is assigned to the negative ion F^- formation process. The count number of this spot over the total stable C_{60}^{2+} count number gives a ratio, say η. The individual spectrum S_{-1} is then multiplied by an adjusted factor α to $S_{-1}' = \alpha S_{-1}$, so that the ratio of the stable C_{60}^{2+} population in S_{-1}' over that in S_{total} is η. Finally, the negative ion production yield is obtained by the ratio between the total counts of the two spectra S_{-1}' and S_{total}.

However, this method is only suitable for targets that partially could remain intact (non-fragmented, in the above case, the stable C_{60}^{2+} ion) after the collision. It is difficult to be applied to more fragile targets such as molecules of DNA bases, which undergo multifragmentation in general after a primary negative ion production channel.

The experimental setup developed in Lanzhou allowed a direct measurement of the cross sections of scattered projectiles with all possible final charge state including neutral, positive, and negative ions. Using F^{2+} projectiles, the charge exchange processes lead to the final charge state of the scattered ions to be -1, 0 and 1. In the following, the negative ion production rate is defined as the ratio γ^-/γ_{total} between the F^- production cross section over the total charge exchange cross section. The total cross section, $\gamma_{total} = \gamma^- + \gamma^0 + \gamma^+$, includes the contributions of negative, neutral and positive scattered projectiles F^-, F^0 and F^+.

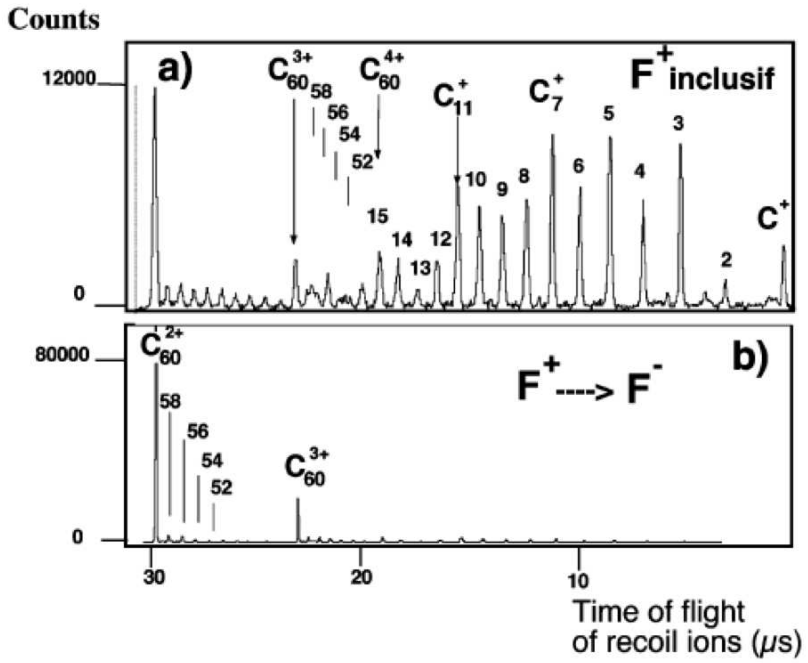

Figure 32. (a) Inclusive TOF spectrum in F^+-C_{60} collisions at 18.3 keV. The dominant single-electron capture peak C_{60}^+ was excluded. (b) TOF spectrum in coincidence with the detection of F^- [83].

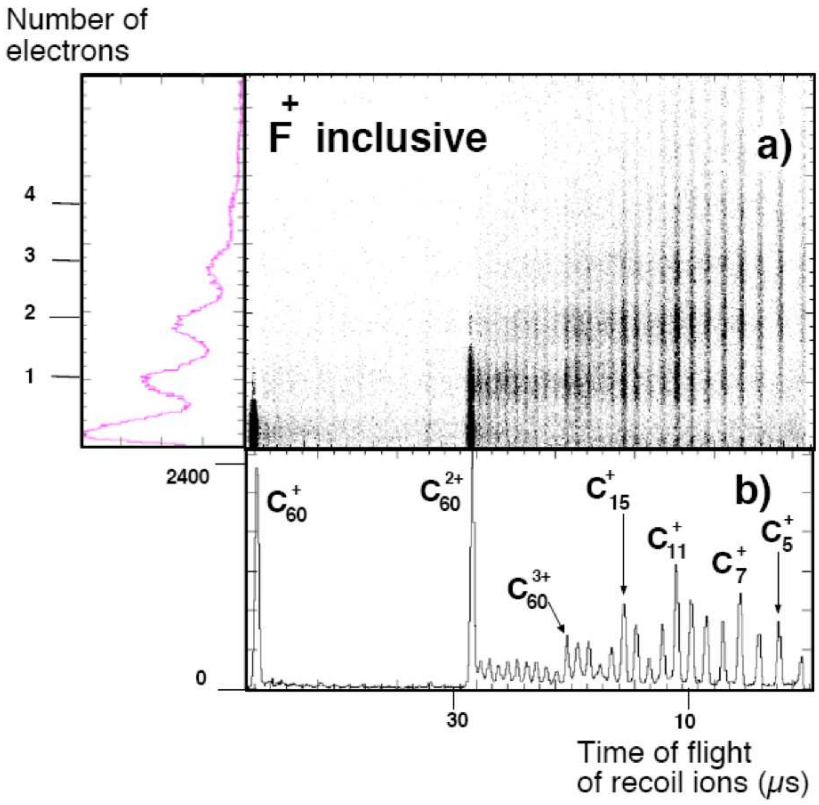

Figure 33. The correlated electron number-inclusive recoil ion spectrum.

III.1.2. Coincidence measurement in F^{2+} (30keV) –Adenine collisions

The experimental setup has been described in section II.4. In this experiment, projectiles of F^{2+} ions at 30keV were employed. The scattered positive, neutral and negative particles were separated by an electrostatic deflector and measured simultaneously by a position sensitive detector (PSD). The detection of the scattered projectiles was performed in coincidence with the Time Of Flight (TOF) spectrum of the recoil ions to exclude contributions of charge exchange in collisions with residual gas in the beam transport line.

III.1.2.1. Scattered projectile detection

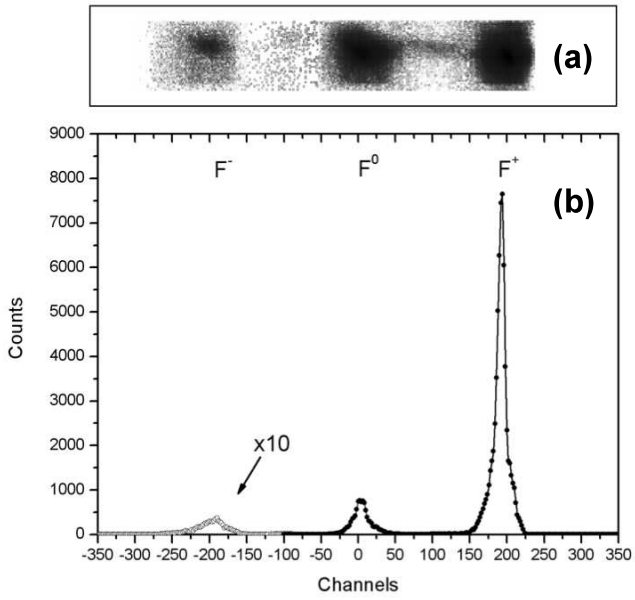

Figure 34. (a) Image of the scattered projectile particles on the position sensitive detector (PSD) measured in coincidence with the detection of at least one recoil ion with the TOF spectrometer. (b) Projection of the spectrum (a) onto the horizontal axis.

The image of the PSD recorded in coincidence with the detection of at least one recoil-ion is presented in **Figure 34**a. The spot in the centre of the detector is assigned to the neutrals F^0 that were not deflected by the parallel-plate deflector. The two lateral spots correspond respectively to the negative and positive ions F^-, F^+. **Figure 34**b presents the projection of the image onto the horizontal axis. We can find that the dominant peak is mono-charged scattered ion F^+, the neutral F^0 is about 10 times lower, and the negative ion F^- is about 10 times lower

than neutral F^0. It gives approximately a negative ion production yield of around a few percent. To extract, from the experimental data, the production yield for each species of scattered particles, it is essential to consider the detection efficiency of the MCP detector for these charged and neutral particles. The absolute detection efficiency (ADE) of MCP for neutral [89] and for ionic species [90] has been studied with light and heavy atoms in the low keV energy range using methods based on coincidence techniques. It is primarily a function of the impact energy and reaches a saturated value at a critical impact energy around 3 keV [89-90]. The comparison of the data obtained from these measurements [89-90] shows that the ADE value for neutral atomic species is similar to that of ionic ones. In the present experiment, the impact energy of the scattered particles is about 30 keV. This is much higher than the critical energy for the ADE saturation. Therefore, it is reasonable to consider that the fluorine particles F^+, F^0 and F^- were detected by the MCP with equal efficiency.

III.1.2.2. The correction of the individual recoil ion spectra in coincidence with scattered projectiles

The TOF spectra correlated to the detection of F^+, F^0 and F^- are presented in **Figure 35**a, b, and c, respectively. These spectra have been corrected by taking into account of the double collision that happened between the interaction region and the Analyzer (see Figure 31 for the setup in chapter II). The original spectrum detected in coincidence with F^0 (b)' and F^- (c)' (not shown here) has a non-negligible contribution of the Ade^+ peak. This is attributed to the double collision effect: first, in the interaction cell, a single electron capture happened between the primary projectile ion F^{2+} and an Ade target; second, the scattered projectile F^+, flying across the region between the interaction cell and the Analyzer over a distance of 265mm, may be neutralized in a collision with a residual gas molecule. The spectrum (b) is obtained by subtracting the probability for the double collision β times the spectrum (a) from the original spectrum (b)'. Similar procedure was performed for the spectrum (c).

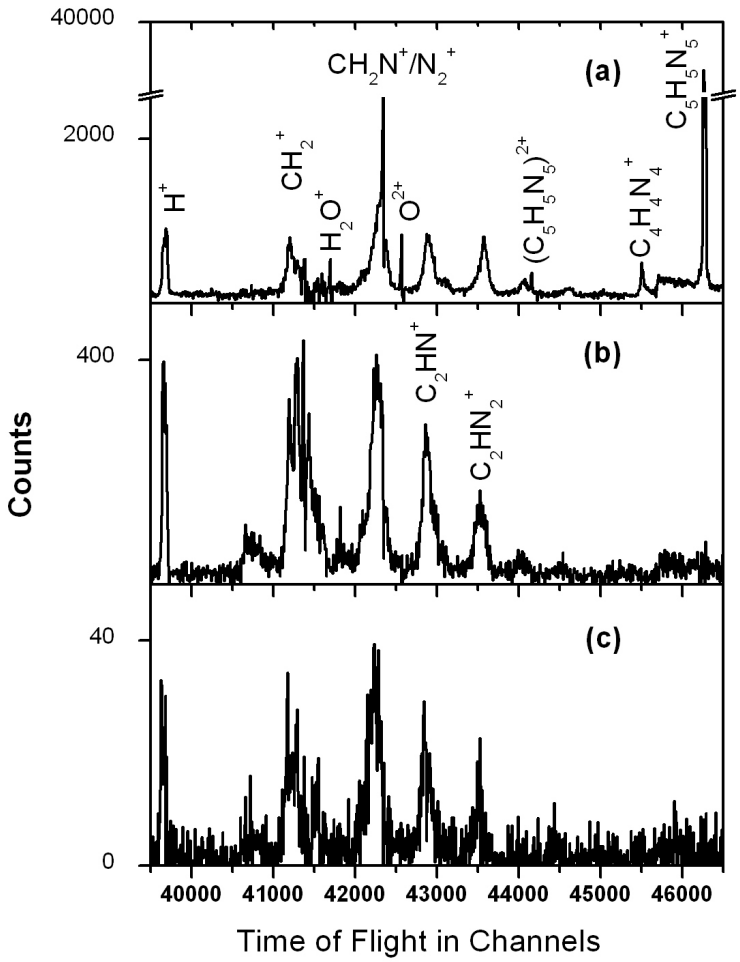

Figure 35. TOF spectrum of F^{2+}-Ade collision at 30keV. (a). With the scattered projectile selection of F^+; (b). With the scattered projectile selection of F^0; (c). With the scattered projectile selection of F^-.

III.1.2.3. The recoil spectrum in coincidence with outgoing projectile F^+

The spectrum (**Figure 35**a) recorded in coincidence with F^+ is dominated by the narrow peak at mass 135 corresponding to singly charged intact adenine (Ade^+ in the following) due to single electron capture from the molecule at large impact parameter. The small narrow peak at mass 108 corresponds to $C_4H_4N_4^+ = (Ade\text{-}HCN)^+$ resulted from the emission of a HCN unit from an Ade^+ parent ion. In the following, it is sometimes convenient to use the number "i" of heavy atoms (C and N) of a fragment $C_xN_yH_z$ (i = x+y) to label the group Gi of peaks of the mass spectrum. Therefore, Ade^+ is a peak of group G10, $C_4H_4N_4^+$ is a peak of group G8. In the present experiment, the ratio between the counts of the two peaks corresponding to HCN

emission and stable channels (N_{108}/N_{135}) is about 3%. Small fragments observed on this spectrum could be attributed either to the emission of several neutral fragments from singly charged parent ions Ade^+ or to the fragmentation of multiply charged adenine at higher internal energy. The appearance of both stable adenine and small fragments in this spectrum suggests that capture processes leading to the stabilisation of one electron on the projectile are correlated with a broad energy distribution on the target. The energy could be as low as to keep the molecule intact and as high as to induce the breaking of the molecule to several fragments.

Adenine parent molecules at higher charge state Ade^{q+} (q>=2) or their fragments could contribute to the spectrum of **Figure 35**a, as long as the final charge state of the scattered projectile is F^+. In these cases, based on the electron number conservation rule, q-1 electrons should be ejected. Therefore, the spectra related to parent ions with different charge state could have been separated by using a coincidence technique that includes the detection of the number of ejected electrons [39]. Unfortunately it was not possible to implement this technique in the present experiment. The first evidence of multicharged Ade in the TOF spectrum related to F^+ (**Figure 35**a) is provided by the observation of stable doubly charged adenine Ade^{2+} corresponding to the small but narrow peak at m/q=67.5. This coincidence detection of Ade^{2+} and F^+ projectile ions is remarkable. According to the classical over barrier model [91], stable Ade^{2+} ions are mostly produced in collisions at large impact parameter where two electrons are captured gently by the projectile, $F^{2+} + Ade \rightarrow F^0 + Ade^{2+}$. At first sight, one would rather expect to observe the peak Ade^{2+} in the spectrum of **Figure 35**b recorded in coincidence with neutral projectiles. This is obviously not the case. The appearance of the peak Ade^{2+} in the **Figure 35**a indicates that in the above charge exchange process, two electrons are transferred into doubly excited states that decay via autoionisation process, $F^{0*} \rightarrow F^+ + 1e^-$. The absence of the peak Ade^{2+} in the **Figure 35**b demonstrates that the stabilization of both excited electrons via radiative transition is highly unlikely. More theoretical efforts would be required in order to determine the electronic states that are likely to be populated on the projectile and their branching ratios concerning decay via autoionisation or radiative stabilisation.

Multicharged adenine parents that decay by multifragmentation could also contribute to the spectrum of F^+ (**Figure 35**a). In fact, a part of small fragments, from H^+ to fragments of group G4 of this spectrum, were observed in coincidence with another or several other small charged fragments (not shown here), which confirmed the charge of parent ions to be equal or larger than 2 for this population. Indeed, in a previous experiment at similar experimental

conditions (collisions of F^{2+} at 36 keV on Ade) [39], it has been observed that multicharged adenine Ade^{q+} (q>=2) produced in interaction, F^{2+} + Ade → F^{+} + Ade^{q+} + (q-1)e^{-}, decay mainly by multifragmentation.

III.1.2.4. The recoil spectra in coincidence with outgoing projectile F^0 and F^-

Figure 35 b and c were recorded respectively in coincidence with the detection of a neutral F^0 and a negative projectile ion F^-. In these spectra, peaks of small fragments are dominant and little difference can be noticed. The spectrum recorded in coincidence with F^0 (**Figure 35**b) is centred on fragments with a mass between G1 and G2, while the spectrum **Figure 35**c is centred between G2 and G3 with slightly larger mass. Although, this fragment population shift suggests that in collisions leading to F^0 and F^- scattered projectiles the energy deposited in the target should be slightly different, it seems difficult to get more information concerning the negative ion formation dynamics from these spectra. At this point, it is interesting to compare ion-Ade collision with collisions using other isolated target for example, a model system with a more rigid structure, the C_{60}.

In a previous experiment of the group [83], in F^{q+} + C_{60} collisions, remarkable different features have been observed in the fragmentation spectra for the channels of neutral and anion productions. Small carbon cluster fragments are observed for neutral channel while heavy fullerene fragments are dominant for anion channel. Furthermore, these two channels are discriminated clearly by very different amount of energy deposited in the target. For example, using projectiles F^{2+}, the excitation energy of the target was estimated to be around 41 eV for the F^- channel and larger than the multifragmentation limit of C_{60} (80 eV [53, 92]) for the neutrals F^0 correlated to small fragments. In the case of F^+ projectiles, the pronounced difference in the mass spectra of **Figure 32** shows clearly that a larger amount of energy is deposited in the target for the production of neutrals (F^0) than anions (F^-). From these observations, it was noticed that in collisions between ions and isolated targets the condition for negative ion production was much more critical than that for the production of neutrals. Neutral scattered projectiles, related to targets with high excitation energy and to multifragmentation of C_{60}, are assigned to violent frontal collisions where the ion passes through the C_{60} cage. The measured cross-section of F^0 correlated to the multifragmentation of the target is comparable to the geometrical section of the C_{60} cage. However, the formation of stable anion and the measured low energy deposition in the target can be only attributed to

grazing collisions where the projectiles pass through the electronic cloud of the C_{60} just outside the fullerene cage. In collisions between F^{q+} (q=1, 2, 3) and C_{60} [83], the production of F^- is attributed to direct feeding of *q+1* electrons to the ground state of the anion. The measured cross section of F^- corresponds roughly to the surface of a ring slightly beneath the electronic cloud with inner radius R_c=9.1 a.u. and a thickness of about 0.7 a.u..

In spite of the different molecular structure of adenine from C_{60}, both molecules play the role of electron donor in a collision with an incident ion. We can therefore expect some common features in the negative ion and neutral formation dynamics using these two targets. For the adenine, the first hypothesis is that stable negative ions are produced by direct multi-electron transfer to the ground state of the anions. This might be possible in grazing collisions where the ions explore regions with high electronic density. Second, in frontal collisions, when the ions pass closer to the atoms of the molecule, only neutral projectiles could probably survive. This is mainly due to the fact that in the case of anion, the loosely bound electron could be easily lost in a frontal collision. This leads to the production of a neutral. Comparing to C_{60} with a spherical shell structure, the adenine is nearly planar. In a frontal collision, the ion passes through one atomic layer instead of two as in the case of C_{60}. In a solid target, the energy deposited during a collision is proportional to the thickness. Considering molecules and clusters as solid targets of nanometer scale, the energy deposition should be reduced roughly by a factor of two for Ade comparing to targets with a shell structure. Then, the difference in excitation energy for frontal and grazing collisions is expected to be less pronounced in the case of Ade comparing to C_{60}. It is therefore not surprising to find only a slight population shift in the fragmentation spectra recorded in coincidence with F^0 and F^- (**Figure 35**b,c). Furthermore, the adenine is a more fragile molecule. Even in grazing collisions, the energy deposited in the target is already large enough for triggering multifragmentation of the molecule.

III.1.3. Negative ion production yield in F^{2+} (keV) – Adenine collisions

The above analysis of the TOF spectra ensured that the measured scattered projectiles (**Figure 34**) were produced in the interaction region by collisions with target adenine molecules and allowed for the correction of the measured populations from double collision effect. The production yield of the scattered projectiles at each final charge state was then obtained directly by the ratio of the corrected count of the corresponding peak in **Figure 34**b over the total count number. The negative ion production yield using F^{2+} at 30 keV colliding on adenine target was measured to be $\gamma(F^-)$ =1%. The neutral production yield was found to be 13%. These values are presented in **Table 3** comparing to the production yields of F^- and F^0

measured in collisions between F^{2+} at 7 keV with C_{60} targets, $\gamma(F^-)$ =3% [83] and $\gamma(F^0)$=45% [93].

Table 3. Measured scattered projectile yields in collisions between F^{2+} and Adenine and in collisions between F^{2+} and C_{60} target [83, 93].

Production yields	$\gamma(F^+)$	$\gamma(F^0)$	$\gamma(F^-)$
F^{2+} (30keV)- Ade	86%	13%	1%
F^{2+} (7keV)- C_{60}	51.7%	45%	3.3%

Considering random orientation of the molecule with respect to the projectile trajectory, the mean radius of adenine molecule could be estimated to be about 3 a.u. leading to smaller geometrical cross section for grazing collisions and frontal collisions in the present case than in the case of C_{60}. Due to the very close first ionization potential of the two targets, Ip(Ade)=8.7 eV, Ip(C_{60})=7 eV, the total electron-capture cross sections estimated using the classical over the barrier model are comparable, 2 10^{-14} cm^2 and 2.5 10^{-14} cm^2 for adenine and C_{60} targets respectively. Then, it is relevant to compare the ratio between the F^- production yields (0.03/0.01) measured with the two targets and the ratio between the geometrical sections of grazing collisions (approximately 9/3). The smaller size of the adenine molecule is therefore in qualitative agreement with the decrease of the measured relative cross section for negative ion formation channel.

III.2. *Fragmentation of Ade^{2+} under energy control*

The relatively high negative ion production yield produced in collisions with Adenine gives an opportunity to determine directly the internal energy of the parent ion before its fragmentation by using the CIDEC method (chapter II). In the experiments, the setup of Lyon was operated in energy loss measurement mode, and two types of projectiles are involved, i.e., Cl^+ and F^+ ions at 3keV. Using the electrostatic cylindrical analyzer, the outgoing negative Cl^- and F^- projectile ions were charge selected, and detected by a channeltron; therefore, before its further decay, the recoil parent ions was prepared at doubly charged state Ade^{2+}. According to charge conservation law, this stands only if there is no electron ejected in the reaction. During the experiment, we were able to measure the number of the emitted electrons, and find out that the emission of electrons to continuum is negligible in these collisions. With

a time reference from the signal of channeltron of the outgoing projectiles, parent ions or other fragments produced in the further decay of parent ions were measured by a time-of-flight spectrometer.

III.2.1. The choice of the projectile

In DCT collisions, there is an energy window that represents the possible energy deposition range provided by the projectile in the target. Different energy windows may open various reaction channels. Generally, this window depends on the characteristic of the collision system, such as the type of the projectile and target, and the collision velocity, etc. In other words, the energy window (or the distribution of the energy deposition) in the collision can be tuned by varying the velocity and the nature of the projectile. To study the decay channels of the parent ions after their excitation, in the first step, it is important to choose collision systems that can provide the energy window at low range, closing to the threshold of the decay of the parent ions as much as possible. In this section, we first compare the centers of the energy windows using projectiles Cl^+ and F^+ ions at 3keV produced by our ECR ion source.

From the principle of the CIDEC method (I.2) we know the energy deposited E_d in the molecule equals to the kinetic energy loss ΔE of the projectile corrected by the energy defect δ of the collision:

$$E_d = \Delta E - \delta$$

Equ 20

The energy defect of the collision can be calculated knowing the first $I_1(M)$ and second $I_2(M)$ ionization potential of the target molecule M and the first ionization potential of the projectile I_1 and its electron affinity EA:

$$\delta = I_1(M) + I_2(M) - I_1 - EA$$

Equ 21

As stated in chapter I, the knowledge of the first and second ionization potential of the target, adenine $I_1(Ade)$ and $I_2(Ade)$, respectively, is required to calculate the energy defect. However, while $I_1(Ade)$ was measured and calculated between 8.3 and 8.5 eV [94], there is no value available for $I_2(Ade)$ in the literature. In order to calculate the energy defect we calculated $I_1(Ade)$ and $I_2(Ade)$ using the ab-initio molecular quantum chemistry GAMESS-

US program [95] under the Gabedit user interface [96] with the 6-31G base and the B3LYP correlation method. The calculated values for I_1(Ade) and I_2(Ade), 8.36 eV (close to the experimental value) and 12.97 eV respectively, are used in the following. The energy defects for F^+ and Cl^+ projectiles are given in **Table 4**.

Table 4. Energy defect δ for F^+ and Cl^+ collision with adenine molecule calculated with I_1(Ade) = 8.36 eV and I2(Ade) = 12.97 eV. I_1 and EA from [97].

	F^+	Cl^+
I_1 (eV)	17.42	12.97
EA (eV)	3.40	3.61
δ (eV)	0.51	4.75

If we assume that in the process leading to the formation of the negative ion, the kinetic energy loss of the projectile is comparable for various singly charged ions at the same velocity, then the smaller the energy defect, the larger the excitation energy of the molecule. From the energy defect value presented in **Table 4** (4.75eV for Cl^+, while 0.51eV for F^+), we can expect a lower energy deposition into the target in the case of Cl^+ projectile collision.

Figure 36 is the mass spectrum of adenine dication parent Ade^{2+} for the two collision systems at 3 keV: (a) $F^+ \rightarrow F^-$ (v = 0.08 a.u.) and (b) $Cl^+ \rightarrow Cl^-$ (v = 0.06 a.u.). As in the section III.1.2.3, the number i of heavy atoms (C and N) is used to assign the group Gi of peaks of the mass spectrum. This number is reported on top of **Figure 36**. In the following, fragments will be written as $C_xN_yH_z^+$ without distinction between different isomers. For Cl^+ collision (**Figure 36**(b)), a significant peak of stable Ade^{2+} molecule was observed, while this is not the case for the F^+ projectile (**Figure 36**(a)). Another remarkable difference of the two spectra is the relative intensities of the fragment peaks. Compared to Cl^+, the mass spectrum with F^+ collision presents an obvious shift from heavy fragments to light ones. This gives strong evidence that, in the case of fluorine projectile, a larger amount of energy was deposited on the target than in the case of Cl^+, leading to higher intensities of light fragments.

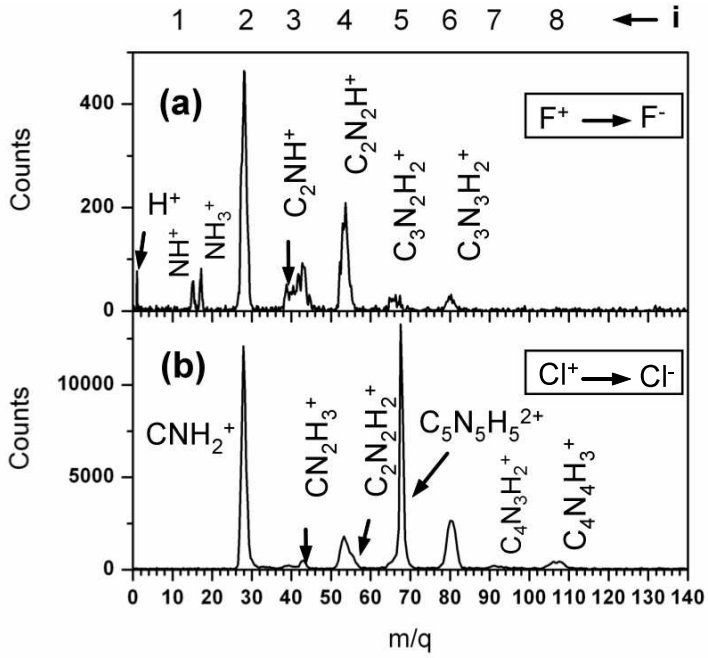

Figure 36. Fragmentation mass spectrum of Ade^{2+} parent obtained for (a) F^+ F^- and (b) Cl^+ Cl^- collision at 3 keV. The corresponding velocity of the projectile is 0.08 a.u. and 0.06 a.u. respectively. Clear excitation energy shift toward small fragments is observed for F^+ projectile.

From the discussion above, we find that, before their fragmentation, doubly charged parent ions with lower excitation energy can be prepared by using projectile Cl^+. It is a suitable case to study the first steps of the dissociation that occur in relatively low energy range. In the following, we will focus only on the fragmentation of adenine dication induced by collisions with Cl^+ projectile.

III.2.2. Excitation energy distributions of Ade^{2+} in collisions with Cl^+ at 3 keV

In collisions between Cl^+ at 3 keV and Ade, in order to get a better insight into the fragmentation of the Ade^{2+} molecule as a function of its excitation energy, a mass spectrum was recorded for different analyzer voltages around the peak of the negative ion Cl^-. The result is presented in **Figure 37**. In **Figure 37**a, the mass spectrum is plotted as a function of the analyzer voltage, leading to the map of the internal energy of the $(Ade^{2+})^*$ parent molecules. **Figure 37**b shows the mass spectrum integrated over the analyzer voltage. **Figure 37**c displays an overview of the population distributions of Ade^{2+} parent ions as a function of the excitation energy for each peak of the mass spectrum, obtained by projection onto the horizontal axis of **Figure 37**a. This axis is converted to the excitation energy based on the principle of CIDEC.

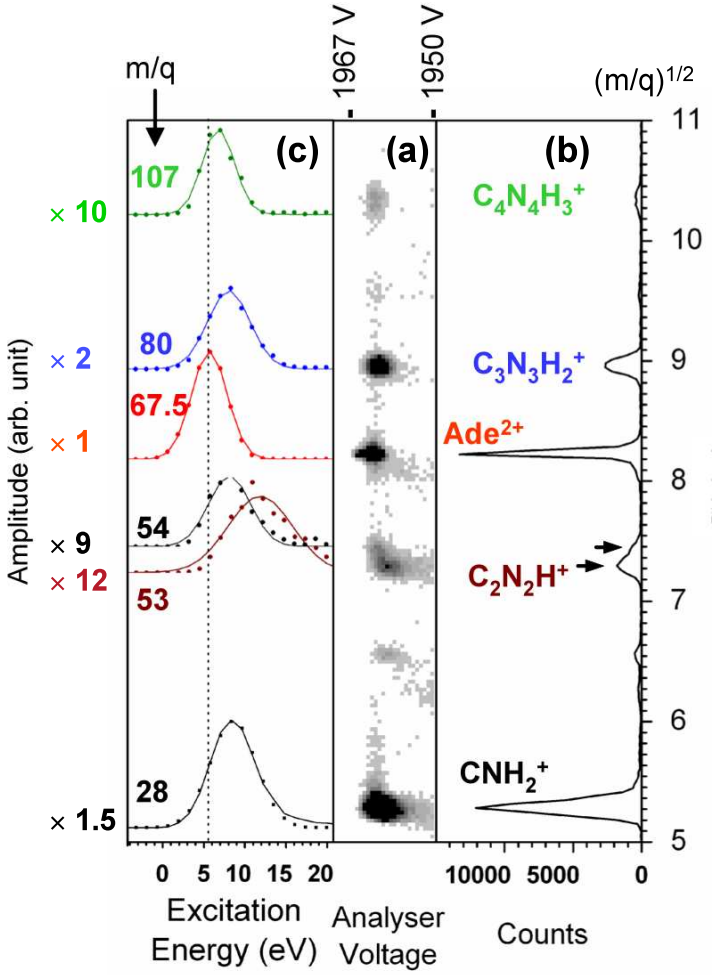

Figure 37. (a) Map of the internal energy of the Ade^{2+} parent ion: Horizontal axis, kinetic energy of Cl^- scattered ion, the point at 1967 V corresponds to the zero kinetic energy loss; vertical axis, TOF of the recoil ion. (b) Mass spectrum integrated over all the kinetic energy. (c) Population distributions of each fragment as a function of the excitation energy: Projection from (a) onto the horizontal axis for each fragment. The dash line corresponds to the center of the stable Ade^{2+} distribution.

From the population distributions as a function of the kinetic energy loss, the population distributions of Ade^{2+} parent ions as a function of the excitation energy is obtained for each fragmentation channel by taking into account of the instrumental and primary beam energy dispersion broadening (4.3 eV FWHM). The deconvoluted distributions of the population of Ade^{2+} parent ion leading to stable Ade^{2+} ion and to the fragments m = 107, 80, 54-55 and 53 are displayed in **Figure 38**. The mean value of the distributions is shown in **Figure 39** and **Table 5**. Stable doubly charged adenine can be formed with mean excitation energy of about 6 eV corresponding to an average projectile energy loss $\langle \Delta E \rangle$ = 10.8 eV. Using a simple model of

attractive Coulomb potential curves for the collision, an average impact parameter $R_c = |Q_P| Q_T / \langle \Delta E \rangle$ can be calculated where $Q_P = -1$ and $Q_T = 2$ are the charge of the projectile and the adenine in the exit channel, respectively. This is remarkable that the value $R_c = 5$ a.u. obtained with this simple model is close to the average size (about 6 a.u.) of the adenine molecule in accordance to the grazing interaction involved in the formation of Cl^- anion.

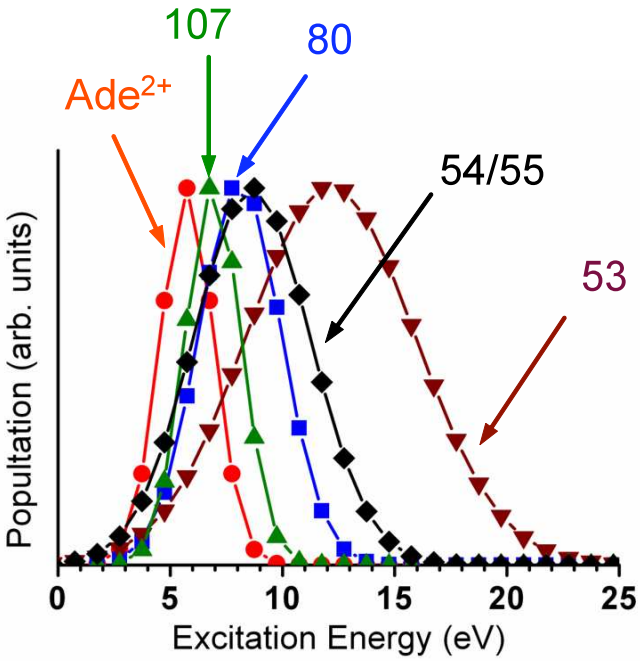

Figure 38. Population distributions (in arbitrary unit) of Ade^{2+} parent ion as a function of the excitation energy for stable Ade^{2+} ion (dot) and fragmentation channels leading to the fragment m/q = 107 (upward triangle), 80 (square), 54-55 (diamond) and 53 (downward triangle).

Table 5. Mean excitation energy of the Ade^{2+} parent and FWHM of the population distribution for the decay channels involving a charged fragment of a given m/q value.

m/q	element	Mean excitation energy (eV)	FWHM (eV)
67.5	$C_5N_5H_5^{2+}$	5.8	3.0
107	$C_4N_4H_3^+$	6.7	3.0
80	$C_3N_3H_2^+$	7.9	4.7
54-55	$C_2N_2H_2^+/C_2N_2H_3^+$	8.4	6.0
53	$C_2N_2H^+$	11.9	8.9

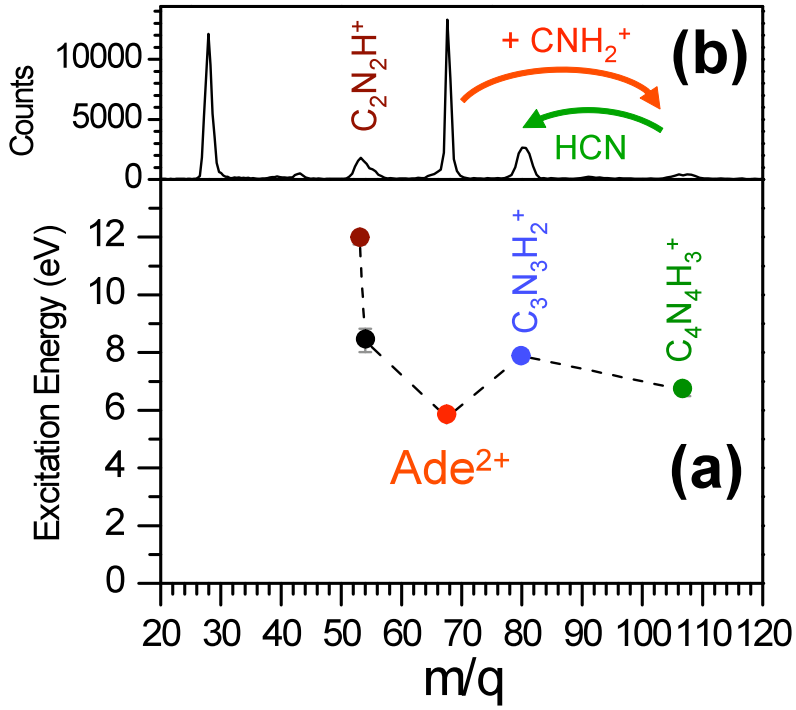

Figure 39. (a) Mean excitation energy of the relative population distributions as a function of m/q. The dash line is to guide the eyes. (b) Fragmentation mass spectrum of Ade^{2+} parent ion.

III.2.3. Discussion

The fragmentation of doubly charged adenine presents some similarities with the dissociation scheme of singly charged adenine that occurs mostly by successive evaporation of neutral HCN group. The main difference appears in the first step of the fragmentation process with the emission of a charged fragment $HCNH^+$ instead of a neutral HCN group. As a consequence the intermediate parent for the second step is not exactly the same: $(Ade\text{-}H_2CN)^+ = C_4N_4H_3^+$ (m = 107) and $(Ade\text{-}HCN)^+ = C_4N_4H_4^+$ (m = 108) for Ade^{2+} and Ade^+ respectively. The decay of these two intermediate parent ions is quite similar thus, the difference for the mass of the fragments between the mass spectra of singly and doubly charged adenine is a shift by one proton. Dissociation of singly charged adenine involving emission of neutral H_2CN fragment followed by successive emission of neutral HCN had also been reported previously but only as a minor pathway.

Regarding the excitation energy of the Ade^{2+} parent, the first step of the fragmentation process, leading to the emission of CNH_2^+ and the formation of $C_4N_4H_3^+$ (m = 107) fragment requires an excess of energy of about 0.7 eV on average (distribution centered at 6.7 eV)

relatively to the stable parent dication (distribution centered at 6 eV). The second step of the fragmentation with the evaporation of a neutral HCN from $C_4N_4H_3^+$ requires an additional excess of about 1.2 eV to form $C_3N_3H_2^+$ ion (m = 80, distribution centered at 7.9 eV). As the second step in the main fragmentation pathway of singly and doubly charged adenine proceeds through the same process of HCN evaporation, it is interesting to compare the excess of energy value we obtained with the one measured for monocharged adenine even though the fragments differ by one proton. Using synchrotron radiation in the 6-22 eV photon energy range, Jochims et al. measured the appearance energy of $C_5N_5H_5^+$ (Ade^+: m = 135), $C_4N_4H_4^+$ (m = 108), $C_3N_3H_3^+$ (m = 81) and $C_2N_2H_2^+$ (m = 54) ions to 8.20, 11.56, 12.8 and 13.7 eV respectively. These ions are formed by successive evaporation of neutral HCN from singly charged adenine parent ion. An excess of energy of 3.36 eV above the ionization potential of Ade^+ is necessary to form $C_4N_4H_4^+$ ion. In first approximation, using the data of table 2, the minimum excitation energy of the Ade^{2+} parent leading to the appearance of $C_4N_4H_3^+$ (m = 107) ion can be estimated by subtracting the width of the distribution to its mean value. The obtained value of 3.7 eV is close to the one measured by Jochims et al. [4]. This indicates that the first step of the fragmentation process is roughly triggered by the same amount of excitation energy for both the singly and doubly charged parent ion despite the different mechanism involved in the process. In the case of the dication parent, the extra charge is carried away by an extra proton attached to the emitted fragment.

From the appearance energy measurements of ref. [4], the evaporation of a second HCN from $C_4N_4H_4^+$ (m = 108) to form $C_3N_3H_3^+$ (m = 81) ion requires an excess of energy of 1.24 eV. Once again, this value is quite close to the mean excess of energy 1.2 eV (= 7.9 – 6.7) obtained for the formation of $C_3N_3H_2^+$ (m = 80) ion from $C_4N_4H_3^+$ (m = 107) in the case of doubly charged adenine. However, following the same idea, a discrepancy appears for the third step of the fragmentation process. The formation of $C_2N_2H_2^+$ (m = 54) fragment by evaporation of HCN from $C_3N_3H_3^+$ (m = 81) ion requires an excess of energy of 0.9 eV in the case of singly charged adenine parent ion. For doubly charged adenine, the population distribution of fragment $C_2N_2H^+$ (m = 53) is centered at 11.9 eV. Therefore, a rather important increase of the initial excitation energy of Ade^{2+} parent would be required to form the $C_2N_2H^+$ fragment from the $C_3N_3H_2^+$ ion (m = 80, distribution centered at 7.9 eV) as the excess of energy is about 4 eV. Assuming that the chemical structure of $C_3N_3H_2^+$ ion is similar to the cyclic triazine molecule ($C_3N_3H_3$), the evaporation of HCN would necessitate two bond ruptures hence requiring more excitation energy. The formation of $C_2N_2H^+$ (m = 53) ion may be quite complex as suggested by the width of the m = 53 energy loss distribution that is

much broader (table 2) compared to the other fragments. A population of different isomers formed at different excitation energies may be responsible of this broadening and a distinction between several m = 53 isomers may be necessary to provide better understanding of the processes involved.

From **Figure 38** and **Figure 39**, it can be seen that the m = 54-55 distribution is centered at 8.4 eV, a value close to the mean excitation energy obtained for m = 80 ions, and the former distribution is slightly broader than the later one. This suggests that the height of the potential barriers for the formation of $C_3N_3H_2^+$ (m = 80) and $C_2N_2H_2^+/C_2N_2H_3^+$ (m = 54-55) is roughly the same. As recently observed for singly charged adenine, another channel may proceed via the intermediate parent ion $C_4N_4H_3^+$ (m = 107) by evaporation of a neutral HC_2N_2/C_2N_2 (m = 53/52) fragment. Therefore a specific pathway for the formation of $C_2N_2H_2^+/C_2N_2H_3^+$ (m = 54-55) fragments needs to be considered for Ade^{2+} parent ions with the opening of competitive channels for the second step of the fragmentation process.

Alternative second steps:

$C_4N_4H_3^+$ (m = 107) → $C_2N_2H_2^+$ (m = 54) + HC_2N_2 (m = 53).

$C_4N_4H_3^+$ (m = 107) → $C_2N_2H_3^+$ (m = 55) + C_2N_2 (m = 52).

Regarding these observations a schematic view for the main fragmentation pathways of the adenine dication is proposed in **Figure 40**. For each fragment, the mean excitation energy of the Ade^{2+} parent is reported on the right scale. From the intermediate parent ion $C_4N_4H_3^+$ (m = 107), the two competitive channels leading either to fragment $C_3N_3H_2^+$ (m = 80) or $C_2N_2H_2^+/C_2N_2H_3^+$ (m = 54-55) are represented. The low-energy two-step process leading to the formation of fragment m = 54-55 opens new possibility to investigate the synthesis of adenine particularly for astrobiology.

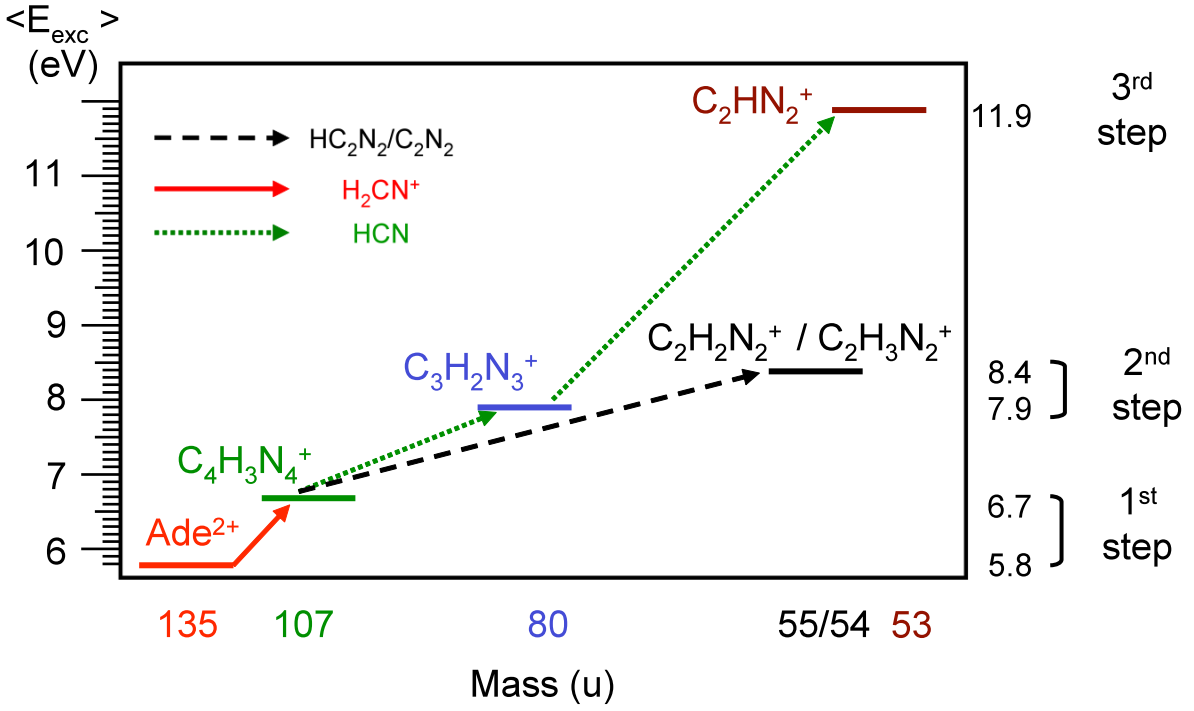

Figure 40. Schematic view for the main fragmentation pathways of Ade^{2+}. Bottom scale: m/q value of the fragment. Left scale: mean excitation energy of the doubly charged adenine parent to form fragment m/q. Right scale: mean excitation energy and number of steps to produce the m/q fragment.

III.3. *Conclusion*

In summary, the combination of the parallel-plate electrostatic analyzer and two-dimensional position sensitive detector offers an opportunity for detecting simultaneously all scattered projectiles, including positive, neutral and negative particles. In collisions between F^{2+} and Adenine at 30keV, the production yields of F^+, F^0 and F^- have been measured to be about 86%, 13%, and 1%, respectively. Despite a slight decrease compared to the C_{60} target, the measured negative ion formation cross section is still much larger than the yield in ion on atom collisions. Using singly charged projectiles, higher negative ion rate is expected,

Using the CIDEC method, the fragmentation of adenine dication was investigated as a function of the excitation energy. The parent dication was prepared in collision between Cl^+ and Ade at 3keV. It was found that the fragmentation pattern of Ade^{2+} was dominated by the successive emission of a charged fragment H_2CN^+ followed by the loss of neutral fragments HCN^0. This successive emission dynamics was confirmed by the excitation measurement of

the excitation energy distribution of the parent dications. A specific fragmentation channel requiring less energy than the usual successive emission of neutral HCN was demonstrated, i.e., the emission of a charged H_2CN^+ followed by the emission of a HC_2N_2 to get a fragment of group 4, $H_2C_2N_2^+$. The mean excitation energy of this channel was measured to be about 8.4eV. It is much lower than the energy necessary for the three-step-process (11.9 eV), the emission of a charged H_2CN^+ followed by the successive emission of two HCN neutrals to get the G4 fragment $HC_2N_2^+$.

Chapter IV The fragmentation of FeTPPCl

This chapter is devoted to the fragmentation studies of a larger target system, FeTPPCl molecule. In the introduction, the complexity and some difficulties in the experiment will be presented. In the second section, we study the fragmentation pattern of this molecule by multi-coincidence method. For that, the interaction system of slow Kr^{8+} (at 80 keV) multicharged ions colliding on FeTPPCl molecules is considered. The followed section will be focused on the internal energy measurement for fragmentation pathways of excited parent ions $FeTPPCl^{2+}$ by using the CIDEC method. The loss of H_2 from the intermediate parent ion $FeTPP^{2+}$ will be discussed in the light of the internal energy distribution.

IV.1. *Introduction*

To study the fragmentation of this large molecule, we should consider the complexity and some difficulties encountered in experiments. The first one is due to the limited mass resolution of our TOF spectrometer for heavy fragments. The molecule FeTPPCl has a formula of $C_{44}H_{28}ClFeN_4$, with various isotopes of the constituent atoms (C, Cl, Fe, and N). It results in a complex peak pattern around the mean nominal mass of 704. In this work, the isotopic structure can not be resolved. In the following, the spectra will be analyzed under two resolution conditions. In the first part, heavy fragments are assigned with a precision of ±2 units of atomic mass, so that differentiation of the loss of benzene molecule (C_6H_6) and phenyl group (C_6H_5) is not possible. For convenience, the symbol $FeTPPCl^{r+}$ will be employed to represent the parent ions; $FeTPP^{q+}$ the ions with the loss of the chlorine atom from the parent ions, and *ph* the neutral phenyl group (C_6H_5). In TOF spectra at such resolution, extra hydrogen loss or gain will not be distinguished. For instance, on a TOF spectrum, if one peak is assigned to fragment $FeTPP^{2+}$, it means that this peak is mainly around the nominal mass of 669, with a precision of ±2. In the section (IV.4), the TOF spectra are analyzed with a better precision of ±0.2 atomic mass unit. With this precision, fragments with or without extra loss

of hydrogen atoms can be assigned precisely. Considering the number of H_2 loss, the fragments will be noted as $(FeTPP\text{-}H_2)^{2+}$, or $(FeTPP\text{-}2H_2)^{2+}$, etc.

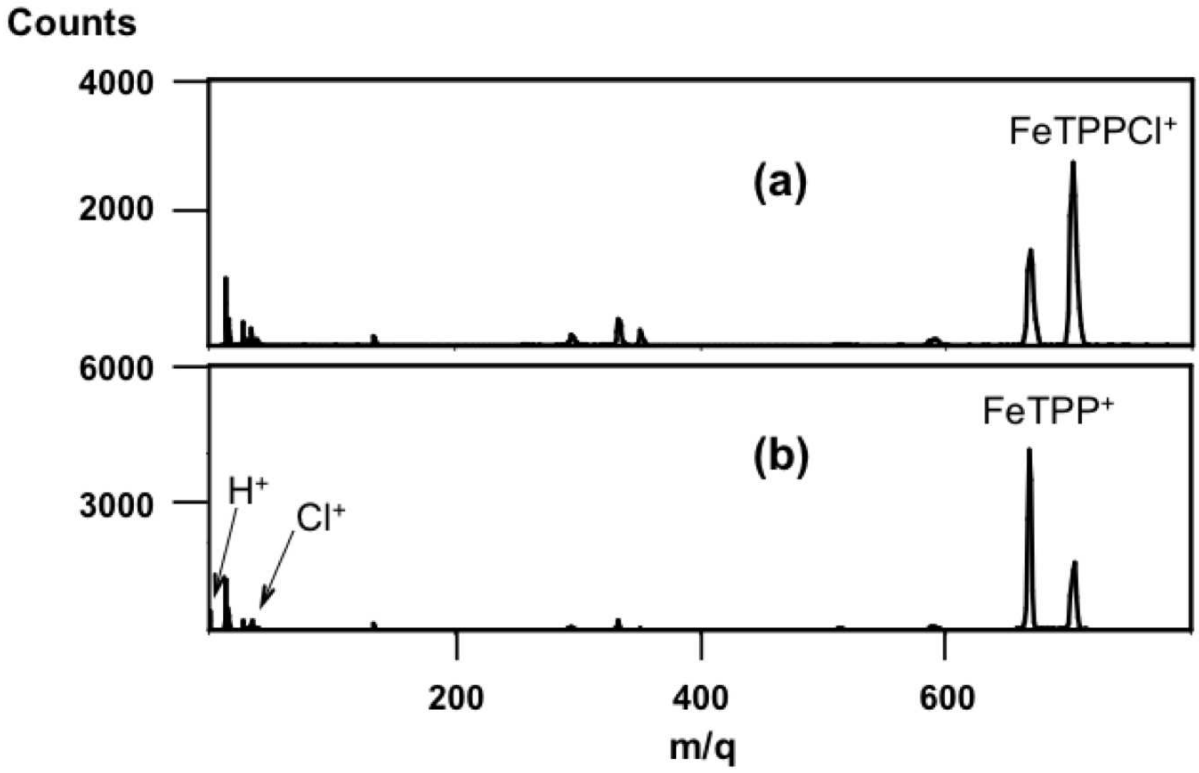

Figure 41. Evidence that there are more than one target beams evaporated from the oven: (a). TOF spectrum of 6keV F^{2+} on FeTPPCl collisions, with the oven temperature of 380°C; (b). TOF spectrum of 6keV F^{2+} on FeTPPCl collisions, with the oven temperature of 350°C

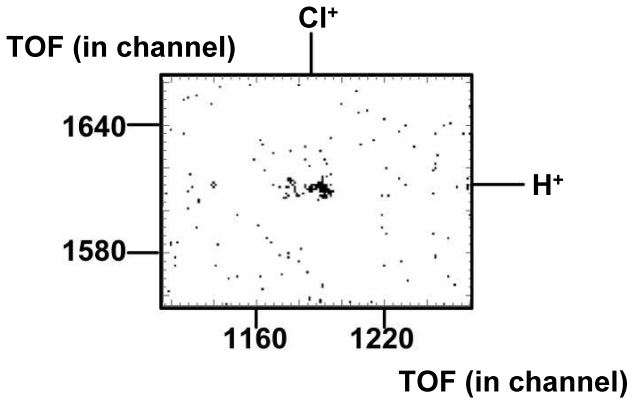

Figure 42. Coincidence between H^+-Cl^+ indicated the presence of neutral HCl in the target beam.

The other difficulty is to obtain a pure target beam evaporated from the oven. In fact, under different oven temperature conditions, the target beam might contain other molecules than the

expected FeTPPCl. This has been demonstrated by the TOF spectra (**Figure 41**) measured in 6keV F^{2+} on FeTPPCl collisions. The spectra of **Figure 41**a and **Figure 41**b were obtained under identical experimental conditions except the oven temperature: 380ºC for (a), and 350ºC for (b). A remarkable variation of the relative intensities of the two dominant peaks, corresponding respectively to the parent $FeTPPCl^+$ and $FeTPP^+$ ions on the TOF spectra, is observed with the oven temperature, showing clearly the presence of both FeTPPCl and FeTPP molecules in the target beam. The unexpected presence of FeTPP in the molecular beam is confirmed furthermore in a kinetic energy loss measurement of anion using neutral F^0 beam on FeTPPCl collisions. The peaks H^+ and Cl^+ in the spectrum **Figure 41**a are partly originated from the presence of HCl molecule in the target beam. This is demonstrated by the coincidence measurement of H^+ and Cl^+ (**Figure 42**) obtained from the 3keV F^+ + FeTPPCl collision, with the oven temperature operated at 360ºC. All these unexpected molecules, FeTPP, and HCl may originate from the chemical reaction inside the oven before the evaporation of the target molecules.

IV.2. *Fragmentation of $FeTPPCl^+$, $FeTPPCl^{2+}$, and $FeTPPCl^{3+}$ prepared in collisions with Kr^{8+} at 80keV and studied with multi-coincidence method*

IV.2.1. TOF spectrum measured in coincidence with Kr^{7+}

As described in chapter II, to study the decay pathways of multi-charged molecular ions, the experimental setup was operated in multi-coincidence mode. A Kr^{8+} projectile beam at 80keV delivered by the ECR source of ARIBE facility in Caen crossed, in the collision cell, a FeTPPCl molecular jet evaporated from an oven operated at 370 °C. The recoil ions were measured in coincidence with the detection of Kr^{7+} (s=1) outgoing projectiles and the detection of the number *n* of ejected electrons. In collisions using highly charged ions, according to the impact parameter, a certain number of electrons (r) can be transferred primarily to high lying states of the projectile and decay later on by the autoionisation of n electrons leading to the stabilization of only one electron on the projectile and the production of a multiply charged molecule $FeTPPCl^{r+}$. Under the above conditions, the charge of the target molecules can be determined by the electron number conservation rule, r=n+1.

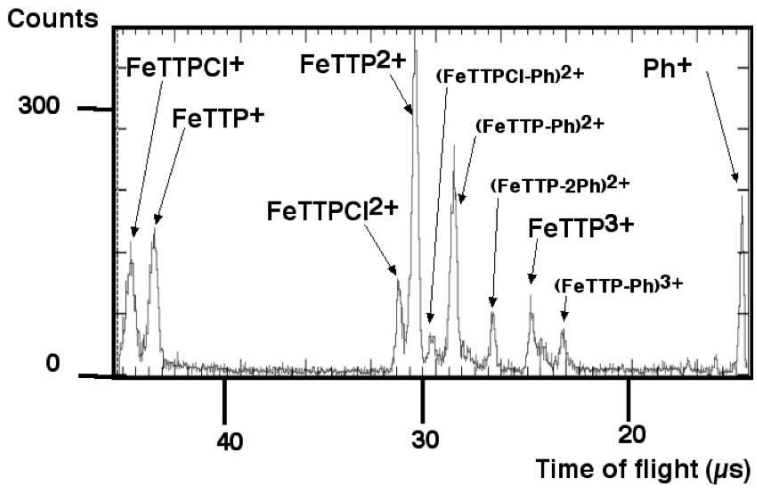

Figure 43. TOF spectrum of Kr^{8+}-FeTPPCl collision at 80keV, obtained in coincidence with the Kr^{7+} outgoing projectile (s=1).

The total time-of-flight spectrum for all fragments (without the selection of the number of emitted electrons) is presented in **Figure 43**. Intact molecules are observed for singly and doubly charged states, $FeTPPCl^{+}$ and $FeTPPCl^{2+}$. Heavy charged fragments such as $FeTPP^{q+}$, $(FeTPP\text{-}ph)^{q+}$ and $(FeTPP\text{-}2ph)^{q+}$ are also identified. Apart from the phenyl peak, no other light fragments resulting from the fragmentation of the parent FeTPPCl molecules are observed on the spectrum. The peaks corresponding to ions of smaller mass than a phenyl and resulting from collisions with the background gas are not shown on the spectrum. This observation shows that under the present experimental conditions, via long distance electron capture process, multicharged molecules with relatively low excitation energy are prepared allowing only for the emission of light neutral or charged fragment. In agreement with other experiments [22, 72-73], the dominant low energy-cost channel for the three charge states of FeTPPCl ($FeTPPCl^{+}$, $FeTPPCl^{2+}$ and $FeTPPCl^{3+}$) parent ions is the emission of the Chlorine atom leading to the intense peaks $FeTPP^{+}$, $FeTPP^{2+}$ and $FeTPP^{3+}$. The small peak around 29.5 μs on the TOF spectrum has never been observed in previous experiments. It is attributed without ambiguity to $(FeTPPCl\text{-}ph)^{2+}$.

The emission of a Benzene molecule C_6H_6 from $(FeTPP)^{+}$ fragment ions has been differentiated from the loss of a C_6H_5 fragment in electron impact experiment [22], showing that the emission of Benzene group from $FeTPP^{+}$ is predominant. The corresponding singly charged peak $(FeTPP\text{-}C_6H_6)^{+}$ is merely observable in our experiment. This indicates that in our experiment singly charged $FeTPPCl^{+}$ is prepared at low excitation energy. After the loss of the Chlorine atom, any further dissociation from fragment $FeTPP^{+}$ is not possible in our

experimental time window. This is expected in the interaction between multicharged ions and molecules where one-electron capture process occurs at long distance and the energy deposited on the target is very low.

On the other hand, doubly or triply charged FeTPPCl molecules are produced in two or three electron capture processes at shorter distance. A larger amount of energy is deposited on the parent molecular ions $FeTPPCl^{2+}$ and $FeTPPCl^{3+}$. Due to the possibility of losing both neutral or charged fragments from a multiply charged molecule, the intense peaks of lower mass fragments, $(FeTPP\text{-}ph)^{2+}$, $(FeTPP\text{-}2ph)^{2+}$ and $(FeTPP\text{-}2ph)^{3+}$ can be attributed to more than one fragmentation channels. For example, the peak $(FeTPP\text{-}ph)^{2+}$ might be either due to the evaporation of a neutral phenyl from doubly charged $FeTPP^{2+}$ or due to the asymmetrical fission of $FeTPP^{3+}$ via the loss of a monocharged ph^{+}.

IV.2.2. TOF spectra with well-defined initial charge of the parent ions

In order to measure precisely the branching ratios of different fragmentation channels related to a well-defined charge state of parent ions, we have measured the number *n* of ejected electrons in coincidence with the recoil ions. **Figure 44**a displays a two-dimensional spectrum plotting the TOF of the heaviest fragment of each event (horizontal axis) and the amplitude of the PIPS detector signal (vertical axis). From the signal of PIPS detector, we extracted information on the number of ejected electrons. **Figure 44**b, c and d show the partial projection onto the horizontal axis of **Figure 44**a with the selection of n=0, 1 and 2 for detected electrons. Based on the electron number conservation rule, r=n+s with s=1, the charge r of the parent molecules $FeTPPCl^{r+}$ related to the three fragmentation spectra is determined easily to be r=1, 2 and 3 for **Figure 44**b, c and d respectively.

For the mono-charged parent ions $FeTPPCl^{+}$ (**Figure 44**b), the main decay channel shown by the peak $FeTPP^{+}$ is due to the emission of neutral chlorine. Based on the analysis in IV.1, an unknown fraction of this peak is due to one electron capture process directly from FeTPP delivered by the oven. The small doubly charged peak, attributed to $FeTPP^{2+}$, could result from two channels. One is related to double electron transfer process $Kr^{8+} + FeTPPCl \rightarrow Kr^{6+}+FeTPPCl^{2+} \rightarrow Kr^{7+}+1e^{-}+FeTPP^{2+}+Cl$, where one of the transferred electrons is lost by the projectile via auto-ionization and missed from the detection due to the limited electron collection and detection efficiency. The other one is due to a single electron transfer process followed by the emission of chlorine anion, $Kr^{8+} + FeTPPCl \rightarrow Kr^{7+}+FeTPPCl^{+} \rightarrow$

Kr^{7+}+$FeTPP^{2+}$ + Cl^-. This last channel involving the loss of an anion Cl^- from a singly charged $FeTPPCl^+$ has been discussed in a previous work by Bernigaud et al [73].

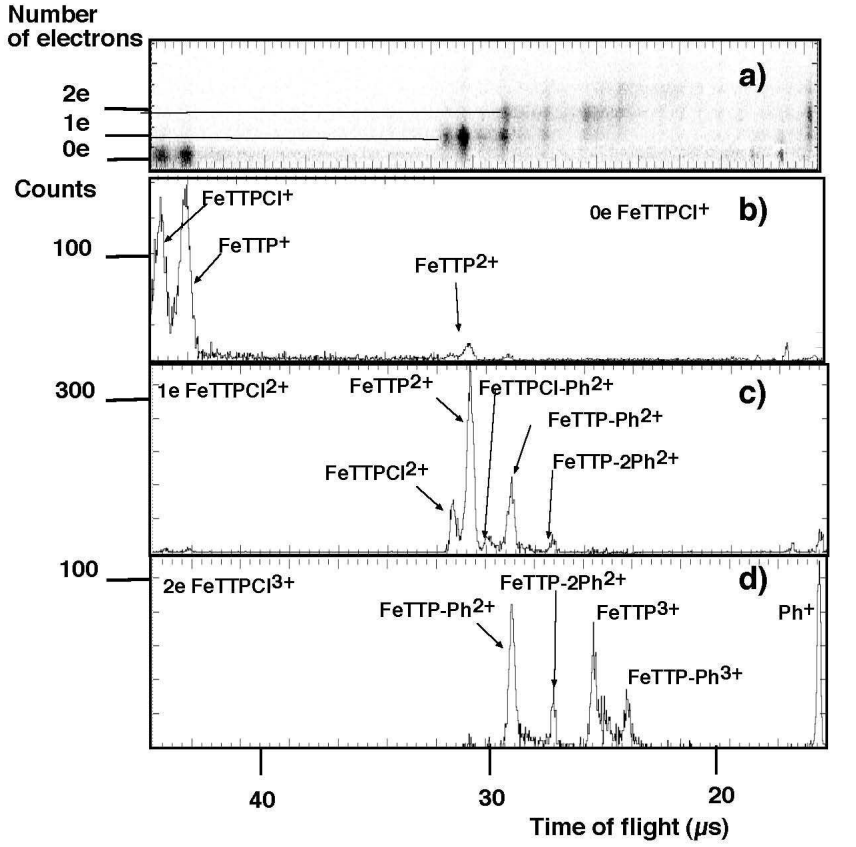

Figure 44. a) Two-dimensional spectrum: the TOF of the heaviest fragment of each event is plotted along the horizontal axis and the amplitude of the PIPS detector giving the number of detected electrons is plotted along the vertical axis. **b)** Partial TOF spectrum obtained by projection of the spectrum a) onto the horizontal axis with the selection of 0 electrons. **c)** Idem as b) but with the selection of 1 electron. **d)** Idem as b) but with the selection of 2 electrons

After corrections of the spectra of **Figure 44** taking into account of the electron collection and detection efficiency, as discussed in previous works [79, 81], the number of counts of all observed dissociation channels related to parent $FeTPPCl^{r+}$ ions with r=1, 2 and 3 are given in the **Table 6**.

For singly charged parent molecules, $FeTPPCl^+$, the branching ratio between the emission of the anion and neutral chlorine has been estimated to be very low, smaller than one percent and in the error bars. Despite the weak measured branching ratio, the phenomenon for negative ion ejection from a positively charged molecule is a plausible process. It can be explained qualitatively by the high electronegativity of the chlorine and by the particular ionic

bond between iron and chlorine compared to the other valence bonds. The mobility of charge between the bonds like C-C or C-N is very different from that on the ionic bond. On the Fe-Cl ionic bond, the negative charge distribution should be situated near the chlorine atom. These arguments are in consistence with the absence of chlorine cation in the correlated fragment spectrum, with the selection of Kr^{7+} for scattered projectile (s=1), whatever the initial charge state of parent ions (q=1-3).

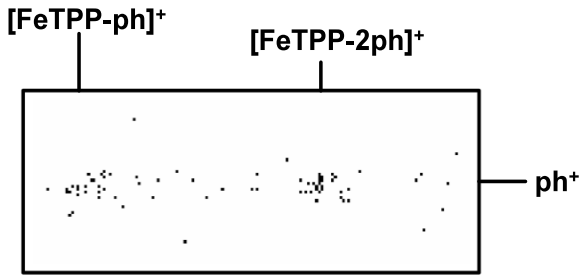

Figure 45. Coincidence spectrum between fragments observed in the dissociation of doubly charged parent ion $FeTPPCl^{2+}$ (selection of one electron) the TOF of the heaviest fragment of each event is plotted along the horizontal axis and the TOF of the lighter fragment is plotted along the vertical axis.

In **Figure 44**c, the peaks correspond mainly to the evaporation of neutral chlorine and phenyl group from $FeTPPCl^{2+}$ parent ions. The count number (**Table 6**) of the peak $FeTPP^{2+}$ (5720) is about four times larger than the peak of $FeTPPCl^{2+}$ (1420), while the count of the peak $FeTPP^{+}$ (3240) is comparable to that of $FeTPPCl^{+}$ (2750). This means that the major part of the doubly charged fragment $FeTPP^{2+}$ is due to the loss of a chlorine atom from the doubly charged parent ions $FeTPPCl^{2+}$ and only a small part may be contributed by the double electron capture directly from the FeTPP neutrals. The count numbers of other main peaks are measured to be respectively, 1960 for $(FeTPP\text{-}ph)^{2+}$, 540 for $(FeTPPCl\text{-}ph)^{2+}$, and 240 for $(FeTPP\text{-}2ph)^{2+}$. The number of counts of singly charged fragment peaks $(FeTPP\text{-}ph)^{+}$, $(FeTPP\text{-}2ph)^{+}$ resulting from the emission of a charged phenyl are so small that the two peaks can hardly get out of the noise background. However, these channels are identified without ambiguity in coincidence spectrum between charged fragments $(FeTPP\text{-}ph)^{+}$ and ph^{+} or $(FeTPP\text{-}2ph)^{+}$ and ph^{+} (as shown in **Figure 45**). The count numbers for these weak channels are found to be about 34 and 17, respectively (**Table 6**). From these measurements, the branching ratio for the emission of a charged fragment from $FeTPP^{2+}$ is estimated to be

2.0%±0.5%. The evaporation channel, measured to be 98%, is the dominant fragmentation channel for the $FeTPPCl^{2+}$.

Table 6. Number of counts for stable and fragmentation channels from $FeTPPCl^{+}$, $FeTPPCl^{2+}$ and $FeTPPCl^{3+}$ parent ions after corrections taking into account of the electron collection and detection efficiency.

Parent ions	Stable	-Cl°	$-Cl^{-}$	-Ph°	-Cl°-Ph°	-Cl°-2Ph°	$-Cl°-Ph^{+}$	$-Cl°-Ph^{+}-Ph°$
$FeTPPCl^{+}$	2750±50	3240±60	<100					
$FeTPPCl^{2+}$	1420±40	5720±80		540±20	1960±40	240±15	34±6	17±4
$FeTPPCl^{3+}$	<10	840±30			330±20		1300±40	300±20

In the **Figure 44**d, the spectrum shows peaks corresponding to the fragmentation of $FeTPPCl^{3+}$ parent ions. The peak $(FeTPPCl\text{-}ph)^{2+}$ noticed earlier in **Figure 43** is absent in **Figure 44**d. Its exclusive appearance in **Figure 44**c shows without ambiguity that the fragment $(FeTPPCl\text{-}ph)^{2+}$ is the result of the loss of a neutral phenyl from a doubly charged FeTPPCl. The loss of a charged phenyl, ph^{+}, from $FeTPPCl^{3+}$ is a negligible channel. In **Figure 44**d, intact $FeTPPCl^{3+}$ is not observed. $FeTPP^{3+}$ and $(FeTPP\text{-}ph)^{3+}$ peaks correspond respectively to the loss of Cl^{0} and the successive loss of Cl^{0} and a neutral phenyl group. $(FeTPP\text{-}ph)^{2+}$ and $(FeTPP\text{-}2ph)^{2+}$ peaks correspond respectively to the emission of a ph^{+} and a ph^{+} followed by the emission of a neutral ph^{0} from $(FeTPP)^{3+}$. These asymmetrical fission channels of $FeTPP^{3+}$ are demonstrated clearly in the coincidence spectrum between charged fragments (**Figure 46**) by the spot $(FeTPP\text{-}ph)^{2+}$ with ph^{+} and the spot $(FeTPP\text{-}2ph)^{2+}$ with ph^{+}.

From **Table 6**, the branching ratio for the asymmetrical fission of $FeTPP^{3+}$ can be estimated to 83%±4%. This high asymmetrical fission probability can be interpreted qualitatively by making an assumption within the charge distribution on the intermediate parent molecule $FeTPP^{3+}$. If we consider a good charge mobility on the molecule, the three positive charges should be distributed rather on the ring of FeTPP and more precisely on the four phenyl-groups due to the coulomb repulsion. To distribute statistically 3 charges on 4 phenyl-groups, the probability that the group of phenyl is ejected with a charge is about 75%. This rough estimation is not too far from the experimental value of 83%.

In **Figure 46**, a horizontal tail from the spot of the coincidence measurement between $(FeTPP\text{-}ph)^{2+}$ and ph^{+} towards shorter TOF is observed. It is interpreted as due to a sequential fragmentation process including, as the first step, a fast emission of a charged fragment ph^{+}

followed by a delayed emission of a neutral fragment ph^0. The fast emission of the small charged fragment ph^+ insures its detection at the nominal TOF of ph^+. In the second step, if the neutral phenyl is lost in the collision region, the residual charged fragment will be detected at its nominal TOF of $(FeTPP\text{-}2ph)^{2+}$. On the contrary, if the neutral phenyl is lost with a delay larger than several hundreds ns when the ion arrives already in the TOF tube, the charged fragment will be detected at the nominal TOF of $(FeTPP\text{-}ph)^{2+}$. In the cases where the phenyl neutral loss occurs in the extraction and acceleration fields before the TOF tube, then, the residual charged fragment will be detected at a TOF between the nominal TOF of $(FeTPP\text{-}ph)^{2+}$ and $(FeTPP\text{-}2ph)^{2+}$. This leads to the formation of the observed horizontal tail between the two spots of the **Figure 46**.

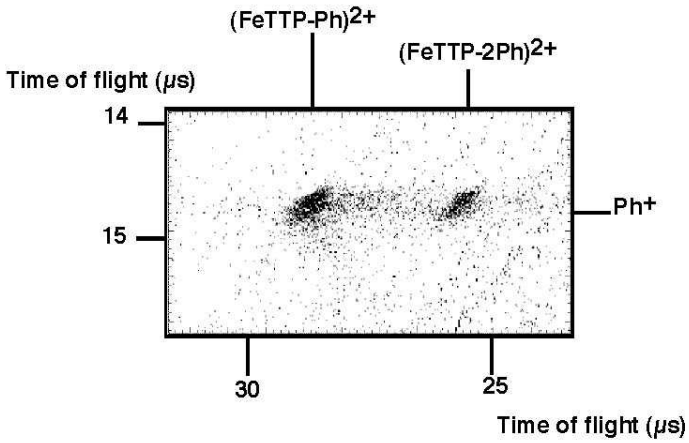

Figure 46. Coincidence spectrum between fragments emerged in the dissociation of triply charged parent ion $FeTPPCl^{3+}$: the TOF of the heaviest fragment of each event is plotted along the horizontal axis and the TOF of the lighter fragment is plotted along the vertical axis. The horizontal tail between the two spots is due to a fast emission of a charged ph^+ fragment followed by a delayed emission of a neutral ph^0.

To have a general decay pattern of the FeTPPCl molecule, the principal fragmentation pathways observed in this experiment are illustrated in **Figure 47**.

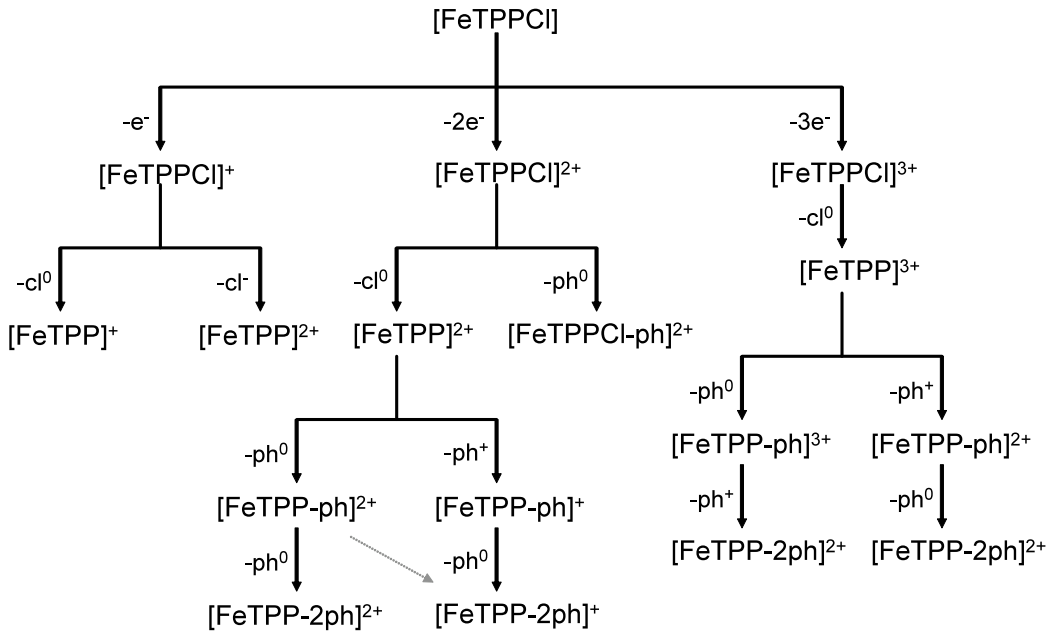

Figure 47. Dissociation channels observed for parent ions FeTPPCl $^{1+, 2+, 3+}$. The parent ions are prepared in the Kr^{8+} projectiles on FeTPPCl collisions at 80keV, leading to Kr^{7+} scattered projectiles.

IV.3. *Fragmentation of FeTPPCl^{2+} under energy control*

The excitation energy is one of the key parameters to understand the dissociation dynamics of molecules. To determine directly the internal energy of the parent ion before its fragmentation, the CIDEC method (see II.3) is employed to study the fragmentation of FeTPPCl in collision with H^+ and F^+ ions at 3keV. In these experiments, using an electrostatic cylindrical analyzer, the outgoing negative H^- and F^- projectile ions were selected, and detected by a channeltron; therefore the decay of recoil parent ions prepared primarily at doubly charged state FeTPPCl^{2+} were studied.

As presented in section I.2, in the CIDEC method, to calculate the energy defect (Equ 2) and to obtain the energy deposited in the target molecule (Equ 8), the knowledge of the first and second ionization potential of the target FeTPPCl, I_1(Po) and I_2(Po) is required. However, while from the NIST database the I_1(Po) is found to be 6.7eV, there is no value available for I_2(Po) in the literature. We have tried to calculate I_2(Po) using the ab-initio molecular quantum chemistry GAMESS-US program (similar as that of Adenine, see section III.2.1). Unfortunately, in the calculation we failed to obtain a stable dication of this molecule. To obtain a reference value of I_2(Po) and to proceed the CIDEC measurement, a rough value of 11.3 eV was proposed, which was obtained by subtracting the I_1(Po) from the appearance

energy of ion $FeTPP^{2+}$ (18eV) obtained in electron ionization and fragmentation experiment [22]. Thus, we remind here that any new value of I_2(Po) with better precision will introduce a global shift of all the excitation energy distribution spectra and the mean excitation energies concerned in section IV.3 and IV.4. The energy defects for F^+ and H^+ projectiles are given in**Table 7**.

Table 7. Energy defect δ for F^+ and H^+ collision with FeTPPCl molecule calculated with I_1(Po) = 6.7 eV and I_2(Po) = 11.3 eV. I_1 and EA from [97].

	F^+	H^+
I_1 (eV)	17.4	13.6
EA (eV)	3.4	0.8
δ (eV)	2.8	-3.6

IV.3.1. CIDEC method with F^+ projectile at 3 keV

IV.3.1.1. Kinetic energy loss of F^- in collisions between F^+ projectiles at 3 keV and FeTPPCl

For F^+ projectile, the mass spectrum measured in coincidence with the detection of the anion F^- is presented in **Figure 48**. From this spectrum, we observed no parent ions $FeTPPCl^{2+}$. The predominant fragments are heavy ions $FeTPP^{2+}$ and $(FeTPP\text{-}ph)^{2+}$. The fragments $FeTPP^{2+}$, with a count number of 5060, resulted partially from the loss of the neutral chlorine atom from the parent $FeTPPCl^{2+}$ ions and partially from collisions between F^+ and neutrals FeTPP directly escaping out of the oven. The fragments $(FeTPP\text{-}ph)^{2+}$, with a count number of 9310, were due to one neutral phenyl group evaporation from $FeTPP^{2+}$. The peak assigned to $(FeTPP\text{-}2ph)^{2+}$, with a count number of 2520, was attributed to the evaporation of two neutral phenyl groups from the fragments $FeTPP^{2+}$. Finally, with a small amount of production yield but no doubt, we measured the narrow $FeTPP^{3+}$ peak, which resulted from one electron emission of $FeTPP^{2+}$. The peak Ar^{2+} in the mass spectrum was due to the argon gas injected into the chamber at low pressure (10^{-7} mbar) for the kinetic energy loss calibration. To get the branching ratio of each decay channel, the number of counts of each fragment is presented in **Table 8**.

With the CIDEC method described previously, we scanned the kinetic energy of the outgoing projectile anion F^- by changing the voltages biased on the sectors of the electrostatic cylindrical analyzer step by step. In this way, we have measured the kinetic energy loss of the scattered projectile, and furthermore, determined the excitation energy deposited on the target molecule before its fragmentation. **Figure 49** is a two dimensional spectrum measured in coincidence between recoil fragments and outgoing F^- projectile, where the horizontal axis is the time-of-flight of the recoil fragments, and the vertical axis is the scanning voltage on the analyzer. The horizontal projection of this spectrum is just the TOF spectrum of the fragments as shown in **Figure 48.** The vertical projection of the spectrum gives a global population distribution for all outgoing anion projectiles as a function of the scanning voltage of the analyzer. This distribution is shown in the figure 11 where the analyzer voltage scanning is converted to the scale of the kinetic energy loss following the calibration method described in II.3.3. The F^- peak obtained in F^+ + Ar collision was used as the reference. It was assigned to an energy loss of 22.6 eV. The **Figure 50** represents the global kinetic energy loss distribution of the outgoing projectile anion, called *translational energy loss spectrum* [46] in early works based on Double-Charge-Transfer spectrometry. From **Figure 50**, we find that this measured distribution ranges from 0 to 30eV with a maximum centered at about 6 eV. The peak around 23 eV corresponds to the contribution of the calibration gas, i.e. the formation of Ar^{2+}. However, from this spectrum it is difficult to extract more information about the interaction and decay dynamics.

In our experiment, the coincidence measurement of the recoil fragments and the outgoing anion projectiles gives the opportunity to determine more precisely the kinetic energy loss distribution of scattered anions associated to each fragmentation pathway. In the following, the spots in the correlation spectrum (**Figure 49**) will be analyzed one by one. First, it is noteworthy that, in **Figure 49**, the spots around channels 400 and 440 on TOF axis have a special form with tilted long tails extending to lower scanning voltages and lower mass. Precise analyzes and interpretations of these features will be discussed in section IV.3.3.

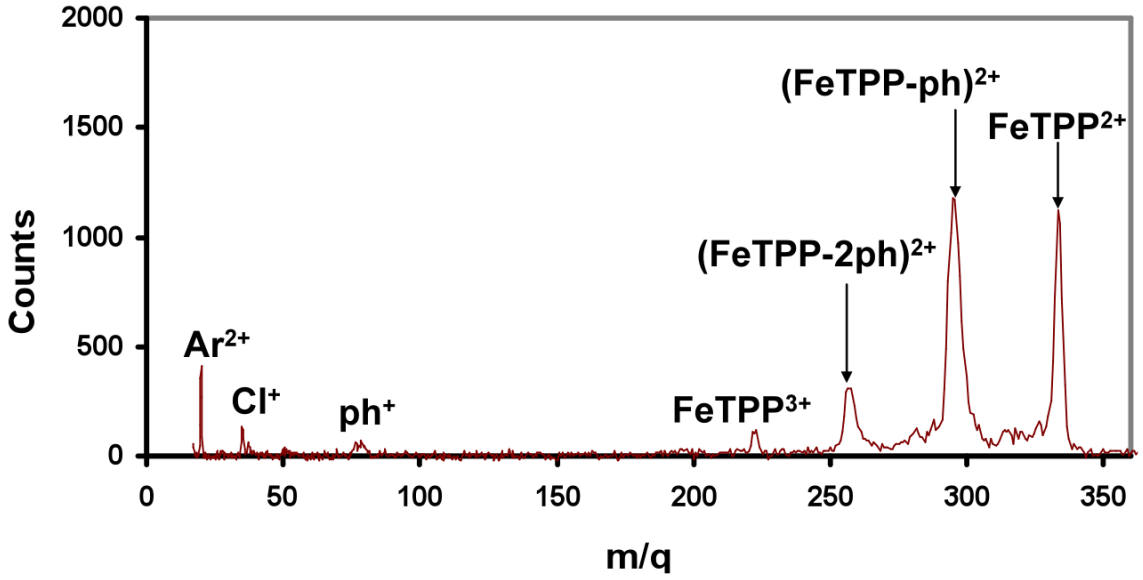

Figure 48. The mass spectrum of the fragments measured in 3keV F^+ on FeTPPCl collision. The dominant fragments have been labeled on the plot.

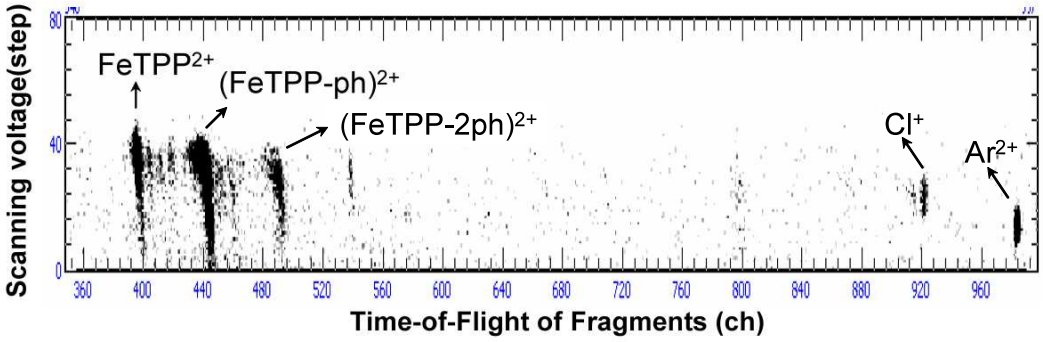

Figure 49. Correlation spectrum between recoil ions and scattered projectile measured in 3keV F^+ on FeTPPCl collision, the scattered projectile is detected with (q-2), i.e., negative F^- ions. The experiment was operated in energy measurement mode. The horizontal axis stands for the TOF of the fragment, and the vertical for the scanning voltage of the analyzer.

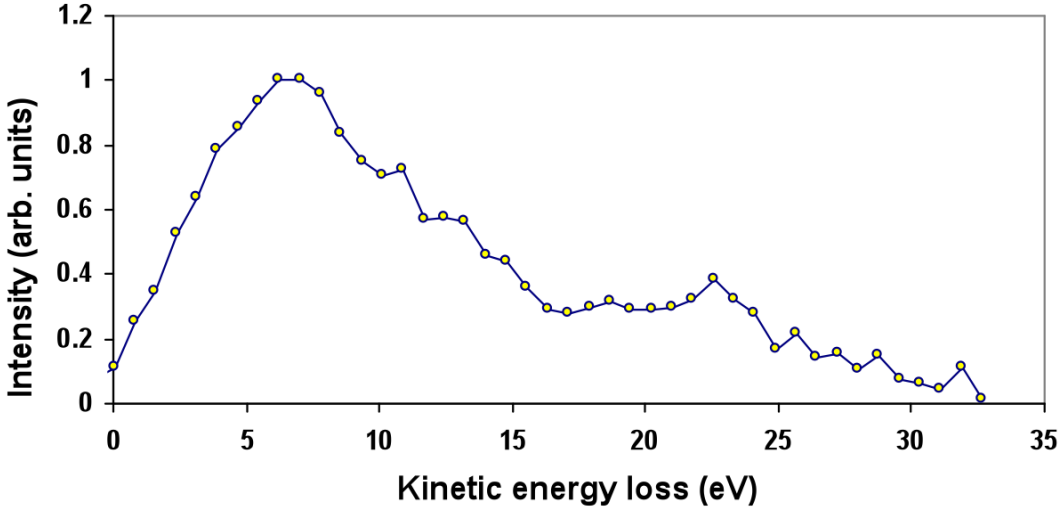

Figure 50. Global kinetic energy loss distribution of outgoing projectile F^- measured in 3keV F^+ on FeTPPCl collision experiment.

IV.3.1.2. Excitation energy distributions of parent $FeTPPCl^{2+}$ ions for individual fragmentation channels in collisions with F^+

From the vertical projection of each spot in **Figure 49**, individual population distributions as a function of the scanning voltages of the electrostatic analyzer have been obtained. Several experimental factors can lead to the broadening of these distributions, the incident projectile kinetic energy dispersion and the broadening due to the resolution of the analyzer and the dimension of the collision region. In order to extract true population distributions free from these factors, the measured distributions should be deconvoluted with a reference function that simulates contributions from all broadening factors. Usually, the F^- peak associated to the ions Ar^{2+} of the calibration gas could be used as the reference function. However, in the present work the experimental conditions were not optimized and the measured reference function was almost as broad as the F^- peak related to the main fragments. This means that the total experimental broadening is much larger than the expected measured distributions. In this condition, the deconvolution procedure becomes difficult. So, contrary to the chapter III, in this work, the raw population distributions for dominant dissociation channels are presented without deconvolution as shown in **Figure 51**. In this figure, the horizontal axis (top scale) has been converted to the scale of kinetic energy loss following the calibration procedure described above.

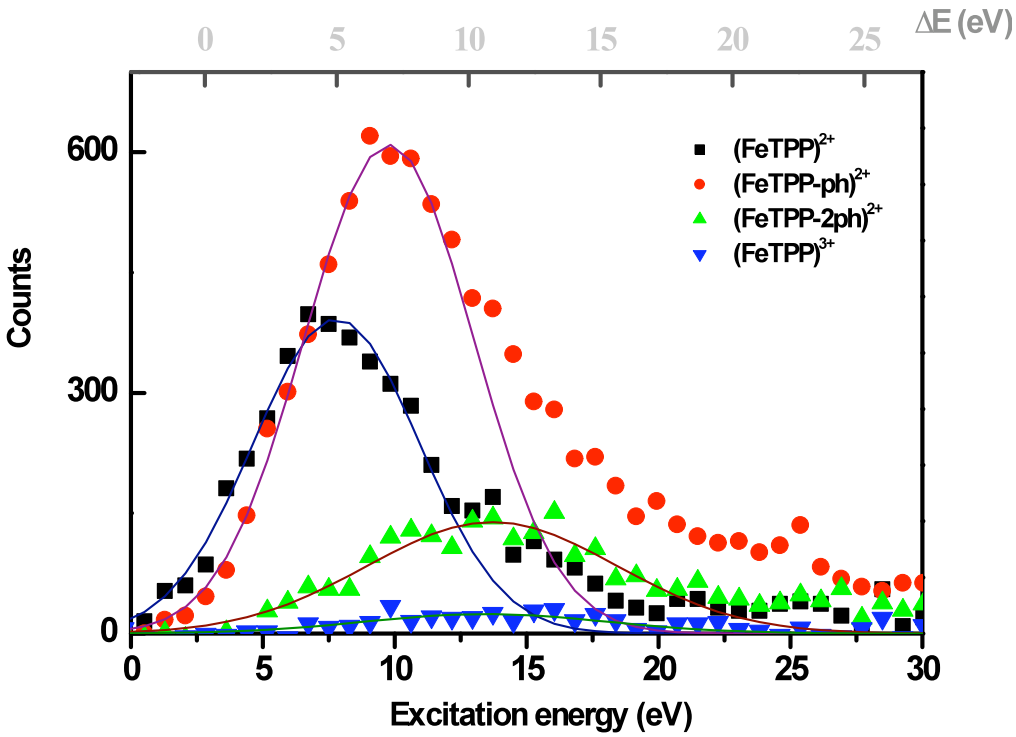

Figure 51. Population distribution for individual fragmentation pathway, measured in 3keV F^+ on FeTPPCl collision experiment. The horizontal down-scale is converted to the excitation energy of parent $FeTPPCl^{2+}$ ions. Discrete symbols stand for the experimental results, and the lines stand for the Gaussian fitting for corresponding channel. The top axis is scaled with the kinetic energy loss of outgoing F^- projectile.

According to the principle of the CIDEC method, the kinetic energy loss of the projectile is related to the excitation energy of the recoil target ion by the simple equation $E_d(M^{2+}) = \Delta E - (IP_1\ (M) + IP_2\ (M) - IP_1(P) - EA(P))$ as shown in I.2.2. In fact, there is only a constant difference between the scales of the kinetic energy loss of the projectile and the excitation energy, 2.8eV corresponding to the energy defect of the interaction (see **Table 7**). Therefore, in **Figure 51**, the bottom scale has been converted to the excitation energy of the target with a shift of 2.8 eV with respect to the top scale. To well locate the center of the population distributions, Gaussian fitting for each curve has been performed and plotted in **Figure 51**. From heavy to lighter fragments, we see an obvious shift from low to higher energy. For convenience of discussion, both the mean excitation energy and the Full Width at Half Maximum (FWHM) for each channel are listed in **Table 8**. However, one should keep in mind that the curves in fig.12 especially the FWHM of the curves do not represent the excitation energy distribution of the parent targets for each fragmentation channel due to the important

experimental broadening. Only the center of each curve has a clear physical signification corresponding to the mean excitation energy of the parent ions prior to the fragmentation.

Table 8. Mean excitation energies of the $FeTPPCl^{2+}$ parent ion and FWHM of the raw measured distributions for the dissociation channels measured in F^+ on FeTPPCl collisions. The number of counts of each fragment is also given.

m/q	Element	Counts	Mean excitation energy E* (eV)	FWHM (eV)
669/2	$FeTPP^{2+}$	5060	7.8	7.4
591/2	$(FeTPP\text{-}ph)^{2+}$	9310	9.8	7.5
513/2	$(FeTPP\text{-}2ph)^{2+}$	2520	13.7	11.2
669/3	$FeTPP^{3+}$	380	13.3±5	10.9
40/2	Ar^{2+}	1370	0	5.7

In **Figure 51**, the curve with square symbol corresponds to the neutral Cl atom loss from the parent ion, i.e., $FeTPPCl^{2+} \rightarrow FeTPP^{2+}+Cl$. In the formation of the corresponding parent ions, the typical kinetic energy loss of the projectile is about 5 eV, corresponding to a measured mean excitation energy of 7.8 eV for the parent ion. The next step of the dissociation is shown by dot in **Figure 51** corresponding to one more neutral loss of a phenyl group from the intermediate product $FeTPP^{2+}$ leading to the measured fragment $(FeTPP\text{-}ph)^{2+}$. The mean excitation energy of $(FeTPPCl^{2+})^{**}$ parent ions for this channel is measured to be about 9.8 eV. It presents a shift of 2eV to higher energy comparing to the channel $FeTPP^{2+}$. For the channel $(FeTPP\text{-}2ph)^{2+}$, where two neutral phenyl groups are evaporated after the emission of Cl from $FeTPPCl^{2+}$, the mean excitation energy is centered at about 13.7 eV. One electron emission from $FeTPP^{2+}$ produces triply charged ions $FeTPP^{3+}$. Due to the low production yield and poor statistics for this decay channel, it is difficult to locate the center of the distribution precisely. Nevertheless, we give an approximate mean excitation energy value of 13.3 eV.

IV.3.2. CIDEC method with H^+ projectile at 3 keV

IV.3.2.1. Excitation energy window in collisions between H^+ projectiles at 3 keV and FeTPPCl

Using 3keV H^+ projectile beam, we have measured the kinetic energy loss for outgoing negative H^- projectiles following the same procedure as in the section IV.3.1. **Figure 52** gives the mass spectrum of all fragment ions. For comparison, the spectrum obtained with F^+ impact was superposed on it (dash line). In the spectrum of H^+ collision, the peak of parent ion $FeTPPCl^{2+}$, that was absent in the spectrum of F^+ collision, was observed with a low count number. To show it clearly, it was multiplied by a factor of 20. Another notable difference of the two spectra is the relative intensities of the fragment peaks. Compared to the case of H^+ collisions, the mass spectrum with F^+ presents an obvious shift from heavy fragments to light ones. This suggests that, in the case of fluorine projectile, a larger amount of energy was deposited on the target than in the case of H^+, leading to higher intensities of light fragments. Direct evidence can be found in the excitation energy measurement in the following.

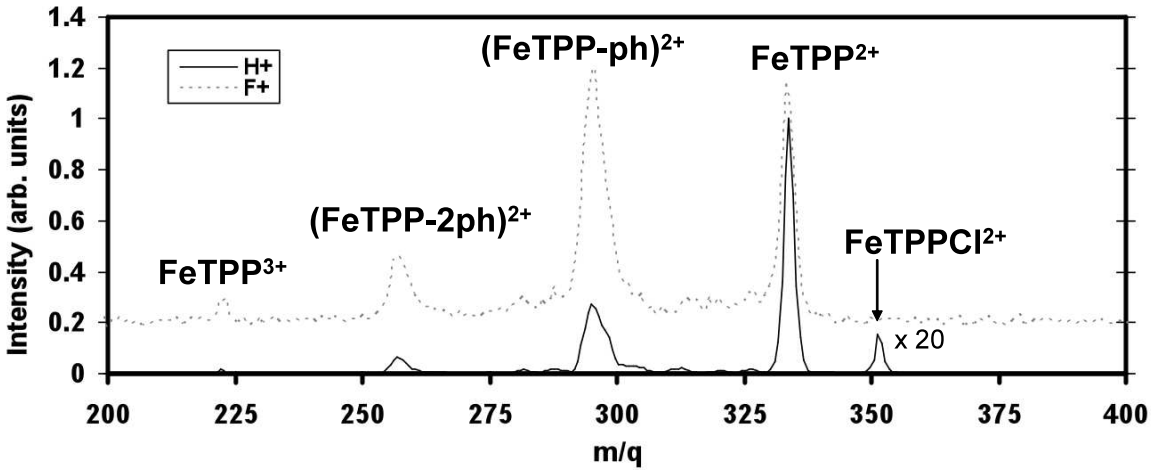

Figure 52. The mass spectrum of the fragments measured in 3keV H^+ on FeTPPCl collision. The parent ion $FeTPPCl^{2+}$ was observed with low intensity; to present it more clearly, it was multiplied by a factor of 20. For comparison, the spectrum for F^+ projectile was superposed on it.

Figure 53 is the correlation spectrum between the recoil ions and scattered projectiles. It shows a similar pattern as F^+ projectile (**Figure 49**). We see also the long tails with slope for several spots.

Figure 54 shows the global population distribution obtained by the vertical projection of the whole spectrum **Figure 53**. The conversion from the analyzer voltage scanning channel to the kinetic energy loss scale is performed using the H^- peak from collisions with the reference gas, Ar (not shown in the spectrum). The H^- peak obtained in H^+ + Ar collision was assigned to an energy loss of 30.7 eV (II.3.3.1). From **Figure 54** it is found that, for the two projectiles, the

profiles of the global population distribution in the kinetic energy loss scale are similar. While due to the different electronic structure of the projectiles, different energy defect values (2.8 eV for F^+ impact, and -3.6 eV for H^+ impact) should be considered in the two collisions. (see **Table 7**). In **Figure 55** the two global anion kinetic energy analysis curves are presented with the excitation energy scale. For F^+ collision, the excitation energy is shifted to larger values globally. It means that an excitation energy window centered at a higher value is opened by F^+ impact. This explains the global population shift to lighter fragments in the mass spectrum obtained with F^+ impact (**Figure 52**).

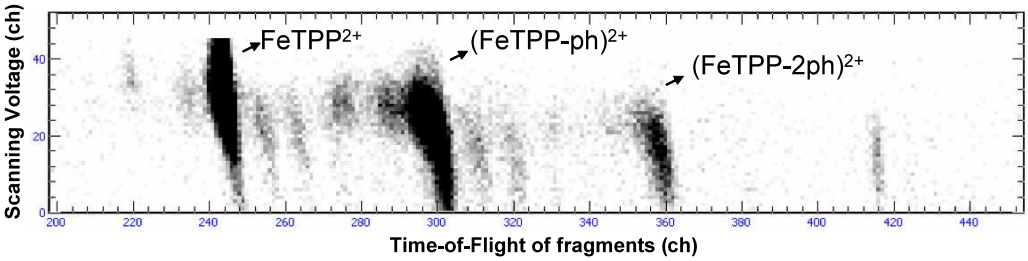

Figure 53. Correlation spectrum between recoil ions and scattered projectiles measured in 3keV H^+ on FeTPPCl collision, the scattered projectile is detected with (q-2), i.e., negative H^- ions. The experiment was operated in energy measurement mode. The horizontal axis stands for the TOF of the fragment, and the vertical for the scanning voltage of the analyzer.

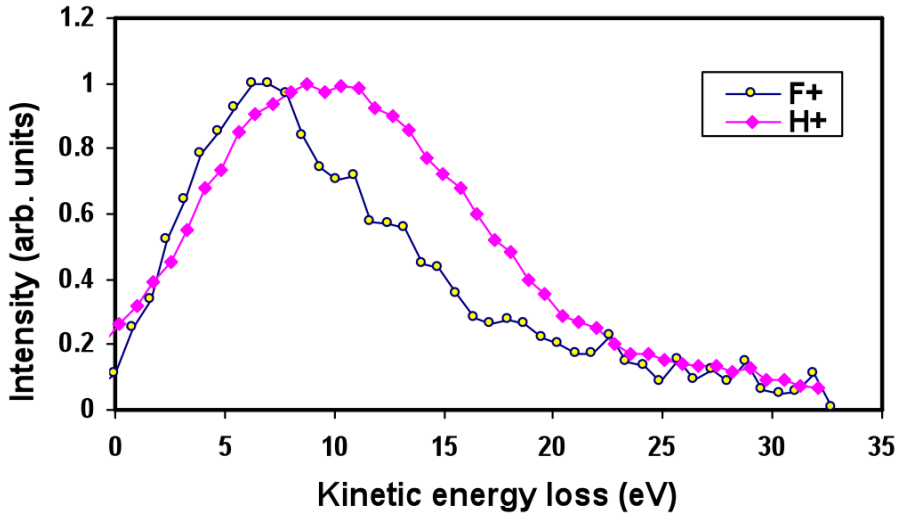

Figure 54. The comparison of the global population distributions of scattered projectiles produced in H^+ and F^+ on FeTPPCl collisions, circles for F^+ and diamonds for H^+. The horizontal axis is converted to the projectile kinetic energy loss.

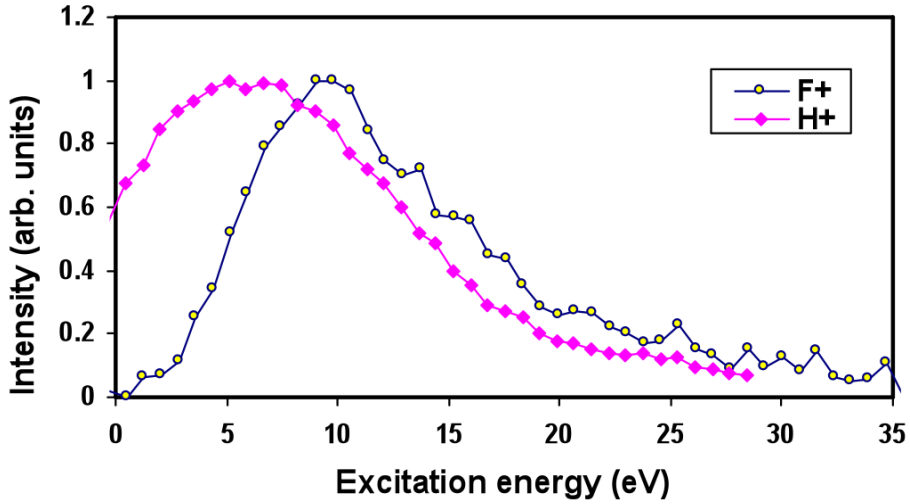

Figure 55. The comparison of the global excitation energy distributions of all fragments produced in H^+ and F^+ on FeTPPCl collisions, circle for F^+ and diamond for H^+.

IV.3.2.2. Excitation energy distributions of parent $FeTPPCl^{2+}$ ions for individual fragmentation channels in collisions with H^+

In **Figure 56**, we present individual raw population distributions for dominant dissociation channels obtained by vertical projection of the main spots in the **Figure 53**. The horizontal axis has been converted to the scale of excitation energy of parent $FeTPPCl^{2+}$ ions. Due to the large broadening of the peak H^- from the reference gas, the curves in **Figure 56** were not deconvoluted. The mean excitation energies for all fragmentation channels obtained from the center of each curve are presented in table 3. The widths (FWHM) of these curves are also reported in table 3 for qualitative indication. This value does not correspond to the width of the excitation energy distribution of the parent ions for the corresponding fragmentation channel due to the contribution of instrumental broadening.

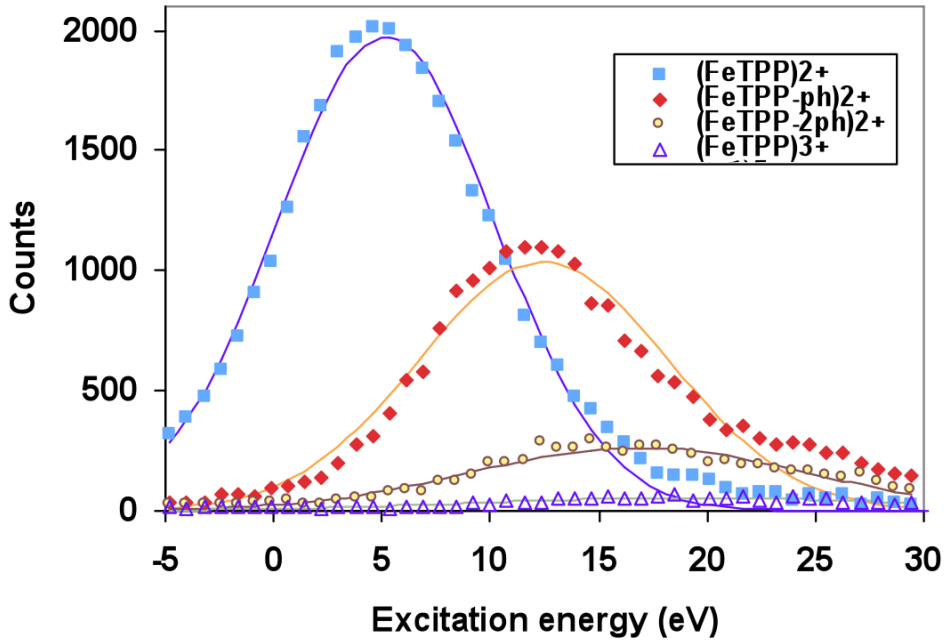

Figure 56. Population distribution for individual fragmentation pathway, measured in 3keV H^+ on FeTPPCl collision experiment. The horizontal scale is converted to the excitation energy of parent $FeTPPCl^{2+}$ ions. Discrete symbols stand for the experimental results, and the lines stand for the Gaussian fits for corresponding channel.

Table 9. Mean excitation energy of the $FeTPPCl^{2+}$ parent ions and FWHM of the measured curves for the dissociation channels measured in H^+ on FeTPPCl collision, the number of counts of each fragment is also given.

m/q	Element	Counts	Mean excitation energy E* (eV)	FWHM (eV)
669/2	$FeTPP^{2+}$	32600	4.2	11.9
591/2	$(FeTPP\text{-}ph)^{2+}$	20100	11.5	13.6
513/2	$(FeTPP\text{-}2ph)^{2+}$	6320	15.8	18.2
669/3	$FeTPP^{3+}$	<1500	18±5	23.4
40/2	Ar^{2+}			9.0

IV.3.3. Discussion

Comparing the results from H^+ and F^+ projectile impact (**Table 8** and **Table 9**), we see comparable mean excitation energies for the formation of fragments $(FeTPP\text{-}ph)^{2+}$ and $(FeTPP\text{-}2ph)^{2+}$. For $FeTPP^{3+}$, due to the low statistics, large uncertainty exists in the reported result, leading to the pronounced difference in the measured mean energy values. The large difference between the mean excitation energies to obtain the fragment $FeTPP^{2+}$ is remarkable, 7.8 eV for F^+ and 4.2 eV for H^+. This will be discussed in detail in the next section.

For both projectiles, the difference of mean excitation energy for the channels $(FeTPP\text{-}ph)^{2+}$ and $(FeTPP\text{-}2ph)^{2+}$ was measured to be about 4 eV. This value corresponds to the energy necessary to break the C-C bond between a phenyl and the main cycle of the molecule. It is close to the value obtained in an *ab initio* calculation. Using the molecular quantum chemistry GAMESS-U.S. program, the dissociation energy to evaporate one phenyl group from intermediate parent ion $FeTPP^{2+}$ to form $(FeTPP\text{-}ph)^{2+}$ was determined to be 4.4 eV (private communication, A. Allouche) . This calculation under the Gabedit user interface with the 6-31G base and the B3LYP correlation method was performed [95]. The obtained value is slightly larger than the energy necessary for a C-C bond cleavage, 348KJ/mol (3.6eV) [97]. So, consider the successive loss of phenyl group from $FeTPP^{2+}$ to form $(FeTPP\text{-}ph)^{2+}$ and $(FeTPP\text{-}2ph)^{2+}$, for the first step, the measured mean energy necessary is about 2 to 3 times the dissociation energy, while for the loss of the second phenyl, an extra energy equivalent to the dissociation energy is needed. This is the typical signature of a statistic dissociation process.

It is also interesting to compare our measured results with those obtained with different techniques, for instance electron impact induced dissociation. In those experiments, the measured parameter is usually the appearance energy for interested fragment. It includes the energy needed for the ionization to form the charged parent ions, and the excitation energy necessary for further decay to form corresponding fragments. In our experiment, if we could determine the minimum excitation energy precisely, we would be able to estimate the appearance energy by adding the first and the second ionization potentials of FeTPPCl molecule to this value in a similar procedure as in the case of adenine target. In the present experiment, however, due to the instrumental enlargement and the energy dispersion of the primary beam, it is difficult to deconvolute the measured profile to determine the appearance energy precisely. In the cases where the widths of physical excitation energy profile for a fragment channel is much smaller than the total experimental enlargement, as the first approximation, the minimum energy value and the center of the measured population distribution are nearly equivalent.

To compare with the appearance energy measured in electron impact experiment, we use the sum of mean excitation energy ($\bar{E}_{exc}$) and the first two ionization potentials of FeTPPCl (I_1+I_2). In the following, let us call this value $E(P_o \rightarrow P_o^{2+}*)$, which equals to $\bar{E}_{exc} + I_1+I_2$. For fluorine collision, we obtain the values $E(P_o \rightarrow P_o^{2+}*)$ for fragmentation channels $FeTPP^{2+}$, $(FeTPP\text{-}ph)^{2+}$, and $(FeTPP\text{-}2ph)^{2+}$ to be 25.8 eV, 27.8 eV, and 31.7 eV, respectively. In electron impact ionization experiment [22] (**Table 10**), the appearance energies for channels with fragments $(FeTPP\text{-}ph\text{-}H)^{2+}$ and $(FeTPP\text{-}2ph)^{2+}$ are measured to be 30eV and 32eV, respectively; these values are very close to our $E(P_o \rightarrow P_o^{2+}*)$ values in both H^+ and F^+ case.

Table 10. The comparison between the $E(P_o \rightarrow P_o^{2+}*)$ measured in our experiment and the appearance energy determined in electron impact .

Element	$E(P_o \rightarrow P_o^{2+}*)$ (eV)		Appearance energy (eV)
	H^+	F^+	
$FeTPP^{2+}$	22.2	25.8	18
$(FeTPP\text{-}ph)^{2+}$	29.5	27.8	30
$(FeTPP\text{-}2ph)^{2+}$	33.8	31.7	32

For the fragment $(FeTPP)^{2+}$, the electron impact experiment gives an appearance energy of 18eV [22], corresponding to the sum of the first and second ionization potential. In our experiment, the value $E(P_o \rightarrow P_o^{2+}*)$ for this channel was measured respectively to be 25.8 eV and 22.2 eV in collisions with F^+ and H^+ projectiles This, in fact, is not surprising. According

to the appearance energy in **Table 10**, the loss of the first phenyl fragment needs an excitation energy of about 12eV (30-18 eV). $(FeTPP)^{2+}$ fragments prepared with an energy lower than this value could stay stable in our experimental time window regarding to the phenyl loss process. For the two collision systems, the kinetic energy loss distributions of anions F^- and H^- are rather similar (**Figure 54**). The mean kinetic energy loss depends mainly on the collision distance for the formation of anions, which is more sensitive to the size of the molecule than the structure of the projectile ion. However, the different values on the energy defect δ in these two collision systems allows for the opening of an excitation energy window with a shift of about 6 eV to higher values in the case of F^+ impact than in H^+ impact. Therefore, using F^+ projectile beam, $(FeTPP)^{2+}$ fragments were produced at a mean excitation energy of 8 eV that is higher than in collisions with H^+, but still lower than the appearance energy of $(FeTPP\text{-}ph)^{2+}$.

IV.4. *More precise analysis: the nH_2 loss process*

Previously, we have mentioned the long tails of the tilted spots on the correlation spectra in **Figure 49** and **Figure 53**. This feature will be analyzed in this section and attributed to the nH_2 loss process. The hydrogen loss processes have been observed in other experiments with different techniques. In the electron ionization (EI) experiment [22], even with low intensities, the nH_2 loss processes have been observed for both mono-charged and doubly-charged parent ions. With the multi-collision-induced dissociation method and electro-spray ionization tandem mass spectrometry (ESI/CID method) [74], mono-charged fragments with the loss of hydrogen have also been observed. The branching ratios of such processes have been determined to be much higher than in EI experiments.

IV.4.1. TOF analysis with higher precision

In this section, the fragmentation channel associated to the spot denoted by $FeTPP^{2+}$ will be analyzed in details. Indeed, channels involving nH_2 loss lead to minor shifts in TOF spectrum due to the small relative mass variation. It is therefore necessary to analyze the TOF mass spectrum with a better precision. The assignment of the sub-channels $(FeTPP\text{-}nH_2)^{2+}$ will be first performed using the TOF spectroscopy, then confirmed with a coincidence

analysis of the excitation energy of the parent molecules. In spite of the small shift in the TOF spectrum for these sub-channels, due to the increasing number of breaking bonds, a more discernible difference in excitation energy of the parent molecular ions might be expected for successive loss of H_2 units. For example, in the case of fragmentation channels around the peak named $FeTPP^{2+}$, one H_2 unit loss results in only two mass unit shifts on the mass spectrum, while a clear shift in the excitation energy measurement is shown by the long tail of the spot $FeTPP^{2+}$ in **Figure 49**. Finally, the difference in the measured mean excitation energy values for $FeTPP^{2+}$ channels in collisions with H^+ and F^+ projectiles will be attributed to different branching ratios for the sub-channels $(FeTPP\text{-}nH_2)^{2+}$ (n=0, 1, 2).

In previous sections, the TOF spectra with a scale of 1024 have been obtained from the original TDC data divided by a factor of 64. The resolution of the TDC is 0.5 ns/channel and the original data is in 16 bytes. The maximum time scale 32.768 μs corresponds therefore to 2^{16}=65536. The mass resolution for heavy fragments was not high enough to allow for the discrimination of the sub-channels $(FeTPP\text{-}nH_2)^{2+}$ clearly on the mass spectrum. In fact, the difference in the nominal positions of peaks for ions $(FeTPP)^{2+}$ and $(FeTPP\text{-}H_2)^{2+}$ is around 1 channel in a 1024 channel spectrum. So, several decay channels mixed together in the corresponding spot $FeTPP^{2+}$, and a long tail with slope appears on the correlation spectrum. In this section, the raw TDC data with a scale from 0 to 4096 are analyzed to improve the precision of the TOF spectrum calibration.

In the following, both the TOF spectra and the excitation energy population distributions will be fitted with Gaussian function to discriminate channels with fragments $(FeTPP\text{-}nH_2)^{2+}$.

IV.4.2. H_2 loss in F^+ on FeTPPCl collisions

In F^+ on FeTPPCl collisions, the separation of the excitation energy distributions for fragments with the loss of n units of H_2 from the ion $FeTPP^{2+}$ was performed in three steps. First, the nominal centers on the TOF spectrum for considering fragments, such as $FeTPP^{2+}$, $(FeTPP\text{-}H_2)^{2+}$, and $(FeTPP\text{-}2H_2)^{2+}$ were determined from the calibration relation with a scale of 4096. Second, the measured peak named $FeTPP^{2+}$ in the mass spectra (or TOF spectra) was fitted with sub-peaks $(FeTPP\text{-}nH_2)^{2+}$ (n=0,1,2) at the nominal TOF values. The count number for each corresponding fragment was extracted from this first fit. In the next step, the population distribution curve as a function of the energy was fitted to get the centers of the energy distributions for all involved $(FeTPP\text{-}nH_2)^{2+}$. In this second fit, the ratio between the

count numbers of $(FeTPP\text{-}nH_2)^{2+}$ fragments obtained in the TOF spectrum fit was kept as a fixed parameter. Details of the analysis procedure are given in the following.

a. As described in chapter II, the time-of-flight of the fragment is proportional to the square root of its mass over charge ratio. Using the measured positions of the known fragments on the TOF spectrum, such as Ar^{2+}, Cl^{+}, ph^{+}, etc., one straight line can be determined by performing a linear fitting. Using this calibration relation, the nominal position on the TOF spectrum for a fragment with a given mass and charge state can be calculated. In this way, the nominal centers of the fragments $FeTPP^{2+}$, $(FeTPP\text{-}H_2)^{2+}$ and $(FeTPP\text{-}2H_2)^{2+}$ were determined to be at channels 1582.5, 1587.1 and 1591.8 on the TOF spectrum, respectively.

b. The peak named $FeTPP^{2+}$ was extracted from the measured time-of-flight spectrum (labeled as Exp and with square symbol in **Figure 57**). The experimental data were fitted using three Gaussian distributions (fit0, fit1 and fit2). The centers of fit0, fit1 and fit2 were fixed at channels 1582.5, 1587.1 and 1591.8, while the widths and amplitudes of the three distributions were set to be variable parameters. The iterative calculation was realized by using the solver function in Microsoft Excel. After the operation, the number of count of the distribution fit0 was found negligible and the numbers of the other two distributions fit1 and fit2 were found to be 3690 and 970 (**Table 11**). The ratio of the numbers of count between the two distributions fit1 and fit2 was found to be 1:0.263. The obtained fit1 and fit2 were plotted in **Figure 57**, as well as the sum of these sub-peaks fitS = fit1 + fit2. The contribution of the sub-peak $FeTPP^{2+}$ without the loss of H_2 was neglected in the following.

c. The excitation energy population distribution of the spot named $FeTPP^{2+}$ was fitted with a certain number of independent Gaussian distributions corresponding to the number of sub-peaks found in the step b. In the present case, two Gaussian distributions fit1' and fit2' were used corresponding to the loss of one and two H_2 units, $(FeTPP\text{-}H_2)^{2+}$ and $(FeTPP\text{-}2H_2)^{2+}$. The ratio of the numbers of count of the two distributions was fixed to 1:0.263 in the fitting. While the centers and the widths of the two Gaussian distributions were set as free parameters. The measured spectrum (labeled as Exp), the fitted Gaussian distributions (fit1' and fit2'), and the sum of the two Gaussian fittings (fitS'=fit1'+fit2') are all presented in **Figure 58**.

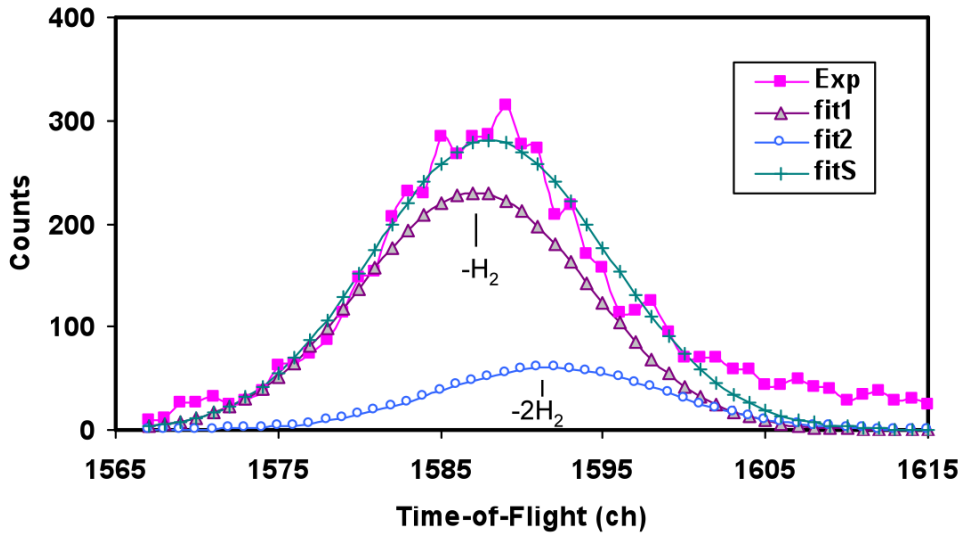

Figure 57. Illustration for the TOF spectrum separation of fragment with nominal mass around 669 measured in F^+ + FeTPPCl collision. The corresponding relation of the labels: experimental data (Exp); Gaussian fitting for fragment $(FeTPP\text{-}H_2)^{2+}$ (fit1); Gaussian fitting for fragment $(FeTPP\text{-}2H_2)^{2+}$ (fit2); the sum of the Gaussian fittings for fragments $(FeTPP\text{-}H_2)^{2+}$ and $(FeTPP\text{-}2H_2)^{2+}$ (fitS).

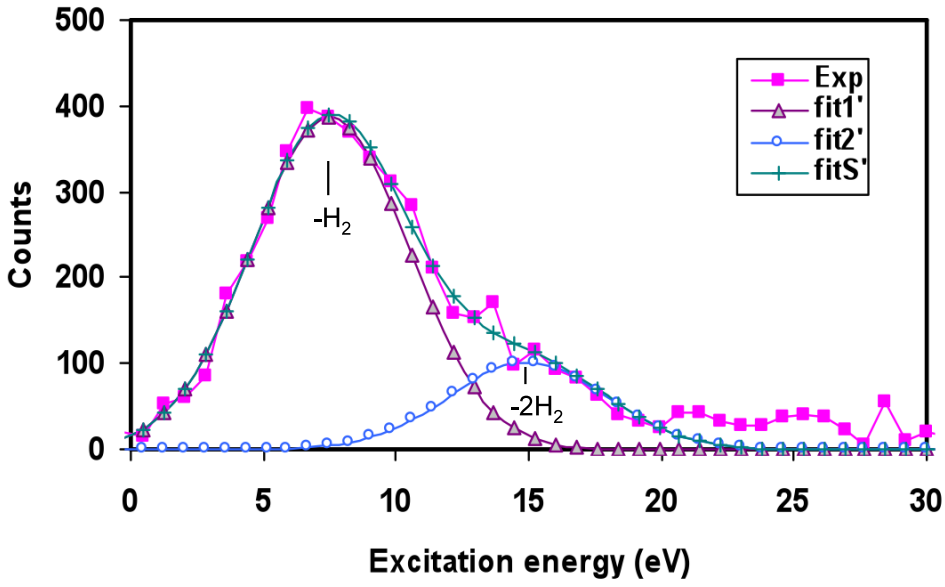

Figure 58. Illustration for the separation of the excitation energy distribution corresponds to fragment with nominal mass around 669, measured in F^+ + FeTPPCl collision. The corresponding relation of the labels: experimental data (Exp); Gaussian fitting for fragment $(FeTPP\text{-}H_2)^{2+}$ (fit1'); Gaussian fitting for fragment $(FeTPP\text{-}2H_2)^{2+}$ (fit2'); the sum of the Gaussian fittings for fragments $(FeTPP\text{-}H_2)^{2+}$ and $(FeTPP\text{-}2H_2)^{2+}$ (fitS').

The experimental distribution was well fitted by two Gaussian excitation energy population distributions fit1' and fit2' for which the numbers of count were fixed to be 3690 and 970 respectively as found in the step b. The centers of fit1' and fit2' are presented in **Table 11**. They are attributed to mean excitation energies for fragmentation channels $(FeTPP\text{-}H_2)^{2+}$ and $(FeTPP\text{-}2H_2)^{2+}$ determined to be 7.5 eV and 14.9 eV respectively.

Now we can look into more details about the decay channels in this collision. According to the analysis of this section, in 3keV F^+ and FeTPPCl interaction, when anions outgoing projectiles F^- were selected, neither parent ion $FeTPPCl^{2+}$, nor intermediate ion $FeTPP^{2+}$ could survive. The heaviest survival fragment observed is $(FeTPP\text{-}H_2)^{2+}$. It corresponds to a mean excitation energy of 7.5 eV for the parent $(FeTPPCl^{2+})^{**}$. One of the competitive decay channel at a slightly higher energy is the formation of $(FeTPP\text{-}ph)^{2+}$, which corresponds to one phenyl group loss from intermediate ion $(FeTPP^{2+})^{**}$, at a mean excitation energy of 9.8 eV (**Table 8**). For comparison, mean energy and count number of main fragmentation channels are presented in **Figure 59** under the envelope of the measured total excitation energy distribution.

Table 11. Mean excitation energies after the separation of concerned $-H_2$ loss processes for fragments around the nominal mass of 669. The number of counts of each fragmentation channel was also given.

	Projectile F^+		Projectile H^+	
Element	Mean excitation energy (eV)	Counts	Mean excitation energy (eV)	Counts
$FeTPP^{2+}$	-	0	2.6	20700
$(FeTPP\text{-}H_2)^{2+}$	7.5	3690	7.8	10660
$(FeTPP\text{-}2H_2)^{2+}$	14.9	970	-	0

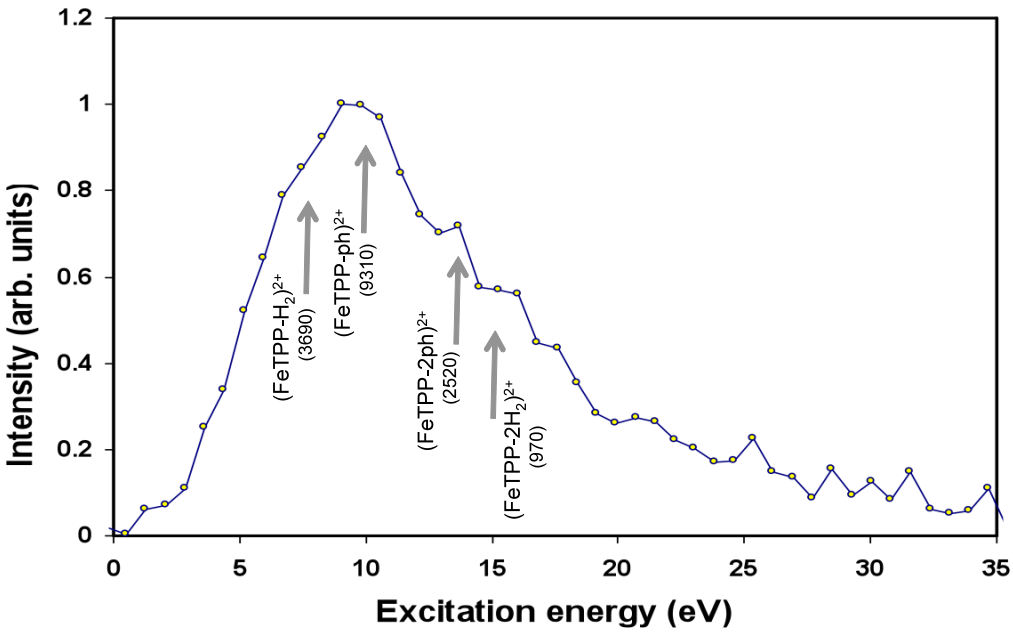

Figure 59. Mean excitation energy and count number of main fragmentation channels plotted under the envelope of the measured global excitation energy distribution in F^+-FeTPPCl collisions at 3keV.

IV.4.3. H_2 loss in H^+ on FeTPPCl collisions

In the case of H^+ collision, we have performed similar data analysis. The experimental data of the peak, named $FeTPP^{2+}$ previously, were fitted with two TOF sub-peaks centered at channels 976, and 982 corresponding to $FeTPP^{2+}$ and $(FeTPP\text{-}H_2)^{2+}$ respectively (**Figure 60**). The numbers of count for the two involved sub-channels were found to be 20700 and 10660 respectively (**Table 11**).

The excitation energy population distribution was well fitted with two Gaussian distributions of count numbers fixed to the values obtained previously in the TOF spectrum fitting (**Figure 61**). The centers of the two Gaussian distributions attributed to mean excitation energies corresponding respectively to $FeTPP^{2+}$ and $(FeTPP\text{-}H_2)^{2+}$ channels are presented in **Table 11**. For these two channels, the mean excitation energies are determined to be 2.6 eV and 7.8 eV respectively. In **Figure 62**, under the envelope of the measured total excitation energy distribution, the mean excitation energies of the four main decay channels are represented by arrows.

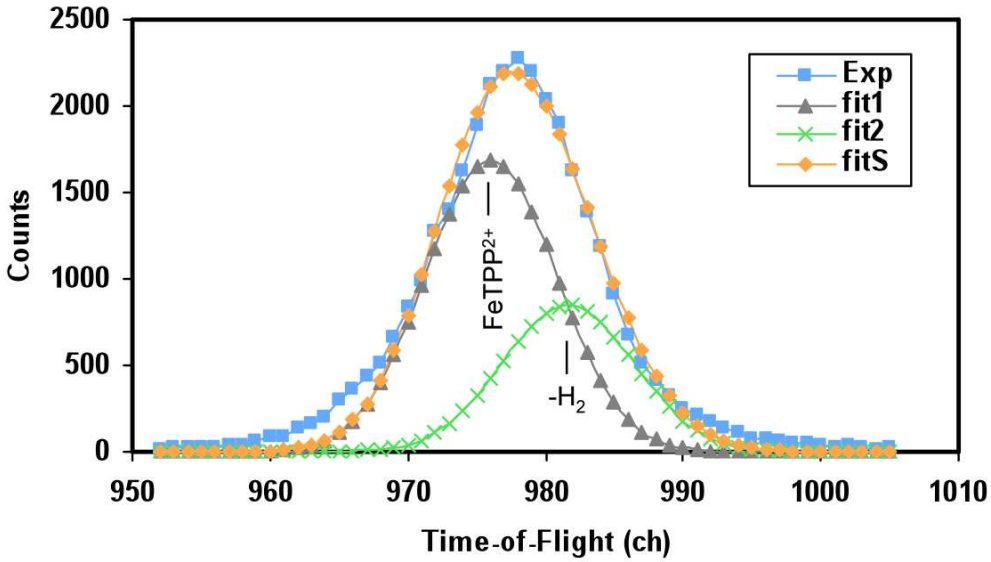

Figure 60. Illustration for the TOF spectrum separation of fragment with nominal mass around 669 measured in H^+ + FeTPPCl collision. The corresponding relation of the labels: experimental data (Exp); Gaussian fitting for fragment $FeTPP^{2+}$ (fit1); Gaussian fitting for fragment $(FeTPP\text{-}H_2)^{2+}$ (fit2); the sum of the Gaussian fittings for fragments $FeTPP^{2+}$ and $(FeTPP\text{-}H_2)^{2+}$ (fitS).

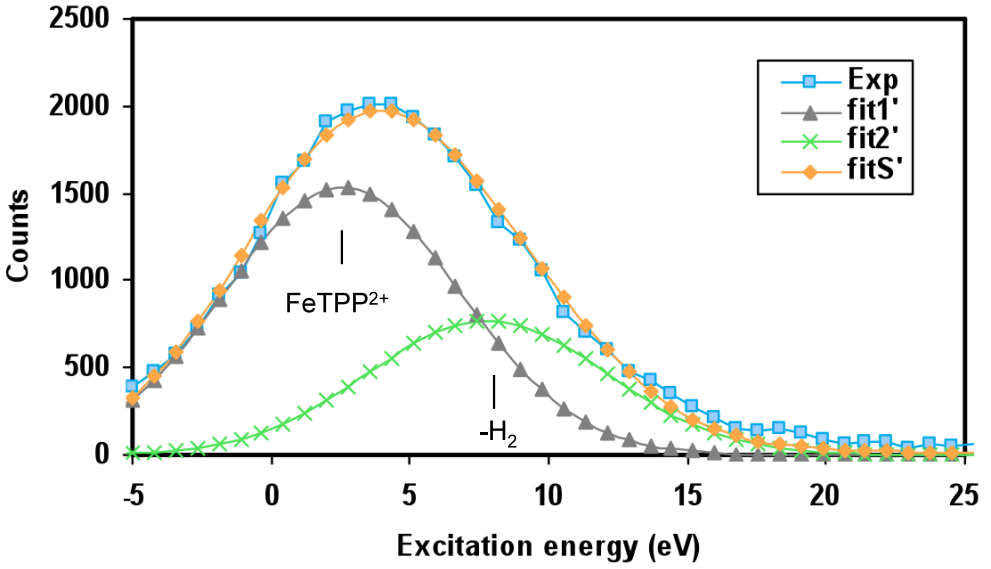

Figure 61. Illustration for the separation of the excitation energy distribution corresponds to fragment with a nominal mass of 669, measured in H^+ + FeTPPCl collision. The corresponding relation of the labels: experimental data (Exp); Gaussian fitting for fragment $FeTPP^{2+}$ (fit1'); Gaussian fitting for fragment $(FeTPP\text{-}H_2)^{2+}$ (fit2'); the sum of the Gaussian fittings for fragments $FeTPP^{2+}$ and $(FeTPP\text{-}H_2)^{2+}$ (fitS').

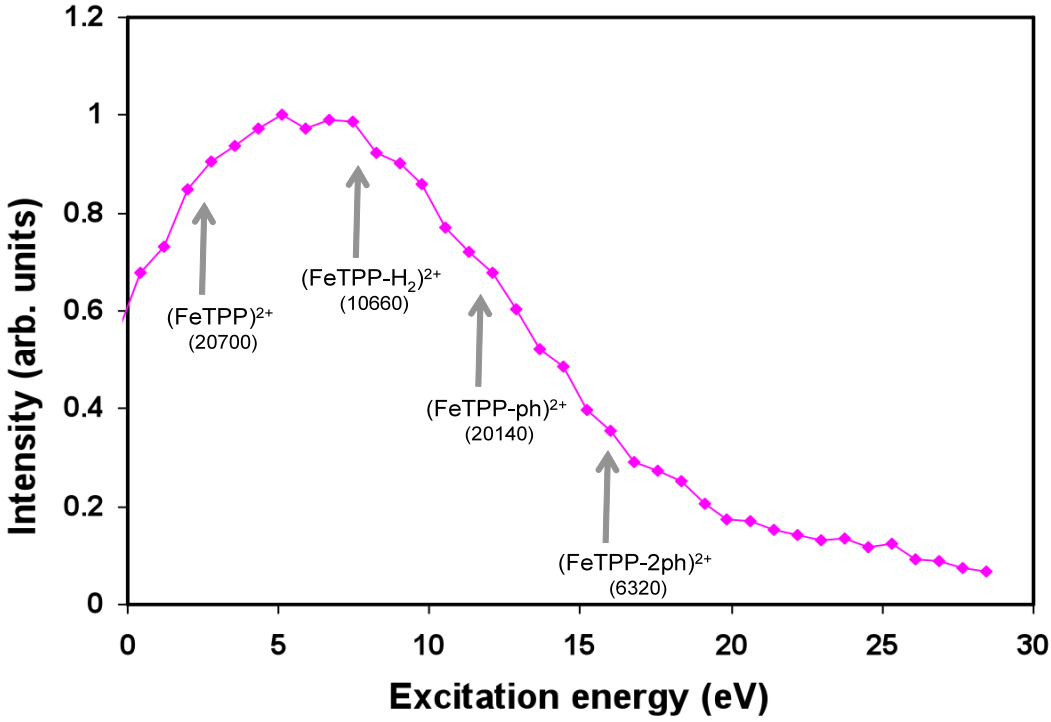

Figure 62. Mean excitation energy and count number of main fragmentation channels plotted under the envelope of the measured global excitation energy distribution in H^+-FeTPPCl collisions at 3keV.

IV.4.4. Discussions

From the above analysis, considering both projectiles (F^+ and H^+), the fragmentation pattern of the ion $FeTPPCl^{2+}$ can be given with more precision. The observed main decay channels, with the measured mean excitation energies and count numbers are presented in **Figure 63** and in **Table 12**.

In the dissociation pattern of dication $FeTPPCl^{2+}$, the first step is the loss of neutral chlorine. From the intermediate ions $FeTPP^{2+}$, there are several dissociation routes:

- the successive loss of H_2 units;
- the successive loss of neutral phenyl groups;
- the loss of a H_2 followed by the loss of a phenyl group or reversely.

The last processes lead to the enlargement of the peak named $(FeTPP\text{-}ph)^{2+}$ in both the TOF and the energy distribution spectra and to the tilted form of this spot in the 2-D spectra (**Figure**

49 and **Figure 53**). Due to the complexity of the involved processes, this peak was not analyzed in this work.

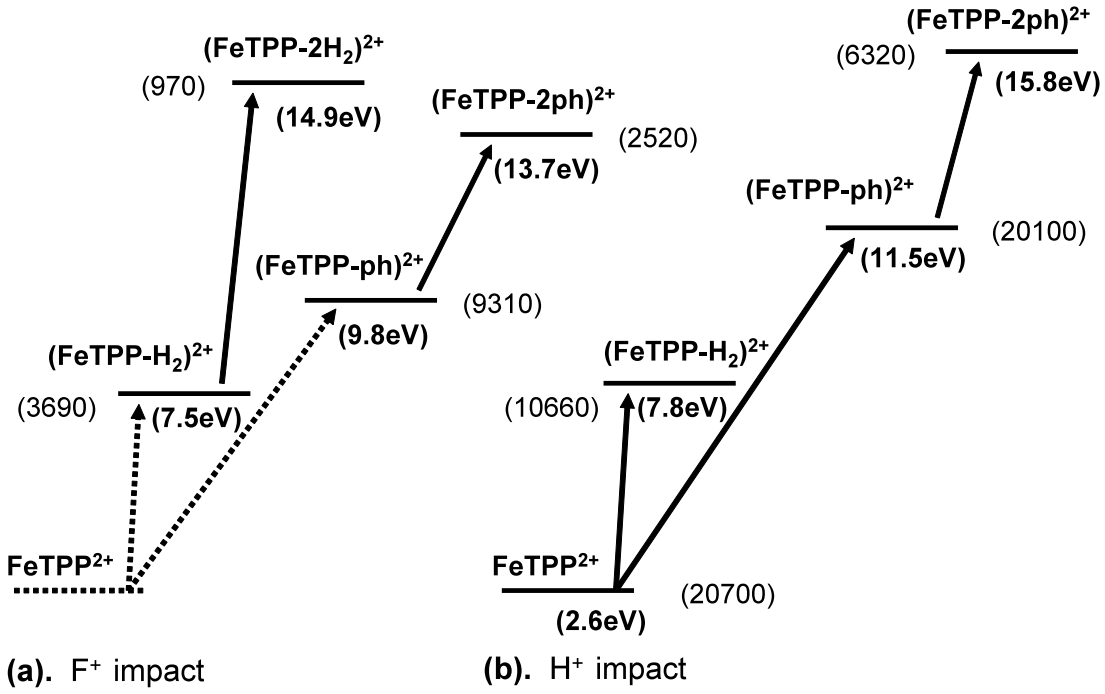

Figure 63. The decay pattern of doubly charged parent ion $FeTPPCl^{2+}$ observed in (a). F^+ impact, and in (b). H^+ impact. The mean excitation energies and numbers of count for all the channels are presented.

The loss of a H_2 from the intermediate ions $FeTPP^{2+}$ is the lowest energy cost channel. In spite of the very different excitation energy windows in collisions with the two projectiles, the mean energy measured for this channel is very near, 7.5 and 7.8 eV (**Table 12**). The different values on the mean excitation energy measured for the peak named $FeTPP^{2+}$ in the section IV.3 find the explication here. In the case of F^+ projectile, this peak is composed of $(FeTPP\text{-}H_2)^{2+}$ and $(FeTPP\text{-}2H_2)^{2+}$ fragments related to a higher mean excitation energy value, 7.8 eV. In the case of H^+ projectile, it is contributed by $FeTPP^{2+}$ and $(FeTPP\text{-}H_2)^{2+}$ fragments due to a lower mean excitation energy value, 4.2 eV.

The loss of a phenyl group is a competitive channel for the loss of a H_2 unit with a mean energy slightly higher, measured to be 9.8 eV in the cases of F^+ projectiles. For one phenyl group evaporation, a single C-C bond is broken; while for the loss of one H_2 unit, at least two C-H bonds cleavage are needed. The cleavage of one C-H bond needs an amount of energy of 413KJ/mol (4.1eV). While the formation of H_2 releases 4.5eV of H-H bond energy. In total, this simple energy balance shows that 3.7eV is needed for the loss of a H_2 unit. This value is

smaller than the calculated value for the loss of a phenyl group from $FeTPP^{2+}$ (4.4eV). This is in qualitative agreement with the fact that $(FeTPP\text{-}H_2)^{2+}$ channel is observed at lower energy value than $(FeTPP\text{-}ph)^{2+}$. For the direct loss of a H_2 unit, a rearrangement, for example, the coupling of two adjacent hydrogen atoms might be involved, which reduces the binding energy of each H-C bond. Similar processes have been observed frequently in organic chemistry.

Table 12. Mean excitation energies and number of counts for fragmentation channels from $FeTPPCl^{2+}$ parent ions.

	Projectile F^+		Projectile H^+	
Element	Mean excitation energy (eV)	Counts	Mean excitation energy (eV)	Counts
$FeTPP^{2+}$	-	0	2.6	20700
$(FeTPP\text{-}H_2)^{2+}$	7.5	3690	7.8	10660
$(FeTPP\text{-}ph)^{2+}$	9.8	9310	11.5	20100
$(FeTPP\text{-}2ph)^{2+}$	13.7	2520	15.8	6320
$(FeTPP\text{-}2H_2)^{2+}$	14.9	970	-	0

The peak named $(FeTPP\text{-}ph)^{2+}$ is rather complex. It might be contributed by three possible processes: the loss of a phenyl group from $FeTPP^{2+}$, the loss of a H_2 followed by the loss of a phenyl group, the loss of a phenyl group followed by the loss of a H_2. The mean energy associated to this peak depends sensitively on the branching ratios of these channels. The two values, 9.8 eV and 11.5 eV for the cases of F^+ and H^+ projectiles, indicate that in collisions with H^+, the contribution of the channel $(FeTPP\text{-}H_2\text{-}ph)^{2+}$ is larger than in collisions with F^+. As already mentioned in section IV.3.3 and shown again in **Figure 59**, the loss of a second phenyl group needs an extra energy of about 4eV, comparable to the dissociation energy needed for the loss of the first phenyl group. In the case of H^+ projectiles, the energy difference between $(FeTPP\text{-}H_2)^{2+}$ and the named peak $(FeTPP\text{-}ph)^{2+}$ happens to be about 4 eV. This suggests strongly that this last peak might be principally due to the loss of a phenyl group from the intermediate fragment $(FeTPP\text{-}H_2)^{2+}$.

Similar to the loss of the first phenyl group, for the loss of the first H_2 unit, the mean excitation energy is measured to be about twice the estimated dissociation energy (3.7 eV). It indicates that the loss of the first H_2 is also a statistical process. However, for the loss of two H_2 units, the mean excitation energy is measured to be 14.9 eV. It is notable that in this case, contrary to the loss of the second phenyl group, the extra energy needed for the loss of the

second H_2 unit is much higher than the expected dissociation energy (3.7eV). It is equivalent to the mean energy measured for the loss of the first H_2. This suggests that a dissociation dynamics different from that of the successive loss of phenyl groups is involved in the H_2 loss.

The loss of H_2 units has been also studied in the ESI/CID experiment. In the work of Gozet et al. [74] the relative abundance of a variety of dissociation pathways were probed as a function of the collision offset voltage applied to the Paul trap [74] (see **Figure 64**). Comparing the abundance distributions for the formation of fragments $(FeTPP\text{-}H_2)^+$ and $(FeTPP\text{-}2H_2)^+$ resulted from $FeTPP^+$, the offset voltages are centered to 85V and 110V, respectively. The fragment $(FeTPP\text{-phenyl})^+$ or $(FeTPP\text{-}C_6H_5)^+$ is not observed. For the fragment $(FeTPP\text{-}C_6H_6)^+$, the offset voltage is centered to the nearly same value as that of $(FeTPP\text{-}H_2)^+$ and its abundance is dominant comparing to that of $(FeTPP\text{-}H_2)^+$. Qualitatively, the observations for the decay of singly charged $FeTPP^+$ are roughly in agreement with our result for doubly charged molecules. Unfortunately, in the ESI/CID experiment, the efficiency of the energy transfer into the target during the collisions is unknown; it is not possible to perform quantitative comparison.

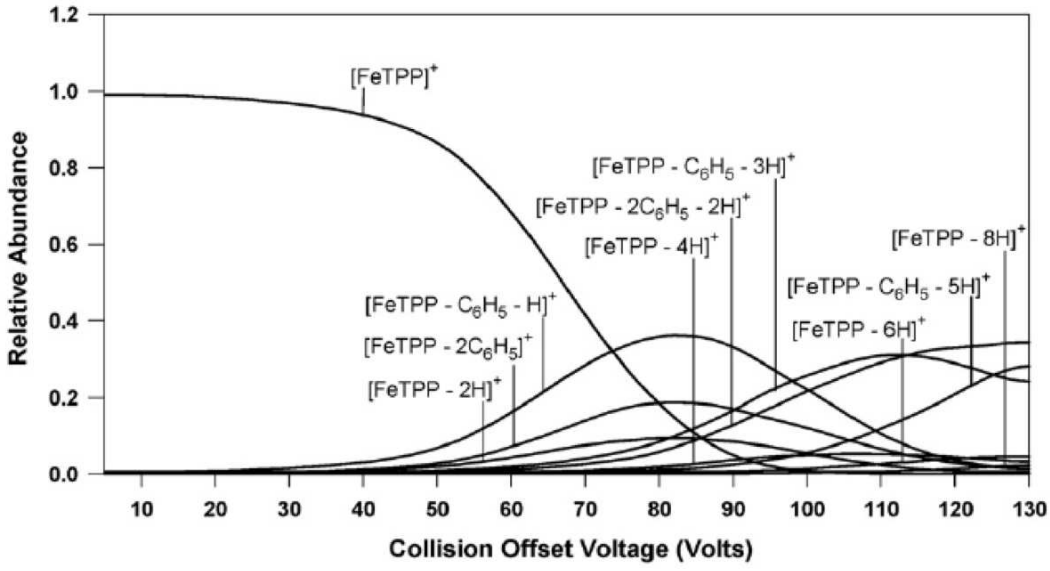

Figure 64. CID profiles monitored for the dissociation of $FeTPP^+$. From reference [74].

IV.5. *Conclusion*

In this chapter, the dissociation of a molecule of biological importance, FeTPPCl has been studied. The experimental setup has been operated in two ways: multi-coincidence mode and kinetic energy loss measurement mode.

In the multi-coincidence measurement, the parent excited ions were prepared by using 80keV Kr^{8+} impact. By coincidence detection of recoil ions, the ejected electron-number and final charge state of the scattered projectile (Kr^{7+}), the initial charge states of parent ions, $FeTPPCl^{r+}$ (r=1,2,3), are determined precisely. By analyzing the fragmentation TOF spectra of $FeTPPCl^{+}$, $FeTPPCl^{2+}$ and $FeTPPCl^{3+}$ parent molecules, it is shown that the main low-energy-cost fragmentation channel is the emission of neutral chlorine independent of the charge state of the FeTPPCl molecule. For $FeTPPCl^{2+}$ and $FeTPPCl^{3+}$ parent ions, the evaporation and asymmetrical fission processes have been measured showing that the emission of light charged fragment is always the phenyl group and never the monocharged chlorine cation. For $FeTPPCl^{2+}$, the evaporation of neutral fragments is the dominant fragmentation channel with a branching ratio measured to be 98%. For $FeTPP^{3+}$, the branching ratio for the asymmetrical fission is estimated to 83%±4%.

In the kinetic energy loss measurement, excited doubly charged parent ions $FeTPPCl^{2+}$ were prepared in 3keV F^{+} and H^{+} on molecule interaction. By using the CIDEC method, the energy windows activated by the two projectiles were measured. It was found that the excitation energy window was shifted to higher energy by about 3 eV in F^{+} collisions. For individual dissociation channels, the mean excitation energy of the parent ions before its fragmentation was determined. The results were discussed in comparison with other techniques, i.e., electron ionization (IE) experiments.

Although, the main fragmentation pathway of the intermediate $FeTPP^{2+}$ is the successive loss of phenyl groups, additional pathways with the loss of H_2 units are also observed using both F^{+} and H^{+} projectiles. By separating the excitation energy distribution spectra, the mean excitation energies for hydrogen loss processes were determined. In spite of the very different excitation energy windows in collisions with the two projectiles, the mean energy measured for the loss of the first H_2 is very near, 7.5 and 7.8 eV. Based on the experimental data, a more detailed dissociation diagram including the loss of H_2 is proposed.

Chapter V Summary

In this work, the fragmentations of isolated small biomolecules induced by low energy heavy ions at keV range were investigated using the setup in Lanzhou and in Lyon. Two molecules of biological importance were studied, i.e., Adenine ($C_5H_5N_5$, m=135) and FeTPPCl ($C_{44}H_{28}FeClN_4$, m=704). The former is one of the nucleobases in DNA; and the later is one of the porphyrin derivatives, an important and widespread class of pigments in nature.

The setup in Lanzhou was built to study the negative ion formation process in ion-molecule collisions. The specificity of this setup is to be able to detect scattered projectiles at all final charge states, including neutrals and negative ions, in coincidence with the detection of charged fragments. Thus the neutral and negative particle production yield can be directly measured.

The setup in Lyon can be operated in two modes: multi-coincidence mode and internal energy measurement mode (CIDEC measurement). In the triple coincidence measurement between the charge-analyzed projectile, the TOF of the recoil ions and the number of ejected electrons, the charge state of the parent recoil ions prior to the fragmentation can be determined without ambiguity. In the CIDEC method, based on the multi-coincidence technique, and analyzing the kinetic energy loss of the outgoing projectiles, one important parameter, the internal energy deposited in the target molecule during the collision, can be experimentally determined.

With these special equipments and techniques, the outcomes of this work are summarized as follows:

Adenine

- F^{2+} on Adenine collisions at 30keV were investigated by using the setup in Lanzhou. The neutral particle F^0 and negative ion F^- production yields were measured to be about 13% and 1%, respectively. The high enough negative ion rate gives an opportunity to perform coincidence measurement to study the fragmentation of small biomolecules by utilizing the CIDEC method.

- Based on CIDEC measurement, the fragmentation of doubly charged adenine molecule, produced in Cl^+ on Ade collisions at 3keV, was investigated. The fragmentation pattern of Ade^{2+} was dominated by successive emission of HCN^0 or H_2CN^+, and it was confirmed by the measured internal energy distributions. A specific fragmentation channel requiring less energy than the usual successive emission of neutral HCN was demonstrated, i.e., the emission of a charged H_2CN^+ following on by the emission of HC_2N_2, for which the measured mean excitation energy was about 8.4eV.

FeTPPCl

- In slow multi-charged ion Kr^{8+} on FeTPPCl collisions at 80keV, the outgoing projectile Kr^{7+} was charge selected in coincidence with recoil ions and the ejected electron number. The initial charge state, from 1+ to 3+, of the transient parent ions prior to the fragmentation was determined for each collision event. By analyzing the fragment TOF spectra of $FeTPPCl^{r+}$ (r=1,2,3), the dissociation scheme was built. It is found that the main low-energy-cost fragmentation channel is the emission of neutral chlorine independent of the charge state of the FeTPPCl molecule. For intermediate fragment dication $FeTPP^{2+}$, the dominant dissociation channel is the neutral evaporation of phenyl group. For intermediate trication $FeTPP^{3+}$, the dominant dissociation channel is the asymmetrical fission of charged phenyl.

- Excited parent dication $FeTPPCl^{2+}$ were prepared in 3keV F^+ and H^+ on FeTPPCl interactions. In F^+ collisions, the excitation energy window was measured to be shifted to higher energy by about 3 eV compared to collisions with H^+. This resulted in higher intensities of relatively small fragments on the mass spectrum. The mean excitation energies of the parent ions prior to fragmentation were determined for the main decay pathways. In the decay pattern of FeTPPCl molecule, additional channels like successive H_2 unit loss processes were investigated. The mean excitation energies for hydrogen loss processes were determined.

Reference

1. Boudaïffa B., et al., *Resonant Formation of DNA Strand Breaks by Low-Energy (3 to 20 eV) Electrons.* Science, 2000. **287**: p. 1658.
2. deVries J., et al., *Charge Driven Fragmentation of Nucleobases.* Phys. Rev. Lett., 2003. **91**: p. 053401.
3. Deng Z. W., et al., *Beyond the Bragg Peak: Hyperthermal Heavy Ion Damage to DNA Components.* Phys. Rev. Lett., 2005. **95**: p. 153201.
4. Jochims H. W., et al., *Photoion mass spectrometry of adenine, thymine and uracil in the 6–22 eV photon energy range.* Chemical Physics, 2005. **314**: p. 263.
5. Sanche L., *Low energy electron-driven damage in biomolecules.* Eur. Phys. J. D, 2005. **35**: p. 367.
6. Liu B., et al., *Collision-Induced Dissociation of Hydrated Adenosine Monophosphate Nucleotide Ions: Protection of the Ion inWater Nanoclusters.* Phys. Rev. Lett., 2006. **97**: p. 133401.
7. Antic D., et al., *Low-Energy Electron Damage to Condensed-Phase Deoxyribose Analogues Investigated by Electron Stimulated Desorption of H^- and Electron Energy Loss Spectroscopy.* J. Phys. Chem. B, 1999. **103**: p. 6611.
8. Antic D., Parentea L. U., and Sanche L., *Electron-Stimulated Desorption of H^- from Condensed-Phase Deoxyribose Analogues: Dissociative Electron Attachment versus Resonance Decay into Dipolar Dissociation.* J. Phys. Chem. B, 2000. **104**: p. 4711.
9. Boudaïffa B., et al., *Induction of single- and double-strand breaks in plasmid DNA by 100–1500 eV electrons* Int. J. Radiat. Biol. , 2000. **76**: p. 1209.
10. Abdoul-Carime H., Cloutier P., and Sanche L., *Low-Energy (5–40 eV) Electron-Stimulated Desorption of Anions from Physisorbed DNA Bases.* Radiat. Res., 2001. **155**: p. 625.
11. Huels M. A., et al., *Single, Double, and Multiple Double Strand Breaks Induced in DNA by 3-100 eV Electrons.* J. Am. Chem. Soc., 2003. **125**: p. 4467.
12. Hanel G., et al., *Electron Attachment to Uracil: Effective Destruction at Subexcitation Energies.* Phys. Rev. Lett., 2003. **90**: p. 188104.
13. Denifl S., et al., *Electron attachment to 5-chloro uracil.* J. Chem. Phys., 2003. **118**: p. 4107.

14. Denifl S., et al., *Electron attachment to the DNA bases thymine and cytosine.* Chem. Phys. Lett., 2003. **377**: p. 74.
15. Feil S., et al., *Partial cross sections for positive and negative ion formation following electron impact on uracil.* J. Phys. B: At. Mol. Opt. Phys., 2004. **37**: p. 3013.
16. Denifl S., et al., *Threshold electron impact ionization studies of uracil.* Int. J. of Mass Spectrom., 2004. **238**: p. 47.
17. Ptasińska S., et al., *Inelastic electron interaction (attachment/ionization) with deoxyribose.* J. Chem. Phys., 2004. **120**: p. 8505.
18. Denifl S., et al., *Mass Spectrometric Investigation of Anions Formed upon Free Electron Attachment to Nucleobase Molecules and Clusters Embedded in Superfluid Helium Droplets.* Phys. Rev. Lett., 2006. **97**: p. 043201.
19. Denifl S., et al., *Electron Attachment to the Gas-Phase DNA Bases Cytosine and Thymine.* J. Phys. Chem. A, 2004. **108**: p. 6562.
20. Denifl S., et al., *Electron attachment to gas-phase uracil.* J. Chem. Phys., 2004. **120**: p. 6557.
21. Ptasińska P., et al., *Dissociative ionization of the nucleosides thymidine and uridine by electron impact.* Chem. Phys. Lett., 2005. **409**: p. 270.
22. Feil S., et al., *Single, double and triple ionization of tetraphenyl iron(III) porphyrin chloride.* Int. J. Mass Spectrom., 2006. **255-256**: p. 232.
23. Schlathölter T., Hoekstra R., and Morgenstern R., *Charge driven fragmentation of biologically relevant molecules.* Int. J. Mass Spect., 2004. **233**: p. 173.
24. Deng Z. W., Imhoff M., and Huels M. A., *Fragmentation dynamics of condensed phase thymine by low-energy (10–200 eV) heavy-ion impact.* J. Chem. Phys., 2005. **123**: p. 144509.
25. Deng Z. W., et al., *Reactive Scattering Damage to DNAComponents by Hyperthermal Secondary Ions.* Phys. Rev. Lett., 2006. **96**: p. 243203.
26. Deng Z. W., et al., *Fragmentation of condensed-phase DNA components by hyperthermal He^+ impact.* Phys. Rev. A, 2006. **74**: p. 012716.
27. Bald I., et al., *10–100 eV Ar^+ ion induced damage to D-ribose and 2-deoxy-D-ribose molecules in condensed phase.* Phys. Chem. Chem. Phys., 2006. **8**: p. 1215.
28. Rice J. M. and Dudek G. O., *Mass Spectra of Nucleic Acid Derivatives. II. Guanine, Adenine, and Related Compounds.* J. Am. Chem. Soc., 1967. **89**: p. 2719.
29. Sethi S. K., et al., *Mass spectrometry of nucleic acid constituents. Electron ionization spectra of selectively labeled adenines.* J. Am. Chem. Soc., 1982. **104**: p. 3349.

30. Barrio M.G., et al., *Syntheses of all singly labeled [^{15}N]adenines: Mass spectral fragmentation of adenine.* Proc. Natl. Acad. Sci. USA, 1981. **78**: p. 3986.
31. deVries J., et al., *C^{q+}-induced excitation and fragmentation of uracil: effects of the projectile electronic structure.* J. Phys. B: At. Mol. Opt. Phys., 2002. **35**: p. 4373.
32. deVries J., et al., *Multiple ionization and fragmentation of the DNA base thymine by interaction with C^{q+} ions.* Eur. Phys. J. D, 2003. **24**: p. 161.
33. deVries J., et al., *Ionization and Fragmentation Modes of Nucleobases after Collisions with Multiply Charged Ions.* Physica Scripta, 2004. **T110**: p. 336.
34. Schlathölter T., Alvarado F., and Hoekstra R., *Ion-biomolecule interactions and radiation damage.* Nucl. Instr. and Meth. B, 2005. **233**: p. 62.
35. Alvarado F., et al., *Quantification of ion-induced molecular fragmentation of isolated 2-deoxy-D-ribose molecules.* Phys. Chem. Chem, Phys, 2006. **8**: p. 1922.
36. Schlathölter T., et al., *Ion-Induced Biomolecular Radiation Damage: From Isolated Nucleobases to Nucleobase Clusters.* ChemPhysChem, 2006. **7**: p. 2339.
37. Alvarado F., et al., *Interactions of neutral and singly charged keV atomic particles with gas-phase adenine molecules.* J. Chem. Phys., 2007. **127**: p. 034301.
38. Alvarado F., et al., *Precise Determination of 2-Deoxy-d-Ribose Internal Energies after keV Proton Collisions.* ChemPhysChem , , 2008. **9**: p. 1254.
39. Brédy R., et al., *Fragmentation of adenine induced by collision with slow F^{2+} ions.* Nucl. Instr. and Meth. B, 2005. **235**: p. 392.
40. Martin S., et al., *Coincidence method for measuring the mass of neutral fragments emitted in a delayed fragmentation process from a singly charged molecule: Fragmentation pathway of adenine.* Phys. Rev. A 2008. **77**: p. 062513.
41. Chen L., et al., *Direct Measurement of Internal Energy of Fragmented C_{60}.* Phys. Rev. Lett., 2007. **98**: p. 193401.
42. Scheier P., et al., *Appearance and ionization energies of singly, doubly and triply charged C_{60} and its fragment ions produced by electron impact ionization.* Int. J. Mass Spectrom. Ion Processes, 1994. **138**: p. 77.
43. Hathiramani D., et al., *Electron-Impact Induced Fragmentation of Fullerene Ions.* Phys. Rev. Lett., 2000. **85**: p. 3604.
44. Fournier P. G., et al., *Validity of Franck-Condon principle for H^+ to H^- double charge transfer of fast protons on H_2 at low scattering angle* J. Phys. B: At. Mol. Opt. Phys., 1972. **5**: p. L58.

45. Durup J., et al., *Collision-radiation-collision three-step processes, and a measurement of the probability ratio for neutralization of 4 keV protons into either H(2p) or H(1s).* J. Phys. B: At. Mol. Phys. , 1972 **5** p. L110.

46. Harris F. M., *Double-charge-transfer spectrometry and the measurement of electronic-state energies of doubly charged ions.* Int. J. Mass Spectrom. Ion Processes, 1992. **120**: p. 1.

47. Fournier P. G., et al., *Theoretical and experimental studies of the elcetronic states of the diatomic cation Cl_2^{2+}.* Phys. Rev. A, 1986. **34**: p. 1657.

48. Furuhashi O., et al., *Double charge transfer spectroscopy for N_2^{2+} and CO^{2+} at vibrational resolution.* Chem. Phys. Lett., 2001. **337**: p. 97.

49. Langford M. L., et al., *Determination of singlet- and triplet-state energies of the doubly ionized ammonia molecule by double-charge-transfer spectroscopy.* Int. J. Mass Spectrom. Ion Processes, 1992. **116**: p. 53.

50. Langford M. L., et al., *Triplet-state energy levels of CO_2^{2+}, COS^{2+} and CS_2^{2+}.* Chem. Phys., 1991. **149**: p. 445.

51. Griffiths W. J., et al., *Double-ionization energies of the chloroethane molecules CH_3CH_2Cl, CH_3CHCl_2, CH_3CCl_3, CH_2ClCH_2Cl, $CH_2ClCHCl_2$, CH_2ClCCl_3, $CHCl_2CHCl_2$, $CHCl_2CCl_3$ and CCl_3CCl_3.* Int. J. Mass Spectrom. Ion Processes, 1992. **112**: p. 45.

52. Harris F. M., et al., *Experimental investigation of double ionization to ground and electronically excited states of chlorobenzene, 1,2-, 1,3- and 1,4-dichlorobenzene, 1,2,3-, 1,2,4- and 1,3,5-trichlorobenzene, 1,2,3,4-and 1,2,4,5-tetrachlorobenzene and pentachlorobenzene dications.* Org. Mass Spectrom., 1992. **27**: p. 261.

53. Martin S., et al., *Fragmentation patterns of multicharged C_{60}^{r+} (r=3–5) studied with well-controlled internal excitation energy.* Phys. Rev. A 2008. **77**: p. 043201.

54. Brédy R., et al., *Fragmentation of adenine under energy control.* J. Chem. Phys., 2009. **130**: p. 114305.

55. Hayatsu R., *Orgueil Meteorite: Organic Nitrogen Contents* Science, 1964. **146**: p. 1291.

56. Sephton M. A. and Gilmour I., *Compound-specific isotope analysis of the organic constituents in carbonaceous chondrites.* Mass Spectrom. Rev, 2001. **20**: p. 111.

57. Cooper G., et al., *Carbonaceous meteorites as a source of sugar-related organic compounds for the early Earth.* Nature, 2001. **414**: p. 879.

58. Lawler M. E. and Brownlee D. E., *CHON as a component of dust from comet Halley.* Nature, 1992. **359**: p. 180.
59. Kissel J., et al., *Composition of comet Halley dust particles from Vega observations.* Nature, 1986. **321**: p. 280.
60. Varmuza K., et al., *Organic substances in cometary grains: comparison of secondary ion mass spectral data and californium-252 plasma desorption data from reference compounds.* Int. J. Mass Spectrom., 1999. **189**: p. 79.
61. Blanksby S. J. and Bowie J. H., *Construction of interstellar cumulenes and heterocumulenes: Mass Spectrometric Studies.* Mass Spectrom. Rev, 1999. **18**: p. 131.
62. Floss C., et al., *Carbon and Nitrogen Isotopic Anomalies in an Anhydrous Interplanetary Dust Particle.* Science, 2004. **303**: p. 1355.
63. Peeters Z., et al., *The Astrobiology of Nucleobases.* Astrophys. J. Lett., 2003. **593**: p. L129.
64. Brack A., *From Interstellar Amino Acids to Prebiotic Catalytic Peptides: A Review.* Chem. Biodivers., 2007. **4**: p. 665.
65. Nelson C. C. and McCloskey J. A., *Collision-Induced Dissociation of Adenine.* J. Am. Chem. Soc., 1992. **114**: p. 3661-3668.
66. Moretto-Capelle P., et al., *Energetics and metastability of the adenine dication observed in proton-adenine collisions.* J. Chem. Phys., 2007. **127**: p. 234311.
67. Academic Press Dictionary of Science Technology.
68. . The porphyrins Handbook, ed. Kadish K. M., Smith K. M., and Guillard R. Vol. 1-20. 2003, Oxford: Elsevier Science.
69. Battersby A. R., et al., *Biosynthesis of the pigments of life: formation of the macrocycle.* Nature, 1980. **285**: p. 17.
70. Battersby A. R., *Tetrapyrroles: the pigments of life.* Nat. Prod. Rep., 2000. **17**: p. 507.
71. Porphyrin Localisation and treatment of tumor, ed. Doiron D. R. and Gomer C. J. 1984, New York: A. R. Liss.
72. Dale M. J., et al., *Investigation of porphyrins and metalloporphyrins using two-step laser mass spectrometry.* J. Mass Spectrom., 1996. **31**: p. 590.
73. Bernigaud V., et al., *Ionisation and fragmentation of tetraphenyl iron (III) porphyrin chloride induced by slow multiply charged ion impact.* Eur. Phys. J. D, 2009. **51**: p. 125.

74. Gozet T., Huynh L., and Bohme D. K., *Collision-induced dissociation of tetraphenyl iron and manganese porphyrin ions by electrospray ionization mass spectrometry.* Int. J. Mass Spectrom., 2009. **279**: p. 113.
75. Geller R., IEEE Trans. Nucl. Sci. , 1976. **NS-23**: p. 904.
76. Sortais P., *Recent progress in making highly charged ion beams.* Nucl. Instr. and Meth. B, 1995. **98**: p. 508.
77. *http://www.strz.uni-giessen.de/~ezr/images/principle.jpg*.
78. Bernrd J., *Etude de la double capture électronique dans des collisions d'ions nus sur des atomes de gaz rare*. 1995, Universite Claude Bernard, Lyon 1: Lyon.
79. Brédy R., *Etude experimentale de la multicapture electronique dans des collisions a basse vitesse entre des ions muticharges et des C_{60}: formation et stabilisation d'atomes creux*. 2001, Universite Claude Bernard, Lyon 1: Lyon.
80. Wei B., *Studies of fragmentation of multi-charged C_{60}^{r+} produced in slow highly charged ion-fullerene collisions*. 2005, Universite Claude Bernard, Lyon 1: Lyon.
81. Martin S., et al., *Excitation and fragmentation of C_{60} (r=3-9) in Xe^{30+}-C_{60} collisions.* Phys. Rev. A, 2000. **62**: p. 022707.
82. Furuhashi O., et al., *Studies of doubly charged molecular ions using high-resolution double charge transfer spectrometer.* J. Mass Spectrom. Soc. Jpn., 2002. **50**: p. 24.
83. Martin S., et al., *High formation yields of negative ions in multicharged fluorine F^{q+}(q = 1–3)-C_{60} collisions.* Europhys. Lett. , 2006. **74**: p. 985.
84. Jagutzki O., et al., *A broad-application microchannel-plate detector system for advanced particle or photon detection tasks: large area imaging, precise multi-hit timing information and high detection rate.* Nucl. Instr. and Meth. A, 2002. **477**: p. 244.
85. Andersen T., *Atomic negative ions: structure, dynamics and collisions.* Phys. Rep., 2004. **394**: p. 157-313.
86. Appell J., *Collision Spectroscopy*, ed. R. G. Cooks. 1978 New York: Plenum.
87. Meyer F. W., et al., *On the neutralization of singly and multicharged projectiles during grazing interactions with LiF(100).* Nucl. Instrum. Methods Phys. Res. B, 1997. **125**: p. 138-145.
88. Auth C., Borisov A. G., and Winter H., *High fractions of negative ions in grazing scattering of fast oxygen atoms from a LiF(100) surface.* Phys. Rev. Lett., 1995. **75** p. 2292.

89. Barat M., et al., *Absolute detection efficiency of a microchannel plate detector for neutral atoms.* Rev. Sci. Instrum., 2000. **71**: p. 2050.
90. Brehm B., et al., *Absolute detection efficiencies of a microchannel plate detector for ions* Meas. Sci. Technol., 1995. **6**: p. 953-958.
91. Cederquist H., et al., *Electronic response of C_{60} in slow collisions with highly charged ions.* Phys. Rev. A, 2000. **61**: p. 022712.
92. Campbell E. E. B., Raz T., and Levine R. D., *Internal energy dependence of the fragmentation patterns of C_{60} and C_{60}^+.* Chem. Phys. Lett., 1996. **253**: p. 261-267.
93. Martin S., unpublished.
94. Roca-Sanjuán D., et al., *Ab initio determination of the ionization potentials of DNA and RNA nucleobases.* J. Chem. Phys., 2006. **125**: p. 084302.
95. Schmidt M. W., et al., *General atomic and molecular electronic structure system.* J. Comput. Chem., 1993. **14**: p. 1347.
96. Abdul-Rahman A., *GABEDIT, http://gabedit.sourceforge.net/home.html.*
97. *NIST Chemistry WebBook, http://webbook.nist.gov.*